ABSTRACT

Title of Document: MULTIDISCIPLINARY OPTIMIZATION OF NON-SPHERICAL, BLUNT-BODY HEAT SHIELDS FOR A PLANETARY ENTRY VEHICLE

Joshua E. Johnson
Master of Science, 2006

Directed By: Professor Mark J. Lewis
Department of Aerospace Engineering

Gradient-based optimization of the aerodynamic performance, static stability, and stagnation-point heat transfer has been completed to find optimal heat shield geometries for blunt-body planetary entry vehicles. In the parametric study, performance trends have been identified by varying geometric parameters that define a range of cross-sections and axial shapes. Cross-sections considered include oblate and prolate ellipses, rounded-edge polygons, and rounded-edge concave polygons. Axial shapes consist of the spherical-segment, spherically-blunted cone, and power law. By varying angle-of-attack and geometric parameters, the aerodynamics, static stability, and heat transfer are optimized based on Newtonian impact theory with semi-empirical shock-standoff distance and stagnation-point heat transfer correlations. Methods have been verified against wind tunnel and flight data of the Apollo Command Module and are within 15% for aerodynamic coefficients and stagnation-point heat fluxes. Results indicate that oblate parallelogram configurations provide optimal sets of aerothermodynamic characteristics.

MULTIDISCIPLINARY OPTIMIZATION OF NON-SPHERICAL, BLUNT-BODY HEAT SHIELDS FOR A PLANETARY ENTRY VEHICLE

By

Joshua E. Johnson

Thesis submitted to the Faculty of the Graduate School of the
University of Maryland, College Park, in partial fulfillment
of the requirements for the degree of
Master of Science
2006

Advisory Committee:
Professor Mark J. Lewis, Chair
Professor Roberto Celi
Associate Professor James Baeder

Dedication

To my parents John and Caroline who have given me immeasurable knowledge in life and have encouraged me to be a part of furthering human space exploration. To my sisters Justine and Lucia Maria who are just starting out in this world.

Acknowledgements

I would like to express my gratitude to Dr. Mark Lewis for the opportunity to conduct this research, who through his achievements in the field of hypersonics, has inspired me to strive forward in my studies and aerospace career. I would like to thank Dr. Ryan Starkey for his endless patience and time given in assisting me with my research. I would also like to thank the other members of my committee Dr. Roberto Celi, who taught me gradient-based optimization theory, and Dr. James Baeder, who taught me the basic theories of computation fluid dynamics.

I also would like to acknowledge the NASA funding that supported this work. This research was supported by the Space Vehicle Technology Institute (SVTI), one of the NASA Constellation University Institute Projects (CUIP), under grant NCC3-989, with joint sponsorship from the Department of Defense. Appreciation is expressed to Dr. Ken Yu, director of the SVT Institute at the University of Maryland, Claudia Meyer of the NASA Glenn Research Center, program manager of CUIP, and to Dr. John Schmisseur and Dr. Walter Jones of the Air Force Office of Scientific Research, the support of whom is greatly appreciated.

Finally, I would like to thank my fellow SVTI graduate students, who have given me friendship and support, and especially to Adam Dissel for the early hours of company and learning that has greatly enhanced my graduate school experience.

Table of Contents

List of Tables

List of Figures

List of Symbols

A	=	Coefficient of power law
A_b	=	Area of the base (m^2)
A_p	=	Planform area (m^2)
AFE	=	Aeroassist Flight Experiment
a	=	Speed of sound (m/s)
a_1	=	Semimajor axis length of a superellipse (m)
a_2	=	Semimajor axis length of a blunt body(m)
b	=	Exponent of power law
b_1	=	Semiminor axis length of a superellipse (m)
b_2	=	Semiminor axis length of a blunt body (m)
C	=	Aerodynamic coefficient
CEV	=	Crew Exploration Vehicle
CFD	=	Computational fluid dynamics
CM	=	Command Module, refers to Project Apollo unless noted otherwise
DOT	=	Design Optimization Tools
d	=	Diameter (m)
d_1, d_2	=	Distances from mesh point to point as indicated in the text
$d_{(j,k),(j+1,k)}$	=	Distance from mesh point (j,k) to point $(j+1,k)$
dA	=	Differential surface area
dA_p	=	Differential planform area
dr	=	Differential distance from mesh point to origin
dV	=	Differential volume
$d\theta$	=	Differential theta
$d\phi$	=	Differential sweep angle
E	=	Search direction for optimization
e	=	Eccentricity
FIRE	=	Flight Investigation of the Reentry Environment
$\vec{G}$	=	Vector of constraints
G_q	=	q^{th} constraint
F	=	Integration of f with respect to x
f	=	Function of x
g_1, g_2, g_3	=	Radiation correlation parameters
g_w	=	Ratio of wall enthalpy to total enthalpy
H	=	Correlation exponent
h	=	Altitude (ft)
	=	Step size
j	=	Mesh point index in ϕ-direction
j_{max}	=	Maximum mesh points in ϕ-direction
k	=	Mesh point index in x-direction
k_{max}	=	Maximum mesh points in x-direction
l	=	Length of heat shield from nose to base (m)
l_b	=	Length from differential surface to base (m)

l_M	=	Length of the semimajor axis of the cross-section
L/D	=	Lift-to-drag ratio
MMFD	=	Modified Method of Feasible Directions
M_∞	=	Freestream Mach number
m	=	Number of sides of the superellipse in the superformula
N	=	Total number of sections in which to divide the conical base
NCON	=	Number of constraints
NDV	=	Number of design variables
n	=	Number of the section of the conical base
n_1, n_2, n_3	=	Superelliptic parameters
$\hat{n}$	=	Outward normal of a surface
OBJ	=	Objective function
$O(\vec{X})$	=	Objective function as a function of $\vec{X}$
PEV	=	Planetary entry vehicle
p	=	Index corresponding to a specific design variable X_p
q	=	Index corresponding to a specific constraint G_q
q_∞	=	Freestream dynamic pressure (Pa)
$\dot{q}_s$	=	Stagnation-point heat flux (W/m^2)
RCS	=	Reaction control system
r	=	Base radius (m)
r_c	=	Corner radius (m)
r_{eff}	=	Effective radius of curvature for radiative heat transfer (m)
r_n	=	Nose radius for spherically-blunted cone axial shape (m)
r_s	=	Radius of curvature for spherical-segment axial shape (m)
r_{st}	=	Length from the central axis to the stagnation point (m)
r_{sh}	=	Radius of curvature for the spherical shock (m)
S	=	Surface area of cross-section (m^2)
S_{hs}	=	Surface area of heat shield without base area (m^2)
SCRAMP	=	Slotted Compression Ramp
TPS	=	Thermal Protection System
u	=	Iteration number
V_∞	=	Freestream velocity magnitude (m/s)
V_{hs}	=	Volume of heat shield (m^3)
V_x, V_y, V_z	=	Freestream velocity components normalized by V_∞
v	=	Exponent of superellipse equation
WT	=	Wind tunnel
w	=	Distance from point (j,k) to x-axis
w_v	=	Wind angle
$\vec{X}$	=	Vector of design variables X_p, in which p = 1 to NDV
X_p	=	p^{th} design variable
x, y, z	=	Coordinate directions
x_s	=	The streamwise distance from the apex of the shock to the point on the shock at distance y_* from the central axis
α	=	Angle-of-attack (deg)
α^*	=	Scalar parameter for optimization
β	=	Sideslip angle (deg)

γ	=	Ratio of specific heats
Δ_{so}	=	Shock-standoff distance (ft)
ε	=	Inclination on forward body surface at the tangent point with corner radius, also mentioned as tangency angle
η_v	=	Volumetric efficiency (surface area comparison)
θ_c	=	Half-cone angle (deg)
θ_s	=	Half-spherical-segment angle (deg)
θ_*	=	Shock surface inclination at a point opposite of the sonic point on a body with respect to a plane normal to the freestream direction
θ_{*o}	=	Shock surface inclination at a point opposite of the sonic point on a flat disk
λ	=	Lagrange multiplier
ρ	=	Density (kg/m^3)
Φ_*	=	Sonic angle of a blunt body, which is the body surface inclination of a blunt body at the sonic point with respect to a plane normal to freestream direction
Φ_{*1},	=	Sonic angle of a sphere
ϕ	=	Sweep angle (rad)
	=	Azimuth angle
ω	=	Angle from *x*-axis and in the *xy* plane (rad)

Subscripts

0	=	Location at tip of nose, stagnation point, moments normalized by base diameter *d*
1	=	Before the normal shock
2	=	After the normal shock
75	=	75% of value assuming uniform density
A	=	Axial force
cg	=	Location of center of gravity
conv	=	Convective
cp	=	Location of center of pressure
D	=	Drag
eff	=	Effective
H	=	Horizontal component with respect to the body
j	=	*xy*-plane index
L	=	Lift
l	=	Rolling moment
lower	=	Lower constraint value
m	=	Pitching moment
N	=	Normal force
nd	=	Non-dimensionalized vector
n	=	Yawing moment
R	=	Resultant
rad	=	Radiative
sl	=	Sea level
tot	=	Total

UD	=	Uniform density
upper	=	Upper constraint value
V	=	Vertical component with respect to the body
Y	=	Side force
α	=	Derivative with respect to angle-of-attack (per rad)
β	=	Derivative with respect to sideslip angle (per rad)
∞	=	Freestream conditions

Chapter 1. Introduction

1.1. Motivation

A blunt-bodied planetary entry vehicle (PEV) requires a proper combination of aerodynamic performance, stability, and heat transfer for it to successfully follow its designed planetary entry trajectory. The simplest blunt-bodied planetary entry vehicle is the re-entry space capsule. It is covered with thermal protection material, with heat shield materials that can withstand very high temperatures on the surface of the vehicle that faces the freestream.

The heat shield is designed to protect a majority of the vehicle from entry temperatures, and because the flow typically separates from the vehicle past the heat shield, its geometry generally defines the capsule's hypersonic aerodynamic performance. The design also provides passive protection from entry flow disturbances that could destabilize the vehicle and endanger the astronauts, and active protection from rolling is also provided on human planetary entry vehicles with a reaction control system (RCS). The passive protection is acquired through the aerodynamic design of the heat shield, and it is common during an initial analysis for aerodynamic performance, stability and heat transfer characteristics to be satisfied mostly through the design of a vehicle's heat shield.

Blunt-bodied capsules, such as the one that will be used by NASA's Crew Exploration Vehicle (CEV), will re-enter Earth's atmosphere at high hypersonic velocities, with projected Mach numbers ranging from 30 to 50. Such high Mach numbers deliver high heat fluxes greater than 300 W/cm^2 along the frontal surface

and heat loads greater than 30000 J/cm^2. Since it is not clear that the classic spherical-segment[1] or spherically-blunted cone[2,3] provides optimal aerothermodynamic performance, executing an optimization on the aerodynamics, static stability, and heat transfer for a broad range of heat shield shapes may assist in ascertaining an optimal, stable configuration with higher lift-to-drag (*L/D*) and lower heat transfer fluxes and loads.

A parametric formulation of the aerodynamic performance and stability of heat shields based on Newtonian impact theory is completed in this work, with the addition of semi-empirical methods for the calculation of the stagnation-point heat fluxes. An optimizer is applied to this formulation to analyze the aerothermodynamic performance of heat shield geometries.

1.2. Previous Work

1.2.1. Heat Shield Geometries

The two primary classes of shapes that have been developed by NASA are the spherical-segment and the spherically-blunted cone, shown in Figure 1.1(a) and (b) respectively. Extensive research on spherical-segments led to its use as the heat shield for human re-entry space capsules including the NASA Gemini and Apollo missions. The spherical-segment is described by a spherical radius r_s and maximum spherical-segment angle θ_s measured from the central axis. The Project Gemini Re-entry Module[4,5] included a 38^o spherical-segment heat shield (θ_s = 19^o) with r_s = 3.712 m, and a base diameter of 2.32 m. The Project Apollo Command Module (CM) had a 50^o spherical-segment (θ_s = 25^o) with r_s = 4.694 m, and a base diameter of 3.912 m.

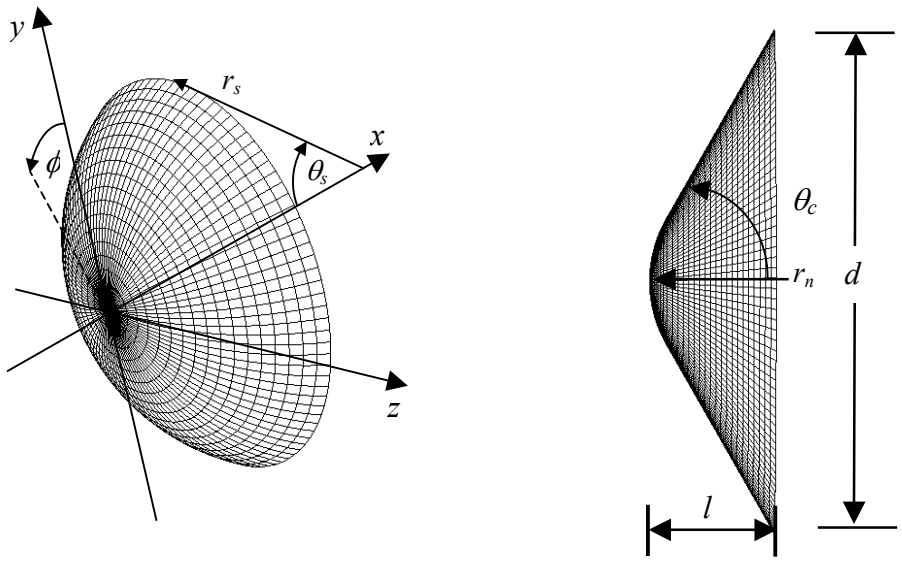

a) Spherical-segment heat shield, $\theta_s = 60^o$. **b) Spherically-blunted cone heat shield, $r_n/d = 0.25$, $\theta_c = 60^o$.**

Figure 1.1. The two most familiar heat shield geometries.

Specific Apollo mission aerodynamic flight data is provided for Apollo mission AS-202 and Apollo 4 in Ref. [6] and Ref. [7] respectively. The Command Module in AS-202 re-entered Earth's atmosphere at 8.23 km/s (27,000 ft/s) to produce planetary entry conditions that occur when entering from satellite orbit. The Apollo 4 (AS-501) followed an elliptical orbit around Earth that produced the expected re-entry velocity from lunar return of 10.7 km/s (35,100 ft/s). Rather than passing by the Moon, Apollo 4 had a second Service Module Propulsion System (SPS) burn at trajectory location 13 marked in Figure 1.2 to produce lunar return re-entry conditions and reduce the mission time to 8.5 hours (from six days). Hillje[7] provided Apollo flight data which was used for code validation and is presented in Chapter 6. Note that most of the aerodynamic data from the Apollo flights can be reproduced accurately by this work, except for the normal coefficient C_N which can have up to 40% difference compared to the available flight-derived data.

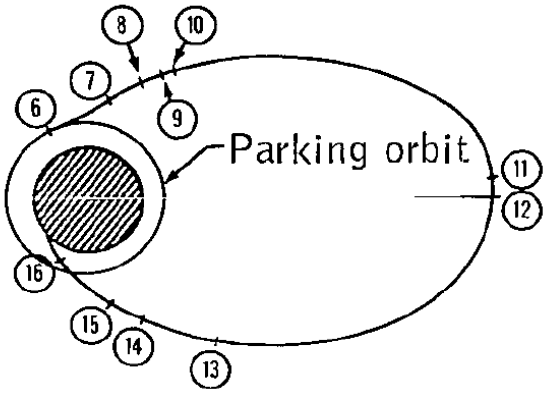

Figure 1.2. Apollo 4 Trajectory from Ref. [7].

Moseley analyzed the aerodynamic stability characteristics of the Apollo Command Module in Refs. [8] and [9]. Both of these NASA Technical Notes provide aerodynamic, static and dynamic stability wind tunnel data on several Command Module configurations with their schematics and relative dimensions. From this set, only two figures are dedicated to rolling moment stability in Ref. [8], and so a discussion of the Command Module's roll static stability is provided in Chapter 6. DeRose[10] provides an analysis of the center-of-gravity offset from the central axis of the vehicle and also discusses the proper way to compare wind tunnel measurements of a non-ablative model to a flight vehicle with an ablative heat shield. Horstman[11] compares the Apollo and Gemini wind tunnel models with center-of-gravity offsets.

The spherically-blunted cone is another commonly-used blunt-body space capsule configuration, as shown in Figure 1.1(b). It is defined by half-cone angle θ_c, the nose radius r_n, and base diameter d. It is common to see the ratio r_n/d as a listed characteristic. Because convective heat transfer increases while radiative heat transfer decreases with a reduction in radius for a blunt-body, there is an optimum r_n that minimizes the heat transfer to the vehicle. The advantage of this configuration is that it can offer designs with the same base radius as a spherical segment without

constraining the nose radius. If the optimal heat shield design for a given set of mission requirements has a smaller nose radius than can be offered by a spherical-segment with base radius r, then that nose radius could be generated with a spherically-blunted cone configuration. Also, the equations that render the spherically-blunted cone can be setup to account for the entire spherical-segment regime.

Chrusciel[3] provides a method for calculating the aerodynamic characteristics of spherically-blunted cones. Chrusciel provides the change in the center-of-pressure location with an increase in nose radius and was used in this work to determine a reasonable range of center-of-pressure locations. A discussion on the misunderstanding present in several sources concerning the calculation of the center-of-pressure location is included in Chapter 3 and those sources are mentioned later in this section.

Jones[12] has completed a wind tunnel investigation on model comparison of the pressure distributions on sharp-nosed and spherically-blunted cones with large cone angles θ_c at hypersonic speeds in air (M_∞ = 7.9), helium (M_∞ = 20.3), and tetrafluoromethane CF_4 (M_∞ = 6.2). The pressure distributions from the three different gases for the tested configurations almost always overlap each other at $\alpha = 0^o$. These results are also compared to theoretical methods including Newtonian theory and concluded that the Newtonian theory does not predict the surface pressure distribution properly near the edges of the configuration. It also shows that there are significant differences in the actual distribution and the one rendered by Newtonian theory. It is shown in this work that although this may be true, Newtonian theory can predict the

aerodynamic forces and moments of the Apollo Command Module (spherical-segment) within 15% and the trim angle-of-attack within 1.2°. Additional work on spherically blunted cones has been completed by Tauber[13] and Bernot.[14]

The spherically-blunted cone configuration was used on the Viking[2,15] and Pathfinder[16,17,18] missions to Mars. Two Viking missions consisted of an orbiter and a lander. The orbiter mapped the surface of Mars, and the landers of the Viking I and II missions had the first successful Mars landings in 1976. The Viking space capsule,[19] shown in Figure 1.3, housed the lander and had a superlight ablative (SLA) heat shield of dimensions $\theta_c = 70^o$, $r_n/d = 0.25$, and $d = 3.505$ m.

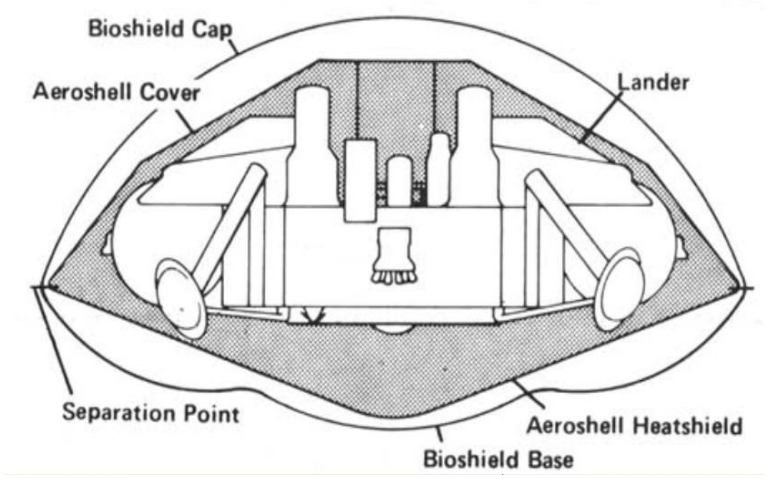

Figure 1.3. Viking Landing Capsule System from Ref. [19].

In 1997, the Mars Pathfinder mission had a Mars rover that was thermally protected during planetary entry by an aeroshell thermal protection system (TPS). Once on the surface, the Pathfinder rover would photograph the immediate vicinity and acquire data that would be sent back to Earth for analysis. Although higher heat fluxes were expected during planetary entry, the Pathfinder mission had a heat shield with the same θ_c and r_n/d as the Viking capsules.

More recent heat shield designs include the raked cone, the biconic and bent biconic cones, the parashield, and the flare-skirt aft-body. The raked cone geometry[20,21] is a spherically-blunted cone raked at an angle as shown in Figure 1.4.

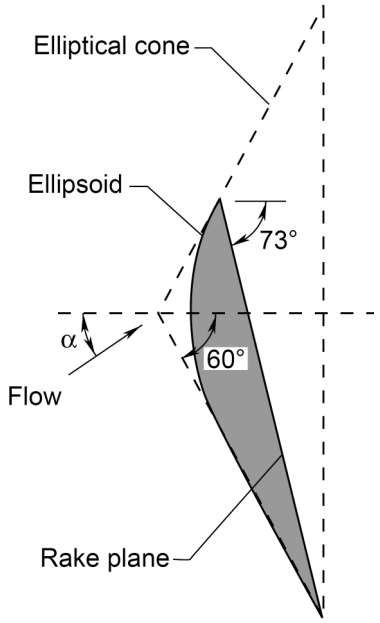

Figure 1.4. Raked cone from Ref. [21].

This geometry offers a way to produce positive lift at zero angle-of-attack. Since the bottom surface of the heat shield has greater surface area than the upper half by design, the flow accelerates more over the bottom surface. This produces positive lift because a larger portion of the surface pressure contributes to lift from the bottom surface than the top surface. The raked cone geometry can be designed to render higher *L/D* at negative angles-of attack than its axisymmetric analogue.

An example of the raked cone geometry is the Aeroassist Flight Experiment (AFE) that NASA worked on and cancelled in the early 1990s. It had a 14 ft diameter and was planned to participate in ten Shuttle-launched experiments. Figure 1.4 shows a few of the dimensions of the AFE's heat shield geometry. It has a 60^o half-cone angle and a 73^o cone rake angle. One additional feature of the AFE's rendition of the

raked cone is its ellipsoid nose with an ellipticity equal to 2. The AFE geometry is shown in Figure 1.5.

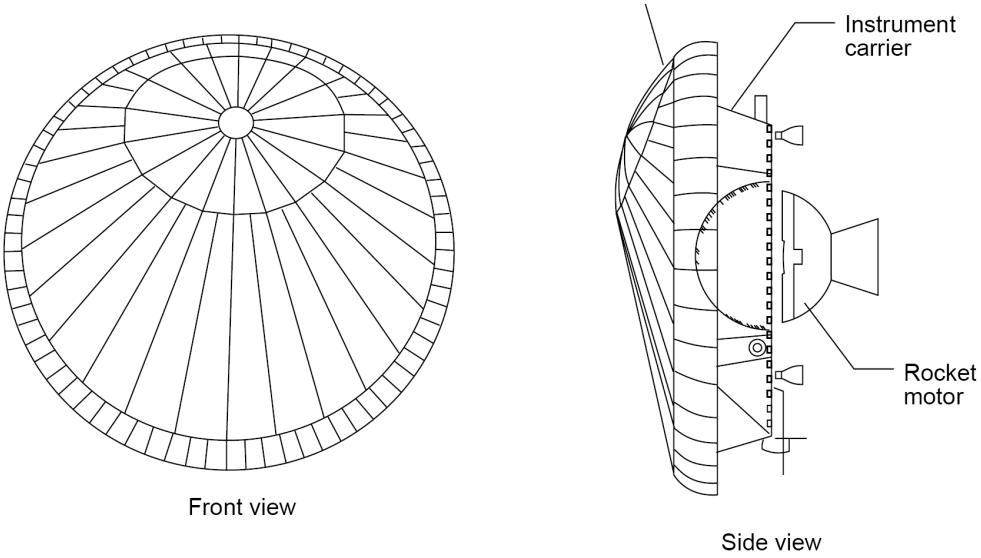

Figure 1.5. AFE flight vehicle configuration from Ref. [21].

At zero angle-of-attack, the *L/D* is approximately 0.30 while it is approximately 0.43 at $\alpha = -10^{o}$.[22] Wells presents the aerodynamic performance and shock shapes of the AFE from wind tunnel results in Ref. [22]. Micol gives the wind tunnel results for its hypersonic lateral and directional stability in Ref. [21] and discusses a simulation of real gas effects on the AFE in Ref. [23].

The biconic and bent biconic bodies have been looked at for an aero-assisted orbital-transfer vehicle application, but it can be argued that they can be used for planetary entry vehicle applications as well. The biconic heat shield is a spherically-blunted cone with an additional conical frustum that has a smaller half-cone angle. The bent biconic heat shield[24,25] has this conical frustrum tilted at an angle with the spherically-blunted cone as shown in Figure 1.6(a). Davies and Park[24] present the aerodynamics characteristics of a bent biconic with a fore half-cone angle of 12.84^{o} and an aft half-cone angle of 7^{o} tilted at 7^{o}. This configuration enables a blunt-nosed

body to have $L/D > 1$ at positive angle-of-attack as shown in Figure 1.6(b). Because of its slenderness due to its low half-cone angle, it can be argued that this is an atypical example of a blunt-body.

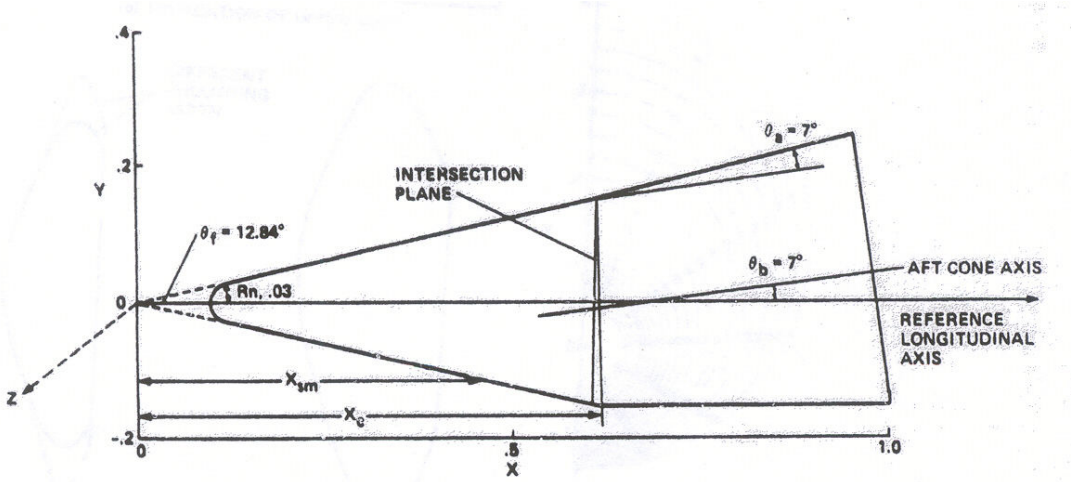

a) Bent biconic geometry

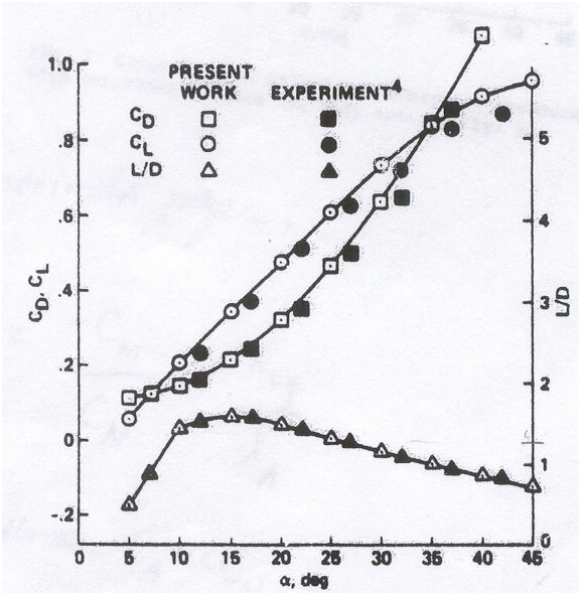

b) Aerodynamic characteristics

Figure 1.6. Bent biconic configuration from Ref. [24].

The common blunt-body produces positive L/D at negative angle-of-attack. Davies and Park acknowledge that a half-cone angle larger than 45^o is required to produces positive lift values at negative angle-of-attack for an axisymmetric

spherically-blunted cone. The reason for this is that at negative angle-of-attack, the axial force has a larger contribution to lift than the normal force. The axial force's contribution is positive while the normal force's is negative, thereby rendering positive lift. Slender designs are usually not considered for planetary entry because they produce higher heat transfer rates at the leading edges than blunter designs. Although the presented bent biconic configuration is slender, it will become a feasible design when more advanced high temperature materials are available. In fact, one could argue that this configuration could be feasible today if an ablative material is applied and if the nose radius-of-curvature is larger than that of the edge of the Apollo CM's heat shield, which was the location of highest heat transfer (not the stagnation point). Either way, its forebody half-cone angle can be easily modified for planetary entry applications.

Other more recent vehicle geometries are the parashield and the Slotted Compression RAMP probe. The parashield is a flexible, umbrella-like planetary entry, aerobrake, or aeroassist vehicle.[26] Magazu, Lewis, and Akin completed an analysis of a parashield with a ballistic coefficient of 181 Pa composed of twelve radial spars for LEO re-entry. This configuration has a mass of 150 kg and could be scaled by at least a factor of ten if desired. They determined that this parashield has a hypersonic *L/D* of 0.18 at $\alpha = 15^{o}$ and that there is increased pressure at each spar whether or not concavity exists.[26] The portability of this geometry in closed configuration is a feature unique to parashield and inflatable ballute geometries.

Murbach[27] has examined the Slotted Compression RAMP (SCRAMP) probe, which has undergone several sub-orbital test flights under his supervision. This

geometry has a long cylindrical forebody with a hemispherical nose and an aft flare of high half-cone angle ($\approx 70^{o}$) attached to the rear of the vehicle. The aft flare creates most of the drag on the vehicle but also produces a compression ramp leading to flow recirculation. As a result, several slots are placed where the aft flare meets the cylindrical fore body to minimize the flow recirculation and thereby increase vehicle drag.

The payload in the SCRAMP probe is located inside the front of the cylindrical forebody in order to place the center of gravity far forward. Since the aft flare produces most of the drag on the vehicle, the location of the center of pressure is far behind this center of gravity, rendering a negative $C_{m,cg,\alpha}$. Murbach observed that by increasing the slot size, the maximum pressure on the aft shield is increased. This configuration has a negative $C_{m,cg,\alpha}$ which is considerably better than the Apollo CM's value of -0.143/rad,[9] rendering an outstanding, longitudinally stable entry vehicle. Note that the described configuration does not produce significant lift but may be designed to in future flight tests.

Several of the classic and more recent design configurations were analyzed as lunar-return planetary entry applications in the work of Whitmore.[28] Whitmore's computational results for aerodynamics and stability are consistent with the results presented in this thesis. Bertin[29] provides a thorough overview and several correlations concerning hypersonic aerothermodynamics, and Rasmussen[30] provides an in-depth look at hypersonic aerodynamics.

1.2.2. Heat Transfer

Extremely high heat transfer rates may be experienced during planetary entry. Since the PEV undergoes high heat transfer rates for several minutes, the heat transfer load is equally important.

In this section general references for planetary entry heat transfer are first mentioned. Since the heat transfer results of this work consist of stagnation-point heat fluxes, the corresponding references are mentioned and referred to throughout the text. For calculating the heat flux, there are more sources and emphasis in this work given to radiation than convection because radiation is an ongoing research topic. The drawback of this work is that the heat load is not determined, but it is mentioned as an important topic for future work.

In recent analyses, Park[31] and Rochelle[32] discuss the aerothermodynamic environments for Mars entry and return, as well as lunar return. Park presents an analysis of two human missions (one is 330 days and the other is 436 days) to Mars and notes that the existence of an optimum nose radius for the tradeoff between convective and radiative heat transfer. Rochelle analyzes several capsule geometries including the biconic and modified AFE aeroshell capsules for Mars entry and notes that with an increase in entry velocity from 10 km/s to 12 km/s, the radiative heat flux goes from 13% to 42% of the total heat flux.

Two classic references from Rose[33] and Kemp[34] at the Avco-Everett Research Laboratory give a general overview of stagnation-point and laminar heat transfer in dissociate air. Kemp notes that the maximum heat transfer flux can be larger than the stagnation-point heat flux, as is the case for a flat-nosed body in which the convective

heat transfer flux is approximately 30% larger at the corner than that at the stagnation-point. This is noticed in the wind tunnel results for the Apollo CM presented by Lee,[35] in which the corner has a heat flux that is 80% larger than at the stagnation-point at $\alpha = 33^{o}$ at $M_{\infty} = 9.07$. The main Apollo missions that included the astronauts did not re-enter at 33^{o}, and so the maximum heating rate was lower. This wind tunnel test was completed to find out the worst-case scenario with the crew compartment (aftbody) being tangent with the freestream flow. Lee also offers a thorough explanation of the convection and radiative heat transfer and gives the heat flux and pressure distributions about the heat shield. Note that the radiative heat flux correlation is analyzed in Chapter 6, but is not recommended for use since there are simpler correlations that follow the Apollo flight data better.

Two Apollo CM were instrumented for aerothermodynamic analysis. Lee[36] compares the flight results from superorbital entry, as is the case in lunar return, with predictions (note that Ref. [35] was written before the Apollo missions were completed). Lee also gives an aerothermodynamic evaluation in Ref. [37] that presents the highlights of the re-entry aerodynamics and heat transfer for the Apollo missions.

The heat shield of the Apollo CM is the main part of the Apollo's Thermal Protection System (TPS). Pavlosky[38] details the history of designing the Apollo TPS and the manufacturing process. Also, he includes a summary of the predicted maximum heat transfer rates and loads for Apollo missions 8 and 10-16. Park and Tauber[39] provide a current review of heat shielding problems experienced by the Apollo 4, 6, Pioneer-Venus, and Galileo Probe missions. Also, Scotti[40] presents a

compilation of TPS technologies that were current in 1992 including the shuttle tiles, a TPS design for the cancelled NASA Aeroassist Flight Experiment (AFE), and proposed future materials.

The amount of stagnation-point heat transfer is one of the main aerothermodynamic benchmarks for comparing the capability of one entry vehicle to another. The stagnation-point heat transfer is not necessarily analogous with the point of maximum heat transfer, as was the case for the Apollo CM and the flat-nosed body. As a result, a more appropriate benchmark would be to compare the point of maximum heat transfer. Because this requires a more computationally expensive process that is beyond the focus of this thesis, previous work concerning the convective and radiative heat transfer at the stagnation-point has been acquired.

Lovelace[41] provides correlations for both convective and radiative heat transfer at the stagnation point; it will be shown in Chapter 6 that the radiative heat transfer correlation is one of two that matches the Apollo flight data the closest.

For convective heat transfer, Tauber[42] provides the stagnation-point, laminar and turbulent flat plate correlations that he validates against the US Space Shuttle heating rates. Tauber applies the well-known Fay and Riddell[43] relation that assumes that convection is inversely proportional to the square root of the nose radius. This would suggest that the convective heat transfer approaches zero as the nose radius is increased, but Zoby[44] notices that blunt bodies have more enthalpy than expected by this theory. Zoby shows that an adjustment that is based on the change in the velocity gradient from that of a hemisphere can produce an effective radius that can be applied to improve the theory's accuracy.

For radiative heat transfer, Tauber[45] also provides the stagnation-point correlations for Earth and Mars entries. This is one of the two correlations that match the Apollo flight data the closest. Originally, Tauber's correlations were not meant to be applied to the entire altitude regime on Earth, but this thesis will show that there is not much difference from Lovelace's correlation[41] when following the Apollo 4 trajectory. A review of the stagnation-point radiation from the Apollo 4 is available by Park.[46]

Cauchon[47] provides the radiative heating results from the Second Flight Investigation of the Reentry Environment (FIRE II) experiment at the superorbital entry velocity of 11.4 km/s (37,400 ft/s), which is slightly larger than the fastest Apollo entry at 10.7 km/s (35,000 ft/s) for Apollo 4.[7] Cauchon compares the theory to the few flight test data points. The FIRE II had three spherical-segment heat shields layered over each other. After initiating planetary entry, heat transfer data is obtained for the first heat shield. Then it is jettisoned from the entry vehicle at a chosen point in the trajectory, leaving the second heat shield surface to face the freestream flow. Data is obtained for the second heat shield, and then it is jettisoned, leaving the third heat shield surface to protect the vehicle for the remainder of the trajectory. The three heat shields had different nose radii: 0.935 m, 0.805 m, and 0.702 m for the first through third heat shields respectively. Cauchon shows that the theory is closer to the FIRE II calorimeter data by accounting for radiation cooling and coupling; otherwise, the theory overshoots the calorimeter data by 30%.

Ried[48] compares the flight measurements and engineering predictions on the Apollo CM for mission four. Ried also provides a computational approximation of

the total radiative heating rate near the stagnation point including ultraviolet lines and continuum, which were not measured by the radiometers on the heat shield of Apollo 4. The shock-standoff distance over the time of maximum radiative heat transfer is also provided. A correlation that closely matches the behavior of how the stagnation-point shock standoff distance varies with normal-shock density ratio is included and could be used along with Lovelace's[41] or Tauber's[45] correlations to calculate stagnation-point heat transfer fluxes. For planetary entry at velocities larger than that of the Apollo missions, curve fits of inviscid heating rates and cooling factors have been produced by Suttles.[49] It is recommended that these curve fits be validated before use in future work.

Determining how the stagnation-point radiative heat transfer rate varies as a function of angle of attack for the Apollo CM is investigated by Walters.[50] By accounting for the stagnation-point shock-standoff distance, Walters is able to approximate this behavior, although the wind tunnel data is noticeably scattered. Additionally, he applies Kaattari's correlation[51] to produce an outstanding match of the Apollo CM's experimental shadowgraph of the shockwave shape at Mach 19.5 and 31.5^{o} angle of attack.

The Kaattari method approximates the shock-standoff distance of a blunt-body at zero angle of attack[52] and the shock envelope of spherical-segment blunt-bodies at large angles of attack.[51] This highly empirical method uses the normal shock density ratio to approximate the location of the sonic line on the body as well as the shock and body surface inclinations at the sonic point along with theory to determine the ratio of the shock-standoff distance to the nose radius. Since a planetary entry

vehicle enters the atmosphere at high velocities, high temperatures are produced in front of the heat shield, and so high temperature gas correlations from Srinivasan[53] (an updated version of the Tannehill[54] correlations) can be used to determine the effective specific heat ratio to determine the normal-shock density ratio. This thesis work applies the Kaattari method, with its implementation described in Chapter 3, to apply Lovelace's[41] and Tauber's[45] radiative heat flux correlations to blunt-bodies at any angle of attack.

1.2.3. Misconceptions

Misunderstandings and discrepancies in publications have been noticed throughout the literature survey. The most common misunderstanding is the theory behind calculating the *x*-location of the center of pressure of a blunt body. This location is dependent on both the axial force and normal force's contributions to the pitching moment; neither can be ignored. However, several references calculate the *x*-location by assuming the axial force's contribution to the pitching moment is negligible. This thesis explains in Chapter 3 that the axial force's contribution to the pitching moment is at least the same order of magnitude as the normal force's contribution and thereby must be accounted for in the case of a blunt body. From here, it is possible to match the Apollo CM's pitching moment wind tunnel data as will be shown in Chapter 6.

Bertin,[29] Rasmussen,[30] and Regan[55] have textbooks that assume the axial force's contribution to the pitching moment is negligible in sections concerning blunt bodies. However, Bertin's textbook[29] also has the correct derivation, and the example

in which the assumption is made in the first edition of Regan's textbook[55] has been removed from Regan's second edition.

Figure 9 in the work of Levine[56] provided the *x*-location of the center of pressure of several spherical and blunt cone geometries. However, they are different from the values of this thesis by one order of magnitude except for one case. Because the work of this thesis was able to match the aerodynamic and stability results of the Apollo wind tunnel and flight test data and basic conical shapes, the use of Levine's values of the *x*-location is not recommended.

Arora[57] maximizes the center of pressure's *x*-location for a spherically-blunted cone-flare configuration. However, Arora's work assumes that the axial force's contribution to the pitching moment is negligible. As a result, the optimized *x*-location value is infeasible. Because the *x*-location is incorrect, it is not possible to find the correct pitching moment value about the blunt-body's center of gravity. An active researcher concerned with the aerodynamic performance and the stability of blunt-body planetary entry geometries should be attentive to this issue.

Papadopoulos[58,59] has figures that are mislabeled as trajectories for Apollo missions AS-201, 4, and 6. The only relations between the figures and the Apollo missions are the mentioned missions' entry flight-path angles. The plots are meant to show code output according to a particular Apollo mission's entry flight-path angle. Because several plots on a single page have legends with Apollo mission numbers, it is easy for one to assume that these must be the flight velocities, decelerations, and Reynolds numbers experienced by the Apollo missions listed. This is a simple

miscommunication and not suggesting that Papadopoulos's results are not accurate; he has validated his results with POST.

Several sources that are not suggested for estimating the radiative heat transfer at the stagnation-point for an Apollo-like capsule include Barter[60] and Gupta.[61] It is possible that both sources have typographical errors in the equations, but this is not certain. However, it is shown in Chapter 6 that these equations do not match the behavior of flight test data from Apollo 4. There are other correlations that match the flight test data closely.

1.3. Research Objectives

The primary objective of this research is to determine if and how the aerodynamic performance, static stability, and stagnation-point heat transfer can be improved over those of previously developed blunt-body planetary entry vehicles. Running a computerized optimization over a range of heat shield geometries is one way to efficiently search an entire design space for such an answer. Ideally, this design space would be controlled by several geometric parameters that could vary the shape of the heat shield to a great extent.

The classic spherical-segment and spherically-blunted cone heat shield geometries were originally developed since these shapes are simple yet satisfy the mission requirements of Apollo and Viking respectively. Another common shape is the power law that has been applied to reduce drag on the nose of hypersonic missiles. One of the goals of this research is to explore a wide design space, one beyond that of previous work. This is accomplished by extending these geometries to

vary eccentricity and transform the base cross-section shape from an ellipse to any rounded-edge polygon.

There are indications that better aerothermodynamic performance is possible, and using today's technology, it is possible that these heat shields could be produced at costs similar to reproduction costs of previous work. All of the past heat shield geometries except for the raked cone and the bent-biconic configuration are axisymmetric designs. The main advantages of the raked cone and the bent-biconic are their larger lift-to-drag ratios compared to their axisymmetric counterparts, and so it is expected that the non-axisymmetric designs will produce higher lift-to-drag ratios. It is also possible that an optimum nose radius exists that could reduce the heat transfer load on the vehicle during lunar or Mars return. These questions are answered in this work, limited to the blunt-body's hypersonic performance.

1.4. Thesis Overview

This thesis is organized to first introduce the investigated blunt-body geometries and their geometric parameters in Chapter 2. Then Chapter 3 describes the Newtonian aerodynamic theory and a method for approximating the shock-standoff distance from the stagnation point. It also includes the equations for determining the static stability of a given heat shield geometry and provides explanations for a couple misinterpretations of basic theory. Chapter 4 gives the main assumptions and correlations for convective and radiative heat transfer at the stagnation point. A description of the code's layout and the chosen optimization process is included in Chapter 5. Then the design code is validated against Apollo wind tunnel and flight

test data in Chapter 6. In order to better understand the design space, a parametric analysis has been conducted. The results are included in Chapter 7 and happen to provide better initial designs for optimization. Chapter 8 presents the optimized configurations of this work in detail, and the final conclusions of this thesis along with suggested future work are detailed in Chapter 9.

Chapter 2. Blunt-Body Heat Shield Geometries

Each heat shield in this work is defined by two geometries: the base cross-section of the heat shield and the axial shape that is swept about the central axis and modified to match the base cross-section. The coordinate system for this work is included in Figure 2.1 with the sweep angle ω and conventional directions for positive moments. One change from convention that is not shown occurs when the vertical lift coefficient $C_{L,V} < 0$, in which the direction of the positive rolling moment switches in order for a negative $C_{l,\beta}$ to still indicate a statically roll stable shape. An explanation of the sign reversal is included in the stability section of Chapter 3.

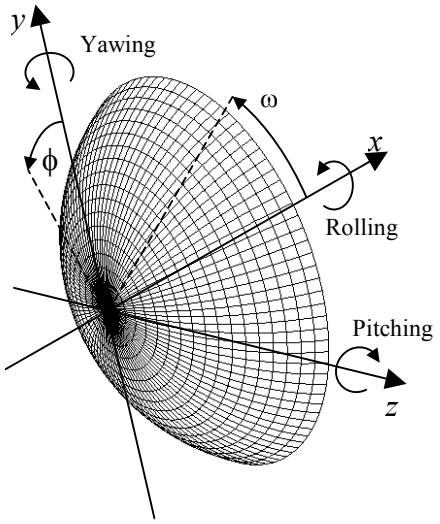

Figure 2.1. Fixed-body coordinate system, spherical-segment, $\omega = 30^o$, $\theta_s = 60^o$, $n_2 = n_3 = 2$.

2.1. Axial Shapes

The shape of the heat shield that protrudes from the base is called the axial shape in order to easily differentiate the protruded shape from the cross-section. The axial shape of the heat shield by itself represents the shield's profile if its base cross-

section were to be circular. If the base cross-section is not circular, then the axial shape is at least the top half of the shields profile at sweep angle $\phi = 0^o$. Then the axial shape is modified to follow the outline of the base cross-section. Three axial shapes: the spherical-segment, the spherically-blunted cone, and the power law are applied in this work and described in the following sections along with how they are generated.

2.1.1. Spherical-segment

A general spherical-segment is a region of a sphere that is left after the sphere is cut by two parallel planes. A closed spherical-segment is a region of a sphere encompassed by spherical-segment angle θ_s, in which $\omega = 90^o - \theta_s$, in which only one plane, parallel to the *yz*-plane divides the sphere. A closed spherical-segment, one shown in Figure 2.1, is also known as a spherical cap and is the type that is applied to previous and present heat shield design.

For this work, only the profile of the spherical-segment is utilized by using the following equations for the *xy*-plane at zero sweep angle:

$$r_{max} = x_{max}/(1-\cos(\theta_s)), \tag{2.1}$$

$$x_k = r_{max}(1-\cos(\theta_k)), \tag{2.2}$$

$$y_k = r_{max}\sin(\theta_k), \tag{2.3}$$

in which $x_{max} = 1$ in order to normalize the geometry to the length of the heat shield $l = x_{max}$. This set of equations produces the axial shapes shown in Figure 2.2 (a) for

the Apollo CM (θ_s = 25°) and a hemisphere (θ_s = 90°). The corresponding spherical heat shields, which have circular cross-sections, are shown in Figure 2.2 (b) and (c).

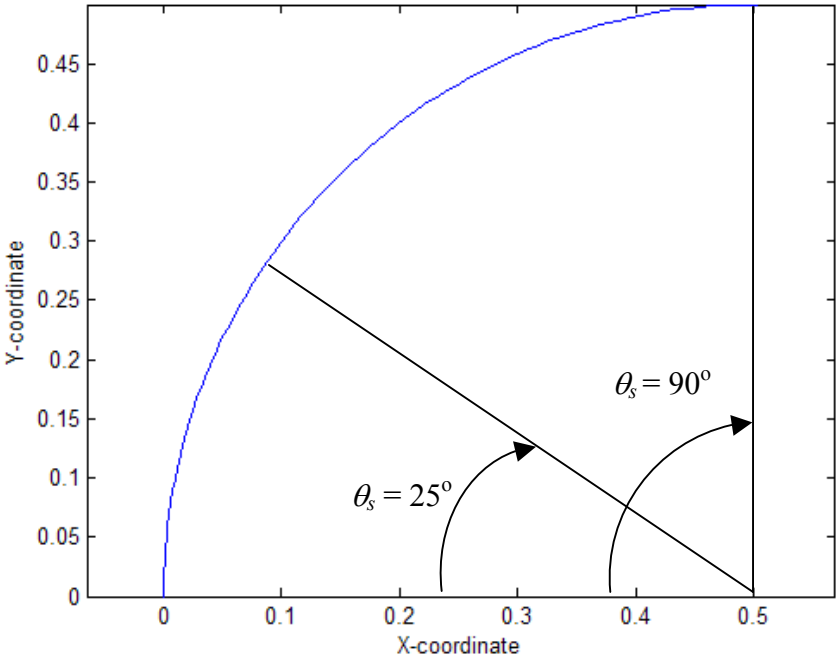

a) Spherical-segment axial profiles at $\phi = 0^o$.

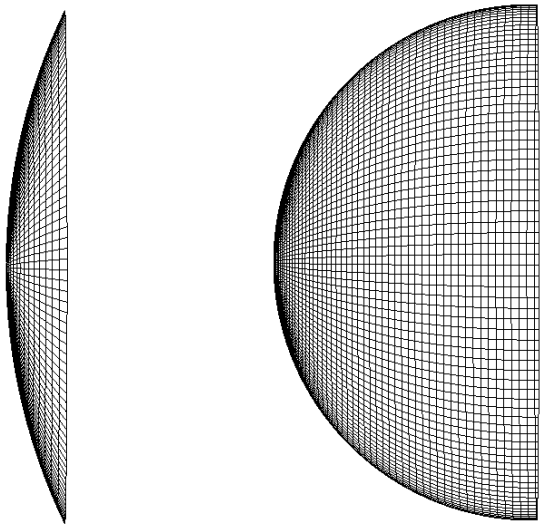

(b) Spherical heat shield, $\theta_s = 25^o$. **(c) Spherical heat shield, $\theta_s = 90^o$.**

Figure 2.2. Spherical axial profiles and heat shields.

2.1.2. *Spherically-blunted Cone*

The spherically-blunted cone's geometric parameters have been introduced in the previous work section of Chapter 1. Figure 1.1(b) is an example of the spherically-blunted cone heat shield. Its axial profile has two parts, a spherical nose and the conical body. The spherical nose is generated by producing a spherical-segment with $\theta_s = \pi/2\text{-}\theta_c$ to provide slope continuity from the spherical nose to the conical body. If the conical base is divided into N vertical sections that are equally spaced along the x-direction, then the spherically-blunted cone profile in the xy-plane is generated with the system of equations

$$x = \begin{cases} r_n(1-\cos\omega), & 0 \le \omega < \theta_s \\ r_n(1-\cos\omega-\sin\omega) + y/\tan\theta_c & \omega = \theta_s, \end{cases} \tag{2.4}$$

$$y = \begin{cases} r_n \sin\omega & 0 \le \omega < \theta_s \\ r_n \sin\omega + \dfrac{\frac{1}{2}d - r_n\sin\omega}{N} n & \omega = \theta_s, 0 \le n \le N. \end{cases} \tag{2.5}$$

Also, the spherical-segment can be produced using only the first equation for both x and y over the range $0 \le \omega \le \theta_s$.

2.1.3. *Power Law*

The power law offers axial shapes with a wide range of bluntness controlled by coefficient A and exponent b with the equation

$$y = Ax^b. \tag{2.6}$$

The effects of varying these two parameters are shown in Figure 2.3. For a fixed value of b, increasing the slenderness ratio A increases the bluntness of the shape. As

a result, the effects of increasing the slenderness ratio should be similar to those of decreasing the spherical-segment angle θ_s or increasing the spherically-blunted cone angle θ_c.

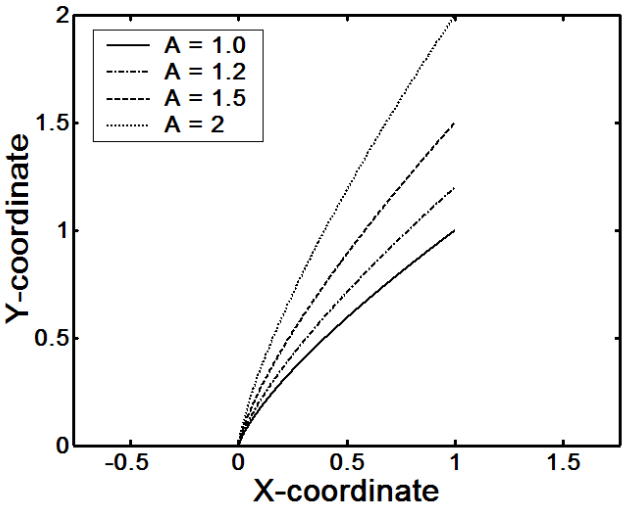

(a) Axial profile varying *A*, *b = 0.75.*

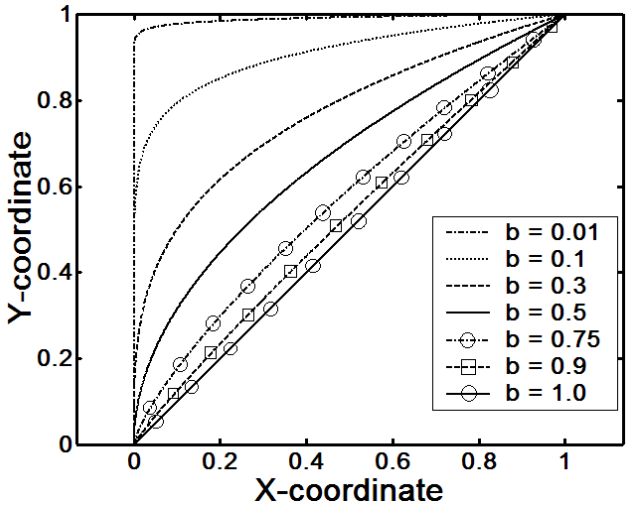

(b) Axial profile varying *b*, *A* = 1.

Figure 2.3. Power law axial shape.

For a fixed value of A, increasing the value of exponent b from 0.01 to 1.0 transforms the axial shape from a flat nosed body to a sharp cone respectively. As a result, a power law shape with b = 1.0 is equal to a sharp cone with a corresponding

angle θ_c. The power law can also nearly match the spherical segment for a given set of A and b or it could produce profiles that are different from these two classic shapes.

Rasmussen[30] mentions that two minimum drag power-law bodies have exponent values of two-thirds and three-fourths based on Newton-Busemann and Newtonian surface pressure models.

When calculating the shock-standoff distance, special cases account for this heat shield shape having a discontinuity at the tip ($x = 0$) and are discussed in Chapter 3. Varying the power law's slenderness ratio and exponent should render a wide range of aerodynamic performance and stability characteristics.

2.2. *Cross-section Shapes*

The cross-section shape is the geometry of the heat shield's base. The base cross-section is usually chosen to be circular although there have been a couple cases of slightly elliptic cross-section including the AFE.[22] For optimization, it would be ideal to have a base cross-section equation that can generate a wide-range of shapes. In order to produce eccentric base cross-sections, the equation of the ellipse can be applied. To produce shapes that range from a parallelogram to an ellipse, Sabean[62] uses the following Cartesian equation for a typical superellipse curve:

$$\left|\frac{x}{a_1}\right|^v + \left|\frac{y}{b_1}\right|^v = 1, \tag{2.7}$$

By varying v from 1 to 2, the superellipse can transform from a parallelogram to an ellipse.

In 2003, Gielis[63] published a more generalized superellipse equation called the superformula; it can transform a polygon into an ellipse and then into a rounded-edge concave polygon. It defines the cross-section radius for $0 \le \phi \le 2\pi$:

$$r(\phi) = \left[\left| \frac{\cos\left(\frac{1}{4} m\phi\right)}{a_1} \right|^{n_2} + \left| \frac{\sin\left(\frac{1}{4} m\phi\right)}{b_1} \right|^{n_3} \right]^{-1/n_1}, \qquad (2.8)$$

in which m corresponds to the number of sides of a polygon, n_1 and n_2 are modifiers, and n_3 is set equal to n_2 to produce sharp or rounded-edge polygons. In the present work, n_2 was set to 1, and then values of n_1 that produced sharp-edged, non-concave polygons were determined. Corresponding values of n_2 for rounded-edge polygons were then determined. Because of the increased heat transfer that would be produced on sharp edges, zero radius-of-curvature polygons were not considered. Setting $n_2 = 2$ produces an ellipse; increasing n_2 beyond 2 will produce concavity in the shape. Table 2.1 presents the values for m, n_1, n_2, and n_3 to produce rounded-edge polygons, both straight and concave.

Table 2.1. Superformula parameters for rounded-edge polygons ($n_3 = n_2$).

m	n_1	n_2
4	1.00	1.50 — 4.0
5	1.75	1.50 — 4.0
6	2.30	1.50 — 4.0
7	3.20	1.50 — 5.0
8	4.00	1.40 — 6.0
9	5.50	1.40 — 6.0
10	7.00	1.40 — 7.0

The cross-sections in this analysis include polygons ranging from four to ten sides. Once m and n_1 are set, n_2 can be varied to transform a polygon into an ellipse

and then into a concave polygons, in which $n_3 = n_2$. With the parameters in Table 2.1, the cross-sections in Figure 2.4 can be constructed. If a rounded-edge pentagon is constructed, as shown in Figure 2.4(d), then n_2 can be increased to 2 in order to produce the corresponding ellipse in Figure 2.4(b), and then n_2 can be increased to 4 to produce the rounded-edge concave pentagon in Figure 2.4(e).

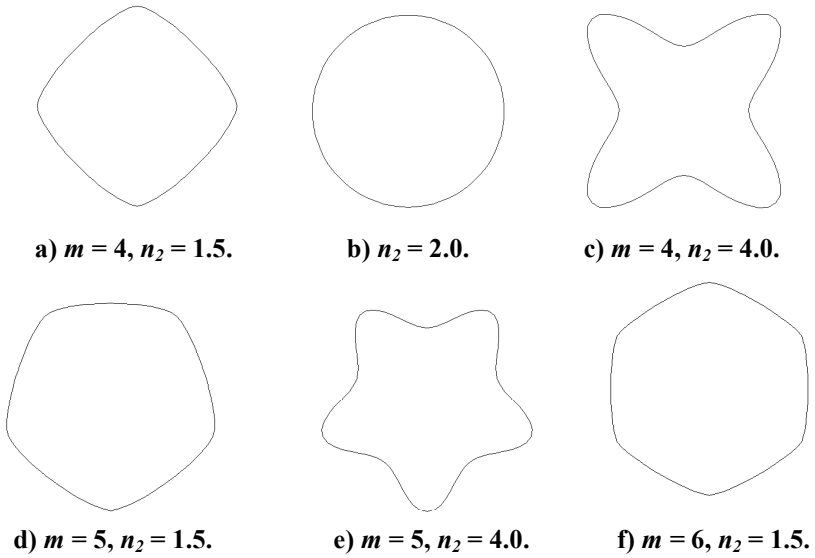

a) $m = 4, n_2 = 1.5$. **b)** $n_2 = 2.0$. **c)** $m = 4, n_2 = 4.0$.

d) $m = 5, n_2 = 1.5$. **e)** $m = 5, n_2 = 4.0$. **f)** $m = 6, n_2 = 1.5$.

Figure 2.4. Cross-section shapes produced using parameters from Table 2.1.

If $a_1 = b_1 = 1$, the cross-section will have no eccentricity, and so $n_2 = 2$ will produce a circular cross-section. Because a_1 and b_1 in Eqn. (2.8) relate differently to eccentricity than they do in Eqn. (2.7) for $v = 1$, it was concluded that it is easier to produce an eccentric heat shield by multiplying either a_1 or b_1 by the cross-section radius r when generating the blunt body as described in the next section.

2.3. *Generating Blunt-Bodies*

Once the axial shape at $\phi = 0^o$ is rendered, it is swept about the central body axis (the x-axis) according to the chosen base cross-section with Eqn. (2.8) according to the following three-dimensional equation set

$$\begin{cases} x_{j,k} = x_k \\ y_{j,k} = a_2 r_{j,k} \cos(\phi_j) \\ z_{j,k} = b_2 r_{j,k} \sin(\phi_j), \end{cases} \tag{2.9}$$

in which j and k are indices, r is the radius at a given j,k location, and a_2 and b_2 are the lengths of the semimajor and semiminor axes of the generated blunt body. In this work, eccentricity e has a range in-between –1 and 1, in which $e < 0$ corresponds to oblate geometries and $e > 0$ corresponds to prolate geometries. The semimajor and semiminor axes are determined from the following equation sets

$$a_2 = \begin{cases} b_2\left(1-e^2\right)^{\frac{1}{2}} & -1 < e < 0, \\ 1 & 0 \le e < 1, \end{cases} \tag{2.10}$$

$$b_2 = \begin{cases} 1 & -1 < e < 0, \\ a_2\left(1-e^2\right)^{\frac{1}{2}} & 0 \le e < 1. \end{cases} \tag{2.11}$$

The superformula cross-section equation reflects the shapes made by $n_2 > 2$ about the horizontal axis. As a result, to keep consistency when varying n_2, the reflection was removed by setting $y_{j,k} = - y_{j,k}$ and $z_{j,k} = -z_{j,k}$.

Examples of generated blunt bodies are included to show the variety of shapes that can be created from this set of axial and cross-section shapes. Figure 2.5 shows a prolate (approximately 4:1 axes length ratio) spherically-blunted cone blunt body. Figure 2.6 shows an oblate (approximately 3:1 axes length ratio) 12-sided polygon blunt body with a spherical-segment axial profile. Figure 2.7 shows a slightly prolate, concave rounded-edge pentagon with a power law axial profile. Note that the angled views do not correspond to any specific orientation.

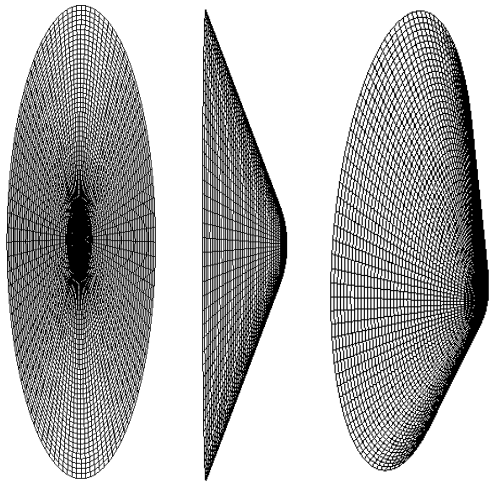

a) Front view. b) Side view. c) Angled view.

Figure 2.5. Spherically-blunted cone, r_n/d = 0.25, θ_c = 70°, e = 0.95, m = 5, n_1 = 1.75, n_2 = 2.

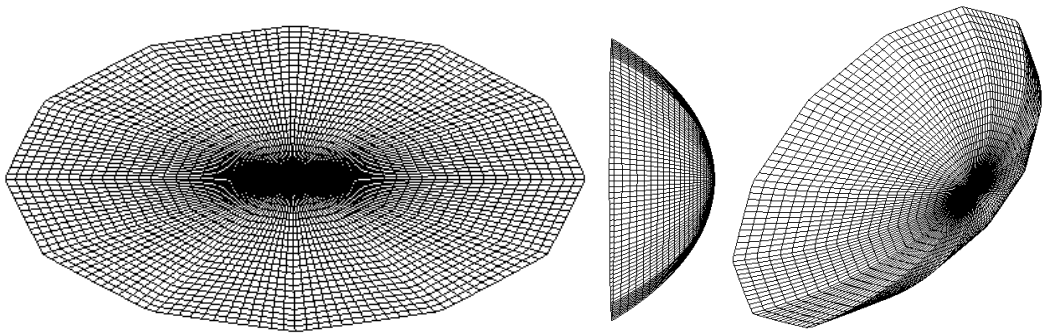

a) Front view. b) Side view. c) Angled view.

Figure 2.6. Spherical-segment, θ_s = 40°, e = -0.85, m = 12, n_1 = 10.75, n_2 = 1.

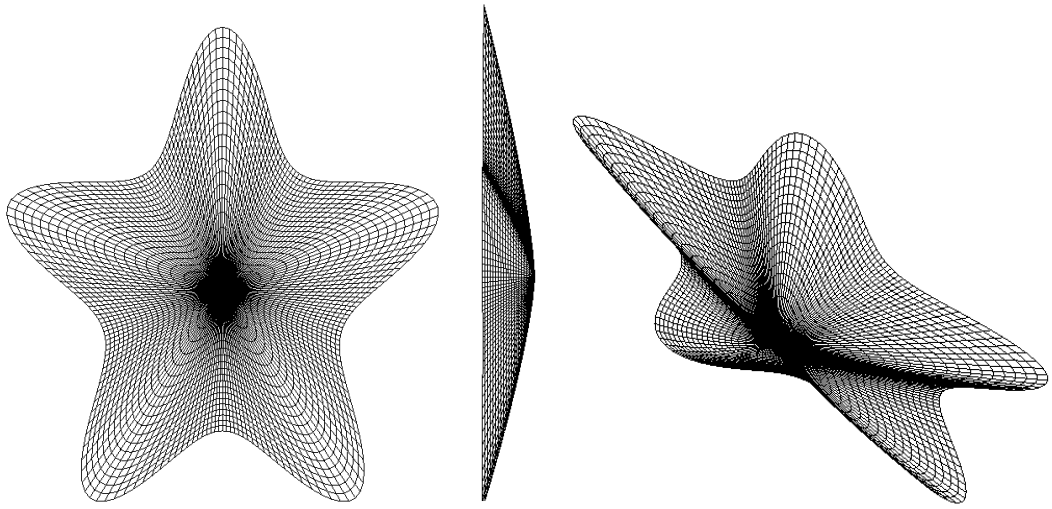

a) Front view. b) Side view. c) Angled view.

Figure 2.7. Power law, A = 3, b = 0.75, e = 0.5, m = 5, n_1 = 1.75, n_2 = 5.

2.4. *Geometric Properties*

The main geometric properties calculated in this work are the surface and planform areas, the volume, the volumetric efficiency of the heat shield, and the location of the center of gravity. The following is a description of how the areas and volume are determined. Each point (*j,k*) is a part of a quadrilateral with four points (*j,k*), (*j-1,k*), (*j,k-1*), and (*j-1,k-1*). The distance between points (*j,k*) and (*j-1,k*) is indicated by $d_{1,a}$,

$$d_{1,a} = \sqrt{\left(x_{j,k} - x_{j-1,k}\right)^2 + \left(y_{j,k} - y_{j-1,k}\right)^2 + \left(z_{j,k} - z_{j-1,k}\right)^2}, \tag{2.12}$$

and the distance between points (*j,k-1*) and (*j-1,k-1*) is $d_{1,b}$. These two distances are then averaged to produce d_1. The distance between points (*j,k*), and (*j,k-1*) is $d_{2,\mathrm{a}}$, and the distance between points (*j-1,k*) and (*j-1,k-1*) is $d_{2,b}$. Likewise, they are averaged to produce d_2.

The product of d_1 and d_2 is the differential surface area dA. All the differential surface area components are summed to produce surface area S_{hs}, which is a term in determining the volumetric efficiency described later in this section. The differential planform area dA_p is the product of w_1 and w_2, which are the distances from and to the same point-locations as d_1 and d_2 if they were assumed to have equal *x*-components. In other words, the planform area dA_p, which is equal to part of the heat shield's base area, depends only on the area projected onto the *yz*-plane, in which

$$w_{1,a} = \sqrt{\left(y_{j,k} - y_{j-1,k}\right)^2 + \left(z_{j,k} - z_{j-1,k}\right)^2}, \tag{2.13}$$

and likewise for $w_{1,b}$, $w_{2,a}$, and $w_{2,b}$. Then the sum of the differential planform areas is equal to the heat shield's base area. The planform area is used in part to non-dimensionalize the aerodynamic forces and moments.

The differential volume is the product of the differential planform area and the distance from the differential surface to the shields base written as l_b

$$l_b = x_{\max} - \left(\frac{x_{j,k} + x_{j,k-1} + x_{j-1,k} + x_{j-1,k-1}}{4} \right). \tag{2.14}$$

Then a summation of all the differential volumes produces the volume of the heat shield V_{hs}.

The volumetric efficiency is one way to benchmark how much volume is available for a given amount of surface area. In the case of a heat shield shape, which is not a closed-shape, the volumetric efficiency is normalized to a hemisphere

$$\eta_v = \frac{(18\pi)^{1/3} V_{hs}^{2/3}}{S_{hs}}. \tag{2.15}$$

As a result, the most volumetrically efficient shape is the non-eccentric spherical-segment with $\theta_s = 90^o$.

The following equations calculate the location of the center of gravity of a uniform density body

$$\left\{ X_{cg}, Y_{cg}, Z_{cg} \right\} = \left\{ \frac{\rho \iiint x dV}{\iiint dV}, \frac{\rho \iiint y dV}{\iiint dV}, \frac{\rho \iiint z dV}{\iiint dV} \right\}. \tag{2.16}$$

This equation is applied to a 3D mesh through numerical integration. One numerical integration method is Simpson's rule,[64]

$$F(x) = \int_{x_1}^{x_{2n+1}} f(x)dx \tag{2.17}$$

$$\approx \frac{h}{3}\left(f_1 + 4\left(f_2 + f_4 + \ldots + f_{2n}\right) + 2\left(f_3 + f_5 + \ldots + f_{2n-1}\right) + f_{2n+1}\right),$$

which is fifth-order accurate in *h*. For this work, *h* is a space step size. Additionally, this method requires an odd number of points to be integrated, and so the final point in the mesh is represented by the index 2*n*+1. Because the space step *h* may not necessarily be the same for each pair of points, this work applies a modified version of Simpson's Rule that uses individual step sizes.

$$F(x) = \int_{x_1}^{x_{2n+1}} f(x)dx \tag{2.18}$$

$$\approx \frac{1}{3}\left(h_1 f_1 + 4\left(h_2 f_2 + h_4 f_4 + \ldots + h_{2n} f_{2n}\right) + 2\left(h_3 f_3 + h_5 f_5 + \ldots + h_{2n-1} f_{2n-1}\right) + h_{2n+1} f_{2n+1}\right).$$

It is likely that more than one integration is required to determine each term of the center-of-gravity location since the triple integrals indicate a three-dimensional shape that requires integration in three directions. It is easier to use the polar coordinate system in Figure 1.1(a). This allows one to conduct two integrations instead of three.

The method applied in this work for determining the center of gravity's location with numerical integration is detailed in this section. In the applied form, the general equation that is equal to Eqn. (2.16) is

$$\left\{X_{cg}, Y_{cg}, Z_{cg}\right\} = \left\{\frac{f_{x,3}}{NVol}, \frac{f_{y,3}}{NVol}, \frac{f_{z,3}}{NVol}\right\}. \tag{2.19}$$

The term *NVol* is a volume-related term, but it is not necessarily equal to the volume of the heat shield. For the spherical-segment axial shape, *NVol* is equal to V_{hs}, but for

the spherically-blunted cone and power law axial shapes, *NVol* is equal to the terms that are not cancelled out from being common to the numerator and denominator of Eqn. (2.16). *NVol* is defined as

$$NVol = \sum_{k=1}^{k\max} \sum_{j=1}^{j\max} dNVol_{j,k}, \tag{2.20}$$

in which $dNVol_{j,k}$ is the differential volume-related term defined as

$$dNVol_{j,k} = \begin{cases} \frac{w_{j,k}^2}{2} d\phi_{j,k} dr_{j,k} \cos\left(\frac{\pi}{2} - \theta_k\right), & \text{Spherical - segment} \\ \frac{w_{j,k}^2}{2} d\phi_{j,k} dr_{j,k}, & \text{Spherically - blunted cone} \\ \frac{w_{j,k}^2}{2} d\phi_{j,k} dr_{j,k}, & \text{Power law,} \end{cases} \tag{2.21}$$

in which spherical-segment angle θ_k only varies with x-location, $d\phi_{j,k}$ is the differential sweep angle in the *yz*-plane. This differential angle is determined from the law of cosines

$$d\phi_{j,k} = \operatorname{acos}\left(\frac{w_{j,k}^2 + w_{j+1,k}^2 - d_{(j+1,k),(j,k)}^2}{2 w_{j,k} w_{j+1,k}} \right), \tag{2.22}$$

and $dr_{j,k}$ is the average of the distances between the points (*j+1,k*) and (*j+1,k-1*) and the points (*j,k*) and (*j,k-1*), which is the numerical analogue to a differential length,

$$dr_{j,k} = \frac{1}{2}\left(d_{(j+1,k),(j+1,k-1)} + d_{(j,k),(j,k-1)} \right). \tag{2.23}$$

Since there are two differentials in *dNVol,* it is noted that it will be integrated twice to produce the denominators of Eqn. (2.19). With these equations, the denominator is

fully defined. For the numerator, the subscript letter on the function f corresponds to the x, y, and z-components, and the subscript number 3 corresponds to the result after the two integrations. The subscript number 2 corresponds to the result after one integration, and the subscript number 1 corresponds to the initial case before integration. The initial variables $f_{x,y,z,1}$ that are integrated twice to produce $f_{x,y,z,3}$ are defined as

$$\left\{f_{x,1}, f_{y,1}, f_{z,1}\right\} = \left\{x_{j,k} dNVol_{j,k}, y_{j,k} dNVol_{j,k}, z_{j,k} dNVol_{j,k}\right\}. \tag{2.24}$$

These are integrated first with respect to ϕ, and there are a k_{max}-number of values for $f_{x,y,z,2}$

$$\left(f_{x,2}\right)_k = \left(\int_{x_1}^{x_{2n+1}} f_{x,1} \right)_k \tag{2.25}$$

$$\approx \left(\frac{1}{3}\left(f_{x,1,1} + 4\left(f_{x,1,2} + f_{x,1,4} + \ldots + f_{x,1,2n}\right) + 2\left(f_{x,1,3} + f_{x,1,5} + \ldots + f_{x,1,2n-1}\right) + f_{x,1,2n+1}\right)\right)_k,$$

and likewise for $f_{y,2}$ and $f_{z,2}$. Note that the $f_{x,1}$ includes the differentials $d\phi$ and dr, and thus they are not written in Eqn. (2.25) and (2.26). The $f_{x,y,z,2}$ are integrated with respect to r, and so there is one value for each component of f_3

$$f_{x,3} = \int_{x_1}^{x_{2n+1}} f_{x,2} \tag{2.26}$$

$$\approx \frac{1}{3}\left(f_{x,2,1} + 4\left(f_{x,2,2} + f_{x,2,4} + \ldots + f_{x,2,2n}\right) + 2\left(f_{x,2,3} + f_{x,2,5} + \ldots + f_{x,2,2n-1}\right) + f_{x,2,2n+1}\right),$$

and likewise for $f_{y,3}$ and $f_{z,3}$. With these definitions, the location of the center of gravity of a given three-dimensional shape can be determined.

Chapter 3. Aerodynamics and Static Stability

The theory behind the aerodynamics and the static stability is presented in this section. The aerodynamic characteristics are then transformed into the quantities that are applied in the code of this work. The method for determining the shock-standoff distance to the stagnation point is introduced also, and modifications to the method to account for angle of attack are stated. Then this chapter finishes with a couple corrected misinterpretations of general aerodynamic theory.

Two coordinate systems applied in this work are the freestream coordinate system shown in Figure 3.1(a) with the positive angle of attack and sideslip angle conventions, and the fixed coordinate system shown in Figure 3.1(b), which is slightly different from Figure 2.1.

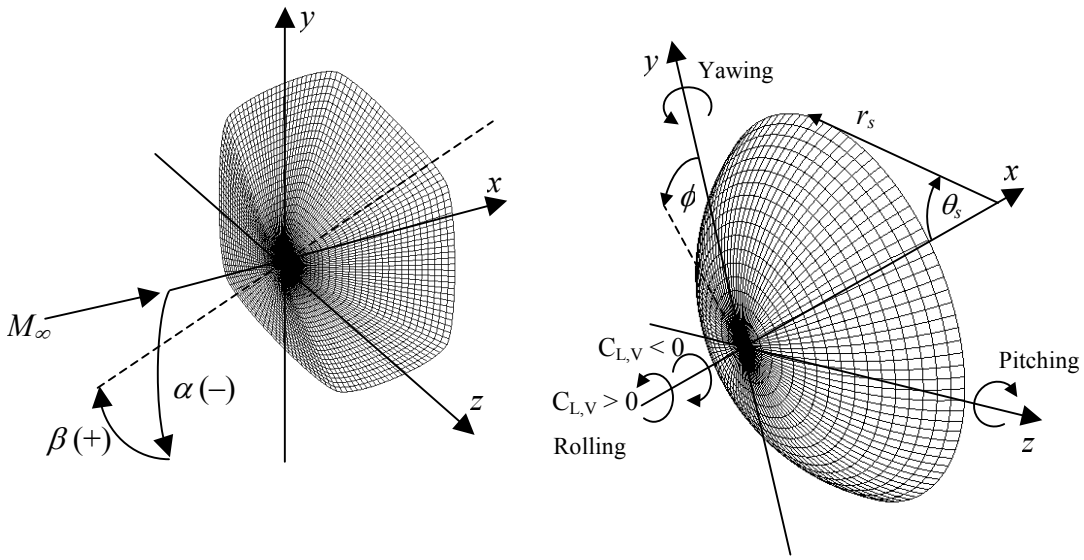

a) Freestream coordinate system with α and β. **b) Fixed coordinate system with aerodynamic moment conventions.**

Figure 3.1. Coordinate systems with positive α and β and moment conventions.

3.1. *Modified Newtonian Impact Theory*

After the heat shield geometry is generated, its aerodynamic characteristics are calculated based on a modified Newtonian surface pressure distribution. Simple Newtonian theory is equivalent to the limit of exact oblique shock theory as M_∞ approaches infinity and γ approaches one.[65] This work is currently being applied to Earth atmospheric entry by assuming $\gamma = 1.4$, and a similar analysis can be applied to a Martian atmosphere of CO_2 by assuming $\gamma = 1.3$. However, when calculating the shock-standoff distance, the effective specific heat ratio after the blunt-body shock is determined using the empirical correlations of high temperature air from Tannehill,[54] as explained in Section 3.2 on shock-standoff distance.

Because Newtonian theory allows aerodynamic performance to be determined within a fraction of a second of computation time, it has been chosen over more complicated, time-intensive methods for optimization reasons. Results from the code that apply modified Newtonian theory are compared to wind tunnel and flight test data from Apollo Command Module (CM) in Chapter 6.

The pressure coefficient, which is the pressure difference normalized by the dynamic pressure, is given by the equation

$$C_p = \frac{p - p_\infty}{q_\infty} = \frac{p - p_\infty}{\frac{1}{2}\rho_\infty V_\infty^2} = \frac{2}{\gamma M_\infty^2}\left(\frac{p}{p_\infty} - 1\right). \tag{3.1}$$

Newtonian theory assumes that the component of a particle's momentum that is normal to the surface is destroyed when impinging on the face of the blunt body while its tangential momentum is conserved.[29,30,55] The Newtonian model is

$$C_p = C_{p,\max}\left(\frac{\vec{V}_\infty \cdot \hat{n}}{V_\infty}\right)^2 \tag{3.2}$$

for $\vec{V}_\infty \cdot \hat{n} < 0$. The surface is in the aerodynamic shadow region when $\vec{V}_\infty \cdot \hat{n} \geq 0$ resulting in $C_p = 0$.

For simple Newtonian, the maximum value of the pressure coefficient is assumed equal to two. Modified Newtonian theory accounts for the maximum value $C_{p,max}$, according to the Rayleigh Pitot tube formula[66] that gives the ratio of the stagnation pressure after the shock to the freestream pressure

$$\frac{p_{0,2}}{p_\infty} = \left(\frac{1-\gamma+2\gamma M_\infty^2}{\gamma+1}\right)\left(\frac{(\gamma+1)^2 M_\infty^2}{4\gamma M_\infty^2 - 2(\gamma-1)}\right)^{\gamma/\gamma-1}. \tag{3.3}$$

This produces the following relation for $C_{p,max}$

$$C_{p,\max} = \frac{2}{\gamma M_\infty^2}\left(\frac{p_{0,2}}{p_\infty} - 1\right). \tag{3.4}$$

The velocity is modeled as a function of the angles of attack and sideslip

$$\frac{\vec{V}_\infty}{V_\infty} = \{V_x, V_y, V_z\} = \{\cos(\alpha)\cos(\beta), \sin(\alpha)\cos(\beta), \sin(\beta)\}, \tag{3.5}$$

and the local normal vector is approximated by setting it equal to the cross product of two local vectors on the differential surface *dA*. Two local vectors are formed by subtracting the values of the *x*, *y*, and *z*-locations at point (*j-1,k*) from those at point (*j,k*) and likewise for points (*j,k-1*) and (*j,k*). The cross product of the two newly-formed vectors in terms of the *x, y,* and *z* values at points (*j,k*), (*j-1,k*), and (*j,k-1*) is the numerator of local normal vector and written as

$$
\begin{aligned}
n_{v,x} &= \left(y_{j,k} - y_{j-1,k}\right)\left(z_{j,k} - z_{j,k-1}\right) - \left(y_{j,k} - y_{j,k-1}\right)\left(z_{j,k} - z_{j-1,k}\right) \\
n_{v,y} &= \left(z_{j,k} - z_{j-1,k}\right)\left(x_{j,k} - x_{j,k-1}\right) - \left(x_{j,k} - x_{j-1,k}\right)\left(z_{j,k} - z_{j,k-1}\right) \\
n_{v,z} &= \left(x_{j,k} - x_{j-1,k}\right)\left(y_{j,k} - y_{j,k-1}\right) - \left(x_{j,k} - x_{j,k-1}\right)\left(y_{j,k} - y_{j-1,k}\right).
\end{aligned} \tag{3.6}
$$

This formulation will work for points with $j \neq 1$ and $k \neq 1$ and at the base of the heat shield geometry for $k = k_{max}$ also. For points with $j = 1$, the vector formed by points (j,k) and $(j-1,k)$ is replaced by $(j+1,k)$ and (j,k), and then the numerator of the local normal vector is formed. For points with $k = 1$, which is at the tip of the nose of the vehicle, it is assumed that $n_x = -1$, and the other components are zero. The magnitude of vector n_v is then calculated to produce the normal vector

$$
\begin{aligned}
\left\|\hat{n}_v\right\| &= \sqrt{\left(n_{v,x}\right)^2 + \left(n_{v,y}\right)^2 + \left(n_{v,z}\right)^2} \\
\hat{n} &= \left\{n_x, n_y, n_z\right\} = \left\{\frac{n_{v,x}}{\left\|\hat{n}_v\right\|}, \frac{n_{v,y}}{\left\|\hat{n}_v\right\|}, \frac{n_{v,z}}{\left\|\hat{n}_v\right\|}\right\},
\end{aligned} \tag{3.7}
$$

and Eqn. (3.2) becomes

$$
C_p = C_{p,\max}\left(V_x n_x + V_y n_y + V_z n_z\right)^2. \tag{3.8}
$$

These equations calculate the pressure coefficient for a general blunt-body geometry given in the form of a three-dimensional structured mesh, with each x, y, and z surface location determined by sweep angle location j and x-section location k.

All the aerodynamic forces and moments are calculated as non-dimensional terms. The forces looked at in this analysis are the normal, axial, and side forces with coefficients C_N, C_A, and C_Y respectively. The coefficients are defined as

$$
C_N = \frac{-1}{A_p}\iint_S n_y C_p \, dA, \qquad f_{x,1} = n_{y,(j,k)} C_{p,(j,k)} dA_{(j,k)}, \tag{3.9}
$$

$$C_A = \frac{-1}{A_p}\iint_S n_x C_p dA, \qquad f_{y,1} = n_{x,(j,k)} C_{p,(j,k)} dA_{(j,k)}, \tag{3.10}$$

$$C_Y = \frac{1}{A_p}\iint_S n_z C_p dA, \qquad f_{z,1} = n_{z,(j,k)} C_{p,(j,k)} dA_{(j,k)}, \tag{3.11}$$

in which $dA_{j,k}$ is the differential surface area defined as

$$dA_{j,k} = w_{j,k} dr_{j,k} d\phi_{j,k}, \tag{3.12}$$

Using the written equations for $f_{x,1}$ that correspond to each of the force coefficients, numerical integration is completed using Simpson's rule with the process detailed in Chapter 2. Then the force coefficients become

$$\{C_N, C_A, C_Y\} = \left\{\frac{-1}{A_p} f_{x,3}, \frac{-1}{A_p} f_{y,3}, \frac{-1}{A_p} f_{z,3}\right\}. \tag{3.13}$$

The lift and drag coefficients can be determined after the normal, axial, and side force coefficients are calculated. For the Apollo CM, Hillje[6,7] divides the lift coefficient into a vertical lift coefficient $C_{L,V}$ and a horizontal lift coefficient $C_{L,H}$. This work uses the following definitions for the lift and drag coefficients

$$C_{L,V} = C_N \cos(\alpha) - C_A \sin(\alpha), \tag{3.14}$$

$$C_{L,H} = C_Y \cos(\beta) - C_A \cos(\alpha)\sin(\beta), \tag{3.15}$$

$$C_L = \sqrt{(C_{L,V})^2 + (C_{L,H})^2}, \tag{3.16}$$

$$C_D = C_N \sin(\alpha) + C_Y \sin(\beta) + C_A \cos(w_V), \tag{3.17}$$

in which w_V is the wind angle, or the magnitude of the angle from the velocity vector to the central-body axis,

$$w_V = \text{atan}\left(\frac{\sqrt{(V_y)^2 + (V_z)^2}}{V_x}\right). \tag{3.18}$$

The resulting lift-to-drag ratio equations are

$$\frac{L}{D} = \frac{C_L}{C_D}, \quad \frac{L_V}{D} = \frac{C_{L,V}}{C_D}, \quad \frac{L_H}{D} = \frac{C_{L,H}}{C_D}. \tag{3.19}$$

The aerodynamic moments about the nose that are considered in this analysis are the pitching, yawing, and rolling moments with coefficients $C_{m,0}$, $C_{n,0}$, and $C_{l,0}$. The equation for the coefficient of the pitching moment about the nose is

$$C_{m,0} = -C_N \frac{X_{cp}}{d} + C_A \frac{Y_{cp}}{d}, \tag{3.20}$$

$$\text{in which } C_{m,N,0} = -C_N \frac{X_{cp}}{d} = \frac{1}{2A_p r}\iint_S x n_y C_p \, dA, \qquad f_{x,1} = x_{j,k} n_{y,(j,k)} C_{p,(j,k)} dA_{(j,k)}, \tag{3.21}$$

$$\text{and } C_{m,A,0} = C_A \frac{Y_{cp}}{d} = \frac{1}{2A_p r}\iint_S \left(-y n_x C_p\right) dA, \qquad f_{y,1} = -y_{j,k} n_{x,(j,k)} C_{p,(j,k)} dA_{(j,k)}. \tag{3.22}$$

$C_{m,N,0}$ is the normal force's contribution to the pitching moment, and $C_{m,A,0}$ is the axial force's contribution. Similar to integrating $f_{x,1}$ to determine the force coefficients, the $f_{x,1}$ and $f_{y,1}$ of each moment coefficient can be integrated separately in order to find $f_{x,3}$

and $f_{y,3}$. Those are used to determine the location of the center of pressure after are calculated. The equation for the coefficient of the yawing moment about the nose is

$$C_{n,0} = -C_A \frac{Z_{cp}}{d} + C_Y \frac{X_{cp}}{d}, \tag{3.23}$$

$$\text{in which} \quad C_{n,A,0} = -C_A \frac{Z_{cp}}{d} = \frac{1}{2A_p r} \iint_S z n_x C_p dA, \qquad f_{x,1} = z_{j,k} n_{x,(j,k)} C_{p,(j,k)} dA_{(j,k)}, \tag{3.24}$$

$$\text{and} \quad C_{n,Y,0} = C_Y \frac{X_{cp}}{d} = \frac{1}{2A_p r} \iint_S \left(-x n_z C_p\right) dA, \qquad f_{y,1} = -x_{j,k} n_{z,(j,k)} C_{p,(j,k)} dA_{(j,k)}. \tag{3.25}$$

$C_{n,A,0}$ is the axial force's contribution to the yawing moment, and $C_{n,Y,0}$ is the side force's contribution. The equation for the coefficient of the rolling moment about the nose is

$$C_{l,0} = -C_Y \frac{Y_{cp}}{d} + C_N \frac{Z_{cp}}{d}, \tag{3.26}$$

$$\text{in which} \quad C_{l,Y,0} = -C_Y \frac{Y_{cp}}{d} = \frac{1}{2A_p r} \iint_S y n_z C_p dA, \qquad f_{x,1} = y_{j,k} n_{z,(j,k)} C_{p,(j,k)} dA_{(j,k)}, \tag{3.27}$$

$$\text{and} \quad C_{l,N,0} = C_N \frac{Z_{cp}}{d} = \frac{1}{2A_p r} \iint_S \left(-z n_y C_p\right) dA, \qquad f_{y,1} = -z_{j,k} n_{y,(j,k)} C_{p,(j,k)} dA_{(j,k)}. \tag{3.28}$$

$C_{l,Y,0}$ is the side force's contribution to the rolling moment, and $C_{l,N,0}$ is the normal force's contribution. After $f_{x,3}$ and $f_{y,3}$ are determined for each coefficient, the moment coefficients become

$$\{C_{m,0}, C_{n,0}, C_{l,0}\} = \left\{ \frac{1}{2A_p l_M}\left(f_{x,3} + f_{y,3}\right)_m, \frac{1}{2A_p l_M}\left(f_{x,3} + f_{y,3}\right)_n, \frac{1}{2A_p l_M}\left(f_{x,3} + f_{y,3}\right)_l \right\}. \quad (3.29)$$

Note that all moment coefficients are defined as the ratio of the moment to $q_\infty S l_M$, in which l_M is defined as the length of the semimajor axis. This definition of l_M makes it possible for the yawing moment coefficient $C_{n,0}$ at a given sideslip angle (the condition $\beta_1 \neq 0$, $\alpha_1 = 0$) for a prolate shape $e_1 > 0$ to be equivalent to the pitching moment coefficient $C_{m,0}$ for an oblate shape at a given angle-of-attack (the condition $\alpha_2 = \beta_1$, $\beta_2 = 0$, $e_2 = -e_1$). This definition was chosen over defining l_M as the span of the heat shield.

In validation, it is shown that the rolling moment calculations rendered a z-location of the center of pressure, Z_{cp}, that is inconsistent with the calculations of the other two moments, and so the yawing moment coefficient was used to calculate Z_{cp}. One observation is that the components of $C_{l,0}$ are of such small magnitude that the values may have numerical error on the same order, thereby producing inconsistent values for Z_{cp}. One reason for this may be that Simpson's rule has difficulty integrating numbers that have values near zero. Since the value of $C_{l,0}$ is orders of magnitude lower than the pitching and yawing moment coefficients, it is possible that Simpson's rule reached its limit around the value of $C_{l,0}$ without affecting $C_{m,0}$ and $C_{n,0}$.

3.2. *Shock-standoff Distance: Kaattari's method*

Kaattari's method for calculating the shock-standoff distance to the stagnation point is semi-empirical.[51,52] Kaattari's method assumes that the shock shape is

spherical with radius r_{sh}. There are several curves that relate the normal shock density ratio ρ_2/ρ_1 to characteristics empirically derived, including the shock-standoff distance at the sonic point for several shapes such as a cone, paraboloid, and sphere. Then there are several aerodynamic and geometric theory-based equations applied in determining the shock-standoff distance from the chosen geometry. Kaattari's method is not completely explained in this work because it is well detailed for the general blunt-body case at zero angle of attack in Ref. (52) and for a spherical-segment blunt-body at large angles of attack in Ref. (51). To introduce the method, this section does include the main equations. Then a description of how this method is implemented on the computer is included since it was originally an iterative process completed by hand. Afterwards, modifications to the method accounting for angle of attack in Ref. (51) are included to estimate the shock-standoff distance for the general blunt-body case.

3.2.1. Method Implementation

Kaattari gives two similar methods for determining the shock-standoff distance, one for conic-section bodies and the other for non-conic-section bodies. Kaattari recommends using the conic-section shock equations with ellipsoids and the non-conic-section shock equations with the spherically-blunted cone. For this work, the non-conic-section shock equations were chosen to be used for all three axial shapes because they account for edge bluntness while the conic-section equations do not. Also, for the spherical-segment blunt-bodies, it was noticed that the conic section equations and non-conic section equations produced similar results for a spherical

body. Additionally, ellipsoid relations assume a complete ellipsoid is present rather than a segment of an ellipsoid, and this may become problematic at angles of attack.

Kaattari originally calculated the shock characteristics of axisymmetric shapes by hand using plots of several geometric and aerodynamic characteristics that varied with the normal-shock density ratio. He needed to iterate his solution until the method found a converged value of the shock-standoff distance. This work uses the computer to automate Kaattari's process. Part of this is accomplished by curve-fitting the necessary semi-empirical plots. This section supplies the curve-fit equations that were generated for this work. Note that all the given digits are required in order for the curve-fits to register the corresponding norm of the residuals or R^2 values (which is given for most of the curve-fit equations). Also, even though all these digits are required to have an accurate curve-fit, this does not mean that the resulting value has a correspondingly large number of significant digits. It is suggested that the calculated results of the given curve-fits do not have more than three significant digits. As noted previously, this section does not detail the entire Kaattari method; it only includes the main modifications and additions to the method including curve-fit equations.

This section also refers to figures that are not included in this work, but the reference numbers are given. The *G* function relates the ratio of the shock-standoff distance to the shock radius, Δ_o/r_{sh}, to the blunt-body's radius of curvature at the nose

$$G = \left(1 + \frac{\Delta_o}{r_n}\right)\frac{\Delta_o}{r_{sh}} = \left(1 + \frac{\Delta_o r_{sh}}{r_n r_{sh}}\right)\frac{\Delta_o}{r_{sh}}, \tag{3.30}$$

which can be manipulated to become

$$\frac{\Delta_o}{r_{sh}} = \frac{\sqrt{1+4G\left(\frac{r_{sh}}{r_n}\right)}-1}{2\left(\frac{r_{sh}}{r_n}\right)}. \tag{3.31}$$

These relations[52] are based on a given normal-shock density ratio. Figure 1 from Ref. [52] provides a relation for the G function to the normal-shock density ratio for γ-values of 1.0 and 1.4

$$G = \begin{cases} -2.2378\left(\frac{\rho_1}{\rho_2}\right)^4 + 2.9402\left(\frac{\rho_1}{\rho_2}\right)^3 - 1.4354\left(\frac{\rho_1}{\rho_2}\right)^2 + \\ \quad + 0.81267\left(\frac{\rho_1}{\rho_2}\right) - 0.00024476, \\ \text{Norm of residuals: } 0.0033845, \qquad \gamma = 1, \\ \\ 2.4242\left(\frac{\rho_1}{\rho_2}\right)^4 - 1.4794\left(\frac{\rho_1}{\rho_2}\right)^3 - 0.047552\left(\frac{\rho_1}{\rho_2}\right)^2 \\ \quad + 0.69906\left(\frac{\rho_1}{\rho_2}\right) + 0.00062937, \qquad \gamma = 1.4. \\ \text{Norm of residuals: } 0.0025566, \end{cases} \tag{3.32}$$

If $\rho_1/\rho_2 < 0.15$, then the two curves converge and the curve-fit equation for $\gamma = 1.0$ must be used. Otherwise, interpolation between the two curves can be completed for $0.15 < \rho_1/\rho_2 < 0.45$. The shock-standoff distance at the sonic point Δ_* is non-dimensionalized by y_*, which is the normal distance from the axis of symmetry to the sonic point on the body. Figure 2 (Ref. [52]) relates the Δ_*/y_* to the ρ_1/ρ_2 for two specific heat ratio values for $0.01 < \rho_1/\rho_2 < 0.45$,

$$\frac{\Delta_*}{y_*} = \begin{cases} 6.418\left(\frac{\rho_1}{\rho_2}\right)^3 - 4.3473\left(\frac{\rho_1}{\rho_2}\right)^2 \\ \quad + 2.7174\left(\frac{\rho_1}{\rho_2}\right) + 0.0018741, \\ \text{Norm of residuals: } 0.0087586, \qquad \gamma = 1, \\ \\ 1.4064\left(\frac{\rho_1}{\rho_2}\right)^3 - 0.80536\left(\frac{\rho_1}{\rho_2}\right)^2 \\ \quad + 1.9834\left(\frac{\rho_1}{\rho_2}\right) + 0.00052448, \quad \gamma = 1.4. \\ \text{Norm of residuals: } 0.0076548, \end{cases} \tag{3.33}$$

Kaattari validates these curve-fits with experimental data for spherical, disk, and cone shapes, as well as with theoretical results for spherical and parabolic shapes for zero angle of attack. From these two equations, the shock surface inclination at a point opposite the sonic point on a flat disk θ_{*o} can be determined

$$\theta_{*o} = \text{atan}\left(\frac{G}{\Delta_* / y_*}\right). \tag{3.34}$$

The sonic angle for a sphere Φ_{*1} is defined as the body surface inclination of a sphere at the sonic point, with respect to a plane normal to the freestream direction. The variation of the sonic angle for a sphere Φ_{*1} with ρ_1/ρ_2 is given in Figure 4 from Ref. [52] for $0.025 < \rho_1/\rho_2 < 0.45$,

$$\Phi_{*1}(\text{deg}) = \begin{cases} -797.1\left(\frac{\rho_1}{\rho_2}\right)^4 + 908.77\left(\frac{\rho_1}{\rho_2}\right)^3 - 380.2\left(\frac{\rho_1}{\rho_2}\right)^2 \\ \quad + 80.348\left(\frac{\rho_1}{\rho_2}\right) + 33.383, & \gamma = 1, \\ 104.8\left(\frac{\rho_1}{\rho_2}\right)^4 - 7.2046\left(\frac{\rho_1}{\rho_2}\right)^3 - 99.371\left(\frac{\rho_1}{\rho_2}\right)^2 \\ \quad + 61.984\left(\frac{\rho_1}{\rho_2}\right) + 32.589, & \gamma = 1.4. \end{cases} \tag{3.35}$$

If $\rho_1/\rho_2 < 0.15$, then the curve-fit equation for $\gamma = 1.0$ must be used. Otherwise, interpolation between the two curves can be completed for $0.15 < \rho_1/\rho_2 < 0.45$. The sonic angle for a rounded-corner blunt-body Φ_* varies with r_c/r

$$\frac{\sin(\Phi_*)}{\sin(\Phi_{*1})} = \begin{cases} 20\frac{r_c}{r}, & 0.00 < \frac{r_c}{r} \le 0.01, \\ -18.35253948\left(\frac{r_c}{r}\right)^2 + 5.31156637\left(\frac{r_c}{r}\right) \\ \quad + 0.15140845, & 0.01 < \frac{r_c}{r} \le 0.10, \\ 0.2159\ln\left(\frac{r_c}{r}\right) + 1.01, & 0.10 < \frac{r_c}{r} \le 1.00. \end{cases} \tag{3.36}$$

For each axial shape, ε, which is the inclination on the forward body surface at the point tangent with the corner radius, is given by the following set of equations. From these, the sonic angle Φ_* can be determined. For the spherical-segment and power law axial shapes,

$$\varepsilon = \begin{cases} \operatorname{asin}\left(\dfrac{\dfrac{r}{r_n}\left(1 - \dfrac{r_c}{r}\right)}{1 - \dfrac{r_c}{r_n}} \right), & \text{Spherical - segment,} \\ \dfrac{\pi}{2} - \left| \operatorname{atan}\left(\dfrac{y_{1,k\,\max} - y_{1,k\,\max-1}}{x_{1,k\_\max} - x_{1,k\_\max-1}} \right) \right|, & \text{Power law.} \end{cases} \tag{3.37}$$

For the power law axial shape, the term subtracted from $\pi/2$ can be defined as an effective local half-cone angle. There are two cases for the spherically-blunted cone: one in which the spherical-segment is the dominant shape, in which the r_n/d is large, and the other in which the cone shape dominates. This is described by the following equation set for the spherically-blunted cone

$$\varepsilon = \begin{cases} \dfrac{\pi}{2} - \theta_c, & 0 < \dfrac{r_n}{d} \le \dfrac{1}{2}\sin\left(\dfrac{\pi}{2} - \theta_c\right), \\ \dfrac{\pi}{2} - \left| \operatorname{atan}\left(\dfrac{y_{1,\mathrm{kmax}} - y_{1,\mathrm{kmax-1}}}{x_{1,\mathrm{k\_max}} - x_{1,\mathrm{k\_max-1}}} \right) \right|, & \dfrac{1}{2}\sin\left(\dfrac{\pi}{2} - \theta_c\right) < \dfrac{r_n}{d}. \end{cases} \tag{3.38}$$

Note that if $\varepsilon > 37^o$, then ε is set equal to 37^o since that is the limit of Kaattari's dataset. The spherically-blunted cone does not approach this limit since it would require a half-cone angle $\theta_c < 53^o$, and the limit for the half-cone angle in the optimizer is set at 55^o. Kaattari's method also notes that if the sonic angle $\Phi_* < \varepsilon$, then the sonic point is assumed to be taken at the tangency angle ε, and so Φ_* is set equal to ε for this case. To determine θ_*, Kaattari supplies Figure 6(b) from Ref. [52] that relates the difference $\theta_* - \theta_{*_o}$ as a function of Φ_*. This relation varies with the normal-shock density ratio, and their corresponding curve-fit equations with Φ_* limits are included

$$\frac{\theta_* - \theta_{*o}}{(\text{deg})} = \begin{cases} -7.8164\times10^{-9}\Phi_*^6 + 1.1554\times10^{-6}\Phi_*^5 \\ \quad -6.5557\times10^{-5}\Phi_*^4 + 0.0017384\Phi_*^3 \\ \quad -0.01669\Phi_*^2 - 0.036272\Phi_* + 0.026591, & \frac{\rho_2}{\rho_1} = 3, \quad 1 < \Phi_* \le 40 \\ \quad \text{Norm of residuals: } 0.10637, \\ \\ -1.3002\times10^{-8}\Phi_*^6 + 1.7632\times10^{-6}\Phi_*^5 \\ \quad -9.1189\times10^{-5}\Phi_*^4 + 0.0021927\Phi_*^3 \\ \quad -0.01933\Phi_*^2 + 0.01135\Phi_* + 0.0031709, & \frac{\rho_2}{\rho_1} = 4, \quad 1 < \Phi_* \le 40 \\ \quad \text{Norm of residuals: } 0.04381, \\ \\ -6.2549\times10^{-9}\Phi_*^6 + 8.0483\times10^{-7}\Phi_*^5 \\ \quad -3.7688\times10^{-5}\Phi_*^4 + 0.00087115\Phi_*^3 \\ \quad -0.0054599\Phi_*^2 + 0.019362\Phi_* - 0.0085934, & \frac{\rho_2}{\rho_1} = 6, \quad 4 < \Phi_* \le 40 \\ \quad \text{Norm of residuals: } 0.0793, \\ \\ -6.0809\times10^{-9}\Phi_*^6 + 6.9855\times10^{-7}\Phi_*^5 \\ \quad -2.7801\times10^{-5}\Phi_*^4 + 0.00053225\Phi_*^3 \\ \quad +\ 0.00034058\Phi_*^2 - 0.0016152\Phi_* + 0.0038209, & \frac{\rho_2}{\rho_1} = 8, \quad 4 < \Phi_* \le 40 \\ \quad \text{Norm of residuals: } 0.0583, \\ \\ -9.8112\times10^{-11}\Phi_*^8 + 1.4038\times10^{-8}\Phi_*^7 \\ \quad -8.0148\times10^{-7}\Phi_*^6 + 2.3289\times10^{-5}\Phi_*^5 \\ \quad -0.00035965\Phi_*^4 + 0.0028275\Phi_*^3 \\ \quad -0.0034554\Phi_*^2 + 0.0075298\Phi_* - 0.00075942, & \frac{\rho_2}{\rho_1} = 12, \quad 0 < \Phi_* \le 40 \\ \quad \text{Norm of residuals: } 0.067392, \\ \\ \quad 1.5644\times10^{-7}\Phi_*^6 - 3.0006\times10^{-5}\Phi_*^5 \\ \quad\quad +\ 0.0023397\Phi_*^4 - 0.094787\Phi_*^3 \\ \quad\quad +\ 2.1177\Phi_*^2 - 24.509\Phi_* + 115.89, & \frac{\rho_2}{\rho_1} = 16, \quad 17.5 < \Phi_* \le 40 \\ \quad\quad \text{Norm of residuals: } 0.0795, \\ \\ \quad 1.2753\times10^{-8}\Phi_*^6 - 1.4433\times10^{-6}\Phi_*^5 \\ \quad\quad +\ 6.7379\times10^{-5}\Phi_*^4 - 0.0014138\Phi_*^3 \\ \quad\quad +\ 0.020612\Phi_*^2 - 0.040357\Phi_* + 0.012458, & \frac{\rho_2}{\rho_1} = 20, \quad 1 < \Phi_* \le 40. \\ \quad\quad \text{Norm of residuals: } 0.11582, \end{cases} \tag{3.39}$$

For all equations in this set except $\rho_2/\rho_1 = 12$, for $0 < \Phi_* < 1$ it is assumed that the difference $\theta_* - \theta_{*o}$ is zero. For this region, the equation for $\rho_2/\rho_1 = 12$ is applied for normal-shock density ratios of twelve and greater. The equation for $\rho_2/\rho_1 = 16$ is not

applied until $\Phi_* > 17.5$, and if it is used before this, the results could be erroneous since the curve fit was designed only for the noted ranges. Linear interpolation between two of the curves within this range of ρ_2/ρ_1 can be exercised to approximate the values of the difference for normal-shock density ratios that are not listed.

The main non-conic-section body shock equation relates the shock radius r_{sh} to the stagnation shock-standoff distance, the corner radius, sonic shock-standoff distance and the tangency angle

$$\frac{r_{sh}}{y_*}\left(\frac{\Delta_o}{r_{sh}}\right) = \frac{x_s}{y_*} + \left[\frac{\Delta_*}{y_*} - \frac{\tan(\varepsilon) + \frac{r_n}{r}\left(\frac{\cos(\varepsilon)-1}{\cos(\varepsilon)}\right) + \frac{r_c}{r}\left(\frac{1-\sin(\varepsilon)}{\cos(\varepsilon)} - \cos(\Phi_*)\right)}{1 - \frac{r_c}{r}(1-\sin(\Phi_*))}\right], \quad (3.40)$$

in which x_s is the streamwise distance from the apex of the shock to the point on the shock at distance y_* from the central axis. This relation along with the shock solution nomograph equation,

$$B_s \frac{x_s}{y_*} = \left(\frac{r_{sh}}{y_*} - \frac{1}{\tan(\theta_*)}\right), \quad (3.41)$$

and the initial value of Δ_o/r_{sh} set equal to G, determine the values of B_s, y_*/r, r_{sh}/r, and Δ_o/r,

$$B_s = \left(\frac{r_{sh}}{y_*}\right)^2 - \frac{1}{\tan^2(\theta_*)}, \quad (3.42)$$

$$\frac{y_*}{r} = 1 - \frac{r_c}{r}(1-\sin(\Phi_*)), \quad (3.43)$$

$$\frac{r_{sh}}{r} = \frac{r_{sh}}{y_*}\frac{y_*}{r}, \quad (3.44)$$

$$\frac{r_{sh}}{r_n} = \frac{r_{sh}}{y_*}\frac{y_*}{r}\frac{r}{r_n}, \tag{3.45}$$

$$\frac{\Delta_o}{r} = \frac{\Delta_o}{r_{sh}}\frac{r_{sh}}{r}. \tag{3.46}$$

From here, the value of Δ_o/r_{sh} based on Eqn. (3.31) is calculated and the process is repeated. Once the value of Δ_o/r_{sh} converges within 0.001, the iterative process has been completed, and the shock properties of the blunt-body have been determined for zero angle of attack. The main output variable is Δ_o/r_n. The complete process with referenced figures and examples is included in Ref. (52).

3.2.2. Accounting for Nonaxisymmetric Shapes & Angle of Attack

Kaattari[51] offers a way to account for angle of attack for spherical-segment axisymmetric blunt bodies. In this section, a basic method is described for determining how Δ_o/r_n changes both for a nonaxisymmetric blunt body and with angle of attack based on Kaattari's method. It also has been modified to account for the spherically-blunted cone and power law axial shapes. These modifications are meant to produce results that follow expected trends only. Although there is confidence in the expected trends, the results should not be accepted as unequivocal since several of the more exotic shapes have not been studied before from a re-entry heat transfer standpoint. The expectation is that these modifications produce shock-standoff distances for nonaxisymmetric geometries within the proper order of magnitude. The reason for using this method is to approximate the stagnation-point radiative heat flux, and Chapter 4 explains how it can be approximated for a blunt body using the shock-standoff distance.

For an axisymmetric spherical-segment geometry, Kaattari provides the process for estimating the shock-standoff distance in Ref. (51), and the equation

$$\frac{\Delta_\alpha}{d} = \frac{\Delta_o}{d} - \left(c_1 \frac{r_{st}}{r_{\max}} + c_3 \left(\frac{r_{st}}{r_{\max}} \right)^3 \right) \cos(\phi) \sin(\alpha) \tag{3.47}$$

relates the shock-standoff distance at angle of attack to that at zero angle of attack. Note that for this work, the angle of the azimuth ϕ is assumed equal to zero. To determine how the value of Δ_o/r_n varies with angle of attack, semi-empirical data of shock correlation functions from Kaattari in Ref. (51) have been curve-fit. Applying these curve-fits is described in the next section, including the modifications required to use Kaattari's method to approximate how the shock-standoff distance changes with angle of attack. Figure 9(a) from Ref. [51] shows how the shock correlation coefficient c_1 varies with the normal-shock density ratio and the tangency angle ε and is curve-fitted (input ε in degrees) with indicated limits of applicability

$$c_1 = \begin{cases} -1.93013729 \times 10^{-7} \varepsilon^3 + 1.16661976 \times 10^{-5} \varepsilon^2 \\ \quad - 7.64482284 \times 10^{-4} \varepsilon + 0.214380383 & \frac{\rho_2}{\rho_1} = 3, \quad 0 < \varepsilon \le 45^o, \\ \quad R^2 = 0.9987, \\ \\ 9.63317384 \times 10^{-7} \varepsilon^3 - 8.78810663 \times 10^{-5} \varepsilon^2 \\ \quad - 7.60025063 \times 10^{-4} \varepsilon + 0.221403281 & \frac{\rho_2}{\rho_1} = 4, \quad 0 < \varepsilon \le 45^o, \\ \quad R^2 = 0.9998, \\ \\ -4.12212802 \times 10^{-11} \varepsilon^6 + 5.39975415 \times 10^{-9} \varepsilon^5 \\ \quad - 2.31598093 \times 10^{-7} \varepsilon^4 + 4.78956150 \times 10^{-6} \varepsilon^3 \\ \quad - 1.15717926 \times 10^{-4} \varepsilon^2 - 2.21715933 \times 10^{-3} \varepsilon & \frac{\rho_2}{\rho_1} = 5, \quad 0 < \varepsilon \le 45^o, \\ \quad + 0.230264502 \\ \quad R^2 = 0.9999, \end{cases} \tag{3.48}$$

$$
c_1 = \begin{cases}
-2.92464389\times10^{-10}\varepsilon^5 - 2.69993388\times10^{-9}\varepsilon^4 \\
\quad + 4.08148122\times10^{-6}\varepsilon^3 - 2.09241117\times10^{-4}\varepsilon^2 \\
\quad - 2.50199798\times10^{-3}\varepsilon + 0.232732751 & \dfrac{\rho_2}{\rho_1} = 6, \quad 0 < \varepsilon \le 42.5^o, \\
\qquad R^2 = 0.9999, & \\
-9.07434828\times10^{-10}\varepsilon^5 + 6.32411067\times10^{-8}\varepsilon^4 \\
\quad + 2.18083922\times10^{-6}\varepsilon^3 - 1.56690529\times10^{-4}\varepsilon^2 \\
\quad - 4.54631057\times10^{-3}\varepsilon + 0.231841134 & \dfrac{\rho_2}{\rho_1} = 8, \quad 0 < \varepsilon \le 42.5^o, \\
\qquad R^2 = 0.9999, & \\
2.00439718\times10^{-10}\varepsilon^6 - 2.99995789\times10^{-8}\varepsilon^5 \\
\quad + 1.62858238\times10^{-6}\varepsilon^4 - 3.65809838\times10^{-5}\varepsilon^3 \\
\quad + 3.31432550\times10^{-4}\varepsilon^2 - 8.40015875\times10^{-3}\varepsilon \\
\quad + 0.232406493 & \dfrac{\rho_2}{\rho_1} = 10, \quad 0 < \varepsilon \le 40^o, \\
\qquad R^2 = 0.9999, & \\
2.56915093\times10^{-10}\varepsilon^6 - 3.32278424\times10^{-8}\varepsilon^5 \\
\quad + 1.52078813\times10^{-6}\varepsilon^4 - 2.69805855\times10^{-5}\varepsilon^3 \\
\quad + 2.01204775\times10^{-4}\varepsilon^2 - 9.22392526\times10^{-3}\varepsilon \\
\quad + 0.232157648 & \dfrac{\rho_2}{\rho_1} = 12, \quad 0 < \varepsilon \le 40^o, \\
\qquad R^2 = 0.9998, & \\
4.06700008\times10^{-9}\varepsilon^5 - 5.34031912\times10^{-7}\varepsilon^4 \\
\quad + 2.54224815\times10^{-5}\varepsilon^3 - 3.58846154\times10^{-4}\varepsilon^2 \\
\quad - 8.09283123\times10^{-3}\varepsilon + 0.221551084 & \dfrac{\rho_2}{\rho_1} = 16, \quad 0 < \varepsilon \le 40^o, \\
\qquad R^2 = 0.9997, & \\
6.06112566\times10^{-9}\varepsilon^5 - 7.49638803\times10^{-7}\varepsilon^4 \\
\quad + 3.16638882\times10^{-5}\varepsilon^3 - 3.50334207\times10^{-4}\varepsilon^2 \\
\quad - 9.44613956\times10^{-3}\varepsilon + 0.210113003 & \dfrac{\rho_2}{\rho_1} = 20, \quad 0 < \varepsilon \le 40^o, \\
\qquad R^2 = 0.9991, & \\
4.60808129\times10^{-9}\varepsilon^5 - 6.46122093\times10^{-7}\varepsilon^4 \\
\quad + 2.95290942\times10^{-5}\varepsilon^3 - 3.29553862\times10^{-4}\varepsilon^2 \\
\quad - 9.52531793\times10^{-3}\varepsilon + 0.200148091 & \dfrac{\rho_2}{\rho_1} = 22, \quad 0 < \varepsilon \le 40^o. \\
\qquad R^2 = 0.9990, &
\end{cases} \tag{3.49}
$$

Note that all the digits have to be included in order to maintain accuracy. If digits are removed, it is strongly recommended that the modified curve-fit be plotted to verify that the curve-fit is still valid throughout the entire range and to verify none of the curve-fits intersect each other. Interpolation for cases with normal-shock density ratios in-between the given curve fits has been tested and is completely feasible. The correlation constant c_3 is also supplied in Figure 9(b) from Ref. [51], and the curve-fit equations (input ε in degrees) have been generated in this work

$$c_3\left(\frac{r_n \sin(\varepsilon)}{d}\right)^2 = \begin{cases} -3.39744191\times10^{-8}\varepsilon^3 + 3.89964215\times10^{-6}\varepsilon^2 \\ \quad -1.82847314\times10^{-4}\varepsilon + 0.0231888243 & \frac{\rho_2}{\rho_1}=3,\quad 0<\varepsilon\le 45^o, \\ \quad R^2 = 0.9994, & \\ \\ -1.48406667\times10^{-8}\varepsilon^3 + 1.72390334\times10^{-6}\varepsilon^2 \\ \quad -1.35288319\times10^{-4}\varepsilon + 0.0201117430 & \frac{\rho_2}{\rho_1}=4,\quad 0<\varepsilon\le 45^o, \\ \quad R^2 = 0.9995, & \\ \\ -7.15150540\times10^{-12}\varepsilon^6 + 9.54110294\times10^{-10}\varepsilon^5 \\ \quad -4.49628934\times10^{-8}\varepsilon^4 + 8.56040487\times10^{-7}\varepsilon^3 \\ \quad -4.96819914\times10^{-6}\varepsilon^2 - 1.14702612\times10^{-4}\varepsilon & \frac{\rho_2}{\rho_1}=5,\quad 0<\varepsilon\le 45^o, \\ \quad +1.77036651\times10^{-2} & \\ \quad R^2 = 0.9998, & \\ \\ -1.13917530\times10^{-10}\varepsilon^5 + 1.63488703\times10^{-8}\varepsilon^4 \\ \quad -7.24637110\times10^{-7}\varepsilon^3 + 9.92739734\times10^{-6}\varepsilon^2 \\ \quad -1.27550983\times10^{-4}\varepsilon + 0.0159334044 & \frac{\rho_2}{\rho_1}=6,\quad 0<\varepsilon\le 45^o, \\ \quad R^2 = 0.9995, & \\ \\ -3.80921614\times10^{-10}\varepsilon^5 + 4.33744906\times10^{-8}\varepsilon^4 \\ \quad -1.56325253\times10^{-6}\varepsilon^3 + 1.66417857\times10^{-5}\varepsilon^2 \\ \quad -1.21889535\times10^{-4}\varepsilon + 0.0149288590 & \frac{\rho_2}{\rho_1}=7,\quad 0<\varepsilon\le 45^o, \\ \quad R^2 = 0.9995, & \\ \\ -5.69532428\times10^{-10}\varepsilon^5 + 6.22306898\times10^{-8}\varepsilon^4 \\ \quad -2.15386203\times10^{-6}\varepsilon^3 + 2.21510280\times10^{-5}\varepsilon^2 \\ \quad -1.32633841\times10^{-4}\varepsilon + 0.0141488648 & \frac{\rho_2}{\rho_1}=8,\quad 0<\varepsilon\le 40^o, \\ \quad R^2 = 0.9994, & \end{cases} \tag{3.50}$$

$$c_3\left(\frac{r_n \sin(\varepsilon)}{d}\right)^2 = \begin{cases} -7.04675716\times10^{-10}\varepsilon^5 + 7.25696594\times10^{-8}\varepsilon^4 \\ \quad -2.32498214\times10^{-6}\varepsilon^3 + 2.06298722\times10^{-5}\varepsilon^2 \\ \quad -1.27943518\times10^{-4}\varepsilon + 0.0131448916 & \frac{\rho_2}{\rho_1} = 10, \quad 0 < \varepsilon \le 40^o, \\ \qquad R^2 = 0.9995, \\ -7.03151544\times10^{-10}\varepsilon^5 + 6.54759070\times10^{-8}\varepsilon^4 \\ \quad -1.73419068\times10^{-6}\varepsilon^3 + 5.67714535\times10^{-6}\varepsilon^2 \\ \quad -4.76005398\times10^{-5}\varepsilon + 0.0119228070 & \frac{\rho_2}{\rho_1} = 14, \quad 0 < \varepsilon \le 40^o, \\ \qquad R^2 = 0.9993, \\ -6.61739779\times10^{-10}\varepsilon^5 + 6.12012384\times10^{-8}\varepsilon^4 \\ \quad -1.56703453\times10^{-6}\varepsilon^3 + 2.90105343\times10^{-6}\varepsilon^2 \\ \quad -4.37257752\times10^{-5}\varepsilon + 0.0116297874 & \frac{\rho_2}{\rho_1} = 16, \quad 0 < \varepsilon \le 40^o, \\ \qquad R^2 = 0.9996, \\ -6.61739779\times10^{-10}\varepsilon^5 + 6.12012384\times10^{-8}\varepsilon^4 \\ \quad -1.56703453\times10^{-6}\varepsilon^3 + 2.90105343\times10^{-6}\varepsilon^2 \\ \quad -4.37257752\times10^{-5}\varepsilon + 0.0113797874 & \frac{\rho_2}{\rho_1} = 18, \quad 0 < \varepsilon \le 40^o, \\ \qquad R^2 = 0.9996 \\ -6.61739779\times10^{-10}\varepsilon^5 + 6.12012384\times10^{-8}\varepsilon^4 \\ \quad -1.56703453\times10^{-6}\varepsilon^3 + 2.90105343\times10^{-6}\varepsilon^2 \\ \quad -4.37257752\times10^{-5}\varepsilon + 0.0111547874 & \frac{\rho_2}{\rho_1} = 20, \quad 0 < \varepsilon \le 40^o, \\ \qquad R^2 = 0.9996 \\ -6.61739779\times10^{-10}\varepsilon^5 + 6.12012384\times10^{-8}\varepsilon^4 \\ \quad -1.56703453\times10^{-6}\varepsilon^3 + 2.90105343\times10^{-6}\varepsilon^2 \\ \quad -4.37257752\times10^{-5}\varepsilon + 0.0109422874 & \frac{\rho_2}{\rho_1} = 22, \quad 0 < \varepsilon \le 40^o. \\ \qquad R^2 = 0.9996, \end{cases} \tag{3.51}$$

Because density ratios over sixteen may occur in the regions of maximum heat transfer during planetary entry, it was decided to extrapolate the curve-fit for $\rho_2/\rho_1 >$ 16 listed in Eqns. (3.49) and (3.51). With all of these equations, it is possible to approximate the shock-standoff distance. This is the full extent of Kaattari's method.

To account for nonaxisymmetric geometries, it is assumed that the change in the shock-standoff distance for shape variance and an angle of attack is dependent on

eccentricity and the axial shape of the upper half at $\phi = 0^o$ (j = 1) and the lower half at $\phi = 180^o$ (j = ($jmax$-1)/2). An example geometry is shown in Figure 3.2 to show how Kaattari's method is applied.

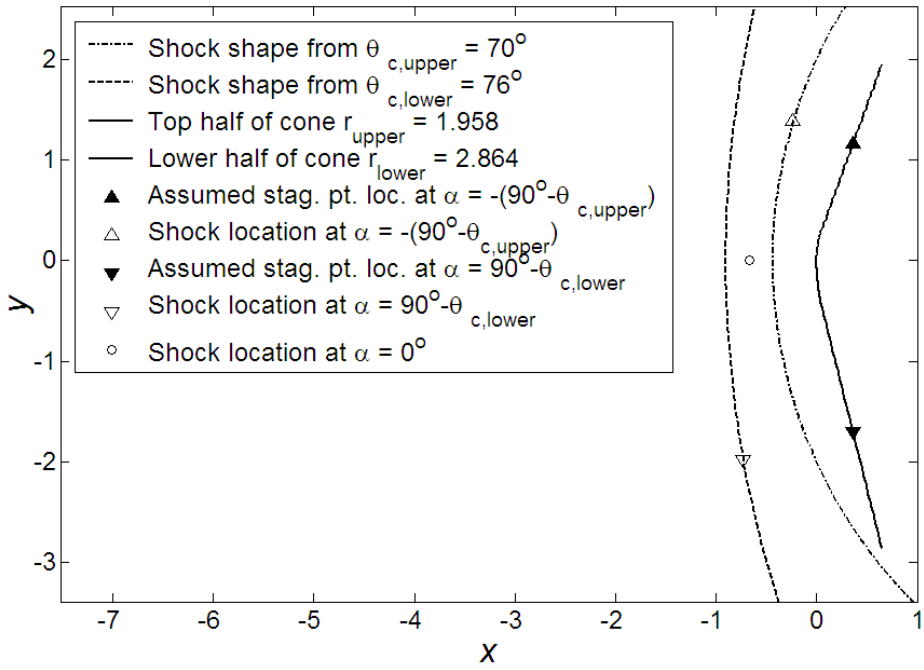

Figure 3.2. Spherically-blunted cone profile shock-standoff distance variance.

Kaattari's method is applied to determine the radii of the shock for the upper profile $r_{sh,upper}$ = 4.827 and the lower profile $r_{sh,lower}$ = 11.30 separately. This is accomplished by accounting for the different half-cone angles for the upper and lower surfaces, $\theta_{c,upper}$ = 70° and $\theta_{c,lower}$ = 76° respectively. Also the different upper and lower base radii, r_{upper} = 1.958 m, and r_{lower} = 2.864 m respectively are accounted for and added together to produce the base diameter. The shock-standoff distances for each case is calculated $\Delta_{o,upper}$ = 0.4175 m and $\Delta_{o,lower}$ = 0.9215 m. After the shock-standoff distances are determined this work assumes that this cone shape must have a zero angle of attack shock-standoff distance Δ_o that is in-between the two calculated shock-standoff values. It is assumed that each has equal effect on Δ_o, and so it is set

equal to the average of the two and produces the open circle in Figure 3.2 corresponding to $\Delta_o = 0.6695$ m.

Originally, to account for angle of attack, Kaattari's Eqn. (3.47) was applied, but for the case of Figure 3.2, $\Delta_{\alpha<0} > \Delta_{\alpha>0}$, which does not follow the most probable trend. At $\alpha<0$, the upper profile faced the freestream more than the lower profile, and so it should have more effect on Δ_α than the lower profile. Because $r_{sh,lower} > r_{sh,upper}$, it is expected that $\Delta_{\alpha=-(90-\theta)} < \Delta_{\alpha=90-\theta}$, which is the opposite of the trend produced by Eqn. (3.47). As a result, the following basic method is applied to guarantee that this trend is held.

This work assumes that the shock-standoff distance at $\alpha = 90^o - \theta_{c,lower}$, which is $\alpha>0^o$, can be approximated by the distance from the lower shock with radius $r_{sh,lower}$ that is perpendicular to the lower face. This distance is the length between the two inverted triangles shown in Figure 3.2. For $\alpha<0$, the shock-standoff distance at $\alpha = -(90^o - \theta_{c,upper})$, can be approximate by the distance from the upper shock with $r_{sh,upper}$ that is perpendicular to the upper face. This distance is the length between the two triangles shown in Figure 3.2. As a result, this also means that if $r_{sh,lower} < r_{sh,upper}$, then $\Delta_{\alpha=-(90-\theta)} > \Delta_{\alpha=90-\theta}$, thus this method accounts for either case. Linear interpolation between Δ_o and Δ_α is applied once the endpoints $\Delta_{\alpha=-(90-\theta,upper)}$ and $\Delta_{\alpha=90-\theta,lower}$ are determined. This simple method is implemented only so that the shock-standoff distance is varied and follows an expected trend.

To account for eccentricity, the average base radius is determined; then it is divided by the maximum base radius to produce the non-dimensional average base radius $r_{avg,nd}$. This term is then used to calculate the upper and lower shock radii

$$r_{sh,upper} = \begin{cases} \dfrac{r_{sh,upper}}{r_n}\dfrac{r_n}{r_{upper}} r_{upper} r_{avg,nd}, & e \geq 0, \\ \dfrac{r_{sh,upper}}{r_n}\dfrac{r_n}{r_{upper}}\dfrac{r_{upper}}{r_{avg,nd}}, & e < 0, \end{cases} \tag{3.52}$$

$$\text{and } r_{sh,lower} = \begin{cases} \dfrac{r_{sh,lower}}{r_n}\dfrac{r_n}{r_{lower}} r_{lower} r_{avg,nd}. & e \geq 0, \\ \dfrac{r_{sh,lower}}{r_n}\dfrac{r_n}{r_{lower}}\dfrac{r_{lower}}{r_{avg,nd}}, & e < 0. \end{cases} \tag{3.53}$$

Eccentricity is accounted for through this approach so that the calculated shock radii of a prolate shape with eccentricity *e* at α and those of an oblate shape with the same eccentricity are affected equally. This is one way of producing consistency throughout the results. Note that this addition does not provide true consistency when calculating the radiative heat transfer, as the value of q_{rad} varies up to 33% at eccentricity |*e*| > +/- 0.9 and up to 20% at |*e*| > +/- 0.8. As a result, any calculations for highly eccentric shapes should be seen only as approximate solutions.

For rounded-edge concave shapes such as that shown in Figure 2.7, the profile could look similar to an inverted Figure 3.2. In this case, it is assumed that only the surface with the larger *r* (in the case of Figure 2.7 it would be r_{upper}) is applied rather than using the average of shock-standoff distances because the surface with the larger *r* represents the primary radius of the shock-shape. This is assumed for the rounded-edge concave shapes since they have not been investigated experimentally or through computational fluid dynamics (CFD). It should be noted that the shock shape about rounded-edge concave shapes may have a radius that varies with sweep angle, and so only basic assumptions can be made at the level of this work's analysis.

3.3. Static Stability

The stability of a planetary entry vehicle is one of the main factors that determines whether a particular design is feasible. If the PEV requires quasi-steady flow in order for it to follow the designed trajectory, then the vehicle must be able to remain or return to the designed trim angle of attack α_{trim} after encountering flow disturbances. This can be determined by looking at the static and dynamic stability of the vehicle. This work analyzes the heat shields' static stability only for a first-look analysis. An in-depth, full vehicle analysis would require the study of both the static and dynamic stability since it is possible for a statically stable vehicle to be dynamically unstable. If a vehicle is statically stable, then it possesses the aerodynamic moments required to restore the vehicle to an equilibrium state after encountering a flow disturbance.[67]

One way to measure a vehicle's static stability is to analyze its aerodynamic moments about the vehicle's center of gravity. In this work, the aerodynamic moment coefficients $C_{m,0}$, $C_{n,0}$, and $C_{l,0}$ about the nose of the vehicle and the force coefficients C_N, C_A, and C_Y are calculated using modified Newtonian Impact Theory. Then the center of pressure location is determined from this information as previously explained. The center of pressure is the location at which the aerodynamic forces are applied. As a result, the aerodynamic moments, which are produced by the aerodynamic forces, are zero about the center of pressure. Once a center of gravity location is either chosen or calculated, moments produced by the aerodynamic forces about the center of gravity are calculated.

For a fixed body-axis moment with conventions for positive moments given in Figure 3.1(b), there are twelve possible center of pressure locations, with respect to the vehicle's center of gravity and the central axis. For example, in longitudinal stability, the contributions of the normal and axial forces to the pitching moment about the center of gravity are determined. If the center of gravity is below the central axis, then the center of pressure can be below the center of gravity, above the center of gravity in the same quadrant (below the central axis), or above the center of gravity in a different quadrant (above the central axis). In each of these cases, the center of pressure could be in front of, aligned with, or behind the center of gravity. If the aligned case is grouped with either the in front or behind cases, then there are six different geometric cases. The other six cases correspond to the inverted case in which the center of gravity is above the central axis, thereby producing a total of twelve cases.

After deriving each of the twelve cases for the pitching, yawing, and rolling moments about the center of gravity, it was observed that all twelve cases for each moment could be reduced into one equation, producing the following three equations

$$C_{m,cg} = C_N\left(\frac{X_{cg} - X_{cp}}{d}\right) + C_A\left(\frac{Y_{cp} - Y_{cg}}{d}\right), \tag{3.54}$$

$$C_{n,cg} = C_Y\left(\frac{X_{cp} - X_{cg}}{d}\right) + C_A\left(\frac{Z_{cg} - Z_{cp}}{d}\right), \tag{3.55}$$

$$C_{l,cg} = \begin{cases} C_N\left(\frac{Z_{cp} - Z_{cg}}{d}\right) + C_Y\left(\frac{Y_{cg} - Y_{cp}}{d}\right), & C_{L,V} \geq 0, \\ -\left(C_N\left(\frac{Z_{cp} - Z_{cg}}{d}\right) + C_Y\left(\frac{Y_{cg} - Y_{cp}}{d}\right)\right), & C_{L,V} < 0. \end{cases} \tag{3.56}$$

In order for the definition of rolling moment static stability to remain constant, the rolling moment $C_{l,cg}$ equation accounts for the change in positive moment convention that occurs when the vertical component of the lift coefficient becomes negative. The explanation for this is included in the next section, which comments on two misinterpretations of basic aerodynamic and stability theory.

With the moments about the vehicle's center of gravity determined, its static stability can be determined through an analysis of its moment derivatives with respect to angle of attack and sideslip angle. These derivatives $C_{m,cg\alpha}$, $C_{n,cg\beta}$, and $C_{l,cg\beta}$ are known as the static stability derivatives. For longitudinal stability, the derivative of the pitching moment with respect to angle of attack must be negative. For yaw stability, the derivative of the yawing moment with respect to sideslip angle must be positive. For roll stability, the derivative of the rolling moment with respect to sideslip angle must be negative. If the positive moment convention for $C_{l,cg}$ were kept constant for positive and negative lift, then roll stability requires the rolling moment derivative to be positive for negative lift.

To calculate the stability derivatives numerically, the code determines the $C_{m,cg}$, $C_{n,cg}$, and $C_{l,cg}$ at α - 0.25°, α + 0.25°, β - 0.5°, β + 0.5° in order to use the following finite-differencing approximate of the first derivative

$$C_{m,cg,\alpha} = \frac{dC_{m,cg}}{d\alpha} = \frac{C_{m,cg,\alpha+0.25^o} - C_{m,cg,\alpha-0.25^o}}{\Delta\alpha}, \tag{3.57}$$

$$C_{n,cg,\beta} = \frac{dC_{n,cg}}{d\beta} = \frac{C_{n,cg,\beta+0.5^o} - C_{n,cg,\beta-0.5^o}}{\Delta\beta}, \tag{3.58}$$

$$C_{l,cg,\beta} = \frac{dC_{l,cg}}{d\beta} = \frac{C_{l,cg,\beta+0.5^o} - C_{l,cg,\beta-0.5^o}}{\Delta\beta}. \tag{3.59}$$

These numerical approximations are second-order accurate in space. With the static stability derivatives calculated, an analysis of the vehicle's static stability can be completed.

3.4. Correcting Misinterpretations

Two common misconceptions are detailed in this section to emphasize the importance of understanding these basic aerodynamic concepts. The first concerns the static roll stability requirement on a given aerodynamic vehicle. The second involves calculating the location of the center of pressure on a passive aerodynamic vehicle.

3.4.1. Static Roll Stability Requirement

When either a disturbance in the flow or a control input generates a rolling moment about the center of gravity of a lift-generating vehicle, the direction of the lift vector relative to the horizon is no longer perpendicular, causing the vehicle to sideslip. In general, a lift-generating vehicle sideslips as it rolls, and general stability theory concludes that there is a coupled effect that can be related to the vehicle's roll angle and the freestream sideslip angle. To make a lift-generating vehicle statically stable when it encounters a flow disturbance that brings the vehicle away from its desired orientation and path, the vehicle must be able to produce a counter-moment to bring it to its initial orientation (usually zero-roll angle or the designed trim position).

Aircraft stability assumes that the lift vector is always positive for an aircraft in wings-level attitude; this leads to the standard convention that a positive rolling moment renders a positive change in sideslip. As a result, the rolling stability

derivative $C_{l,\beta}$ is required to be negative for static stability to counter flow disturbances.[67]

Spacecraft stability must also account for the possibility that the vehicle may be designed to produce negative lift during a portion of its trajectory. If the lift vector is negative, then a positive rolling moment renders a negative change in sideslip, producing the reverse relationship between roll angle and sideslip angle, in which a positive roll angle produces a negative sideslip angle. In this case, the rolling stability derivative $C_{l,\beta}$ is required to be positive for static roll stability. Since a negative $C_{l,\beta}$ is commonly associated with a statically roll stable vehicle, this convention is maintained in this work by reversing the direction of the positive rolling moment convention when the vehicle produces negative lift as shown in Figure 3.1(b). The sign reversal of the positive rolling moment produces the discontinuity shown in Figure 3.3 in order for all roll stable configurations to have $C_{l,\beta} < 0$.

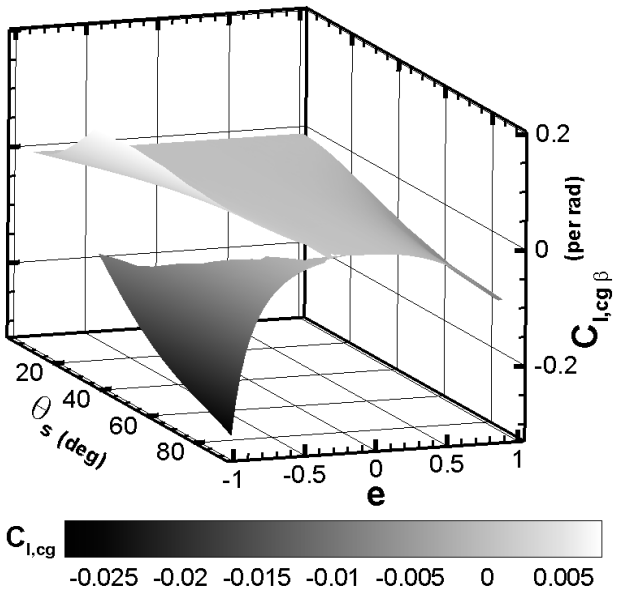

Figure 3.3. $C_{l,cg,\beta}$ distribution for spherical-segment, elliptical base ($n_2 = 2$), varying e and θ_s, $\alpha = 20^o$, $\beta = 5^o$.

As a result, if the positive rolling moment direction were kept constant, then there would be stable configurations with $C_{l,\beta} > 0$, and there would not be a discontinuity. With the sign reversal, Figure 3.3 clearly divides the stable and unstable oblate geometries. Phillips[68] includes a good discussion on roll stability in his flight mechanics textbook.

3.4.2. Determining the Location of the Center of Pressure

One of the assumptions of aircraft stability, $C_L >> C_D$, cannot be followed in a blunt-body analysis since blunt bodies usually have an $L/D < 1$. The assumption of $C_L >> C_D$ leads to the conclusion that the center of gravity must lie in front of the aircraft's neutral point (or the vehicle's center of pressure) to satisfy the requirement of $C_{m,cg,\alpha} < 0$ for longitudinal static stability.[31] Since this assumption does not apply to blunt-bodies, it may be possible to produce longitudinal static stability with the center of pressure in front of the center of gravity. From modified Newtonian results for $C_{m,cg}$ shown in Figure 3.4 for $-30^o \leq \alpha \leq 0^o$, it is determined that the $X_{cp}/l = 0.6556$ and Y_{cp}/l varied from 0.0000 to 0.5530 for a spherical-segment of $\theta_s = 25^o$ with a non-eccentric base. As a result, the code suggests that the Apollo CM with a $X_{cg}/l = 2.171$ is one successful example of maintaining longitudinal static stability with the center of pressure in front of the center of gravity.

Similar to X_{cp}/l being constant over a range of α for a spherical-segment $e = 0$, $\theta_s = 25^o$, it has been proven that $X_{cp}/l = 0.6667$ for a sharp cone in a Newtonian surface pressure field, suggesting that X_{cp}/l is independent of half-cone angle θ_c.[29] Note that not all spherical-segments have $X_{cp}/l = 0.6556$, but at least one does with θ_s

= 25°, e = 0 including the Apollo CM. The general pitching moment equations that relate X_{cp} and Y_{cp} to $C_{m,0}$ are given as Eqns. (3.20-3.22). These equations follow the coordinate system shown in Figure 3.1(b) that has a positive C_m corresponding to a nose-up moment. Bertin[29] notes that the axial force's contribution to the pitching moment is commonly neglected in the definition of the center of pressure location at and near zero angle-of-attack. However, this assumption does not apply to blunt-body aerodynamics because $C_{m,A,0}$ is commonly the dominant term for a blunt-body.

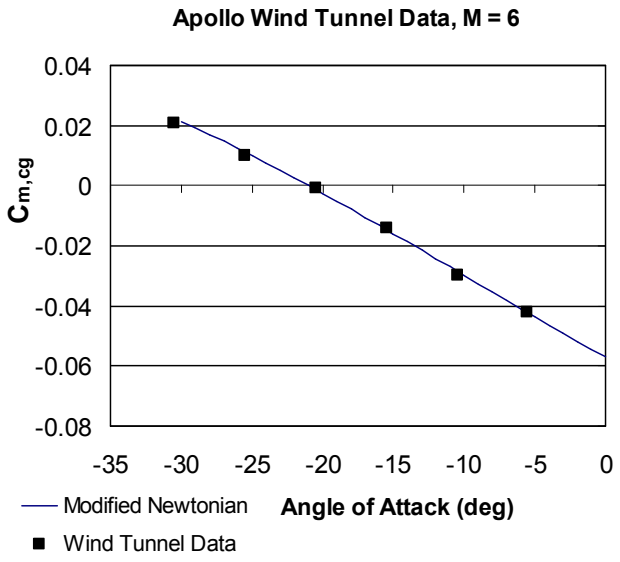

Figure 3.4. Variation in $C_{m,cg}$ with angle of attack.

$C_{m,N,0}$ is not usually the dominating term for slender bodies, in which case the resulting formula[29,30,55] for a circular cone at zero angle-of-attack $X_{cp}/l = 2/(3\cos^2\theta_c)$ can be used, but this equation complicates the analysis since X_{cp}/l is constant at 0.6667 without the assumption. When this assumption is applied to a blunt circular cone with θ_c = 70°, then X_{cp}/l = 5.7, which is not close to the actual X_{cp}/l = 0.6667. This assumption is only close to the exact solution for small θ_c, but a blunt-body cone

does not have a small θ_c. For a general blunt-body shape, the following relation does not determine the x-location of the center of pressure

$$\frac{X_{cp}}{d} \neq -\frac{C_{m,0}}{C_N}. \tag{3.60}$$

Instead, X_{cp}/l for a given blunt-body shape can be determined from the normal force's contribution to the pitching moment $C_{m,N,0}$ as shown in Eqn. (3.21).

Arora's 2003 aerodynamic shape optimization work[57] maximizes X_{cp}. Unfortunately, he equates X_{cp} to $C_{m,0}/C_N$, which contradicts Eqn. (3.60). Since he does not account for the axial force's contribution to the pitching moment, his work is an example of recent research that has made this incorrect assumption on basic blunt-body aerodynamics, rendering the published optimization results unusable. His conclusion is that the optimized X_{cp} value is 1.213 m, but a quick analysis of the geometry he chose accounting for the axial force's contribution to the pitching moment suggests that the actual X_{cp} is less than approximately 1.1 m, suggesting that his optimization results are within an infeasible region of x-locations due to the incorrect definition of X_{cp}. Additionally, his optimization results could be significantly different when accounting for the general relation of X_{cp} and $C_{m,0}$ given by Eqn. (3.20). Note that the incorrect definition of X_{cp} for a blunt body is included in Regan's first edition[55] and Rasmussen.[30] These are all examples of published work that show what Bertin[29] mentions is the conventional definition of X_{cp}, not the true definition of X_{cp} that is required to complete an aerodynamic analysis of blunt-bodies.

Chapter 4. Heat Transfer

Two heat transfer modes, convection and radiation, are considered in this work. The two arguably most important heat transfer characteristics are the heat flux and the heat load. The heat flux is power density in the form of heat per unit area. The heat load is equal to the heat flux integrated over the trajectory in time. It is common in the first analysis of a vehicle to look at the heat fluxes and heat loads at the stagnation point because this is usually accepted as the point of highest heat transfer.

This is not true for the Apollo CM, which re-entered at an angle of attack that brought the stagnation point near the corner radius. In such cases, as noticed in Ref. (35), the heat transfer is higher at the edge of the heat shield than at the stagnation point. In fact, the Apollo Command Module at $\alpha = \pm 33^{o}$ had a heat transfer flux at the edge that is 92% larger than that at the stagnation point corresponding to $\alpha = 0^{o}$, according to wind tunnel results,[35] but the actual CMs did not necessarily travel trajectories that required this high an angle of attack. The most likely reason that this was one of the highest angles of attack tested is because the conical shaped crew compartment that connected to the heat shield was at a 33^{o} angle with the horizontal. As a result, the flow would pass by the crew compartment flush at $\alpha = \pm 33^{o}$. The Apollo 4 CM traveled with a maximum angle of attack of $\pm 25^{o}$, in which the heat transfer at the edge is around 60% higher than at the stagnation point corresponding to $\alpha = 0^{o}$, according to other wind tunnel results.[36] In both the cases of $\alpha = \pm 25$ and $\pm 33^{o}$, the stagnation-point heat flux is approximately 15% larger than it would be at α

= 0^{o}.[35,36] As a result, the heat flux is higher at the edge of the heat shield than that at the stagnation-point of the Apollo CM.

Both the heat flux and heat load are equally important; however, for this work, only the heat flux is analyzed as it has been decided that the heat load would be determined with use of a trajectory code at a later time. This chapter explains the correlations applied in this work and their assumptions. The correlations were originally designed to calculate the stagnation-point heat flux on a sphere. Applying these correlations allows for the heat flux to vary with the radius of curvature of a given blunt body. Explanations on how these correlations are applied to blunt-bodies are included in the following sections. These correlations also vary with altitude through a freestream density factor and with speed through a freestream velocity factor. For this work the ARDC 1959 Model[69] and US Standard Atmosphere of 1976[70] have been applied. The 1976 standard atmosphere is applied for results, but the 1959 model atmosphere is used as noted throughout the text for the application of older correlations and code validation of results that used standard atmospheres before 1976.

4.1. Convection

The stagnation-point convective heat transfer correlation of Tauber[42] is applied in this work. Tauber assumes equilibrium flow conditions and a flight regime where boundary-layer theory is valid. Tauber produces a specific equation for planetary entry from satellite speed, but it is the objective of this work to approximate the heat transfer flux for planetary entry from both satellite and superorbital entry

speeds. To account for this, the general form of his correlations, which is given as Eqn. (4) of his article[42], is applied to produce the following correlation for the stagnation-point convective heat flux $\dot{q}_{s,conv}$

$$\dot{q}_{s,conv} = \left(1.83\times10^{-8}\right) r_n^{-0.5}(1-g_w)\rho_\infty^{0.5}V_\infty^3, \tag{4.1}$$

in which g_w is the ratio of wall enthalpy to total enthalpy. It is assumed that $g_w << 1$, and so g_w is zero in this work. This correlation assumes a fully catalytic surface. This correlation also holds true to the Fay and Riddell[43] derivation that states the $\dot{q}_{s,conv}$ is inversely proportional to the square root of the nose radius. Zoby[44] presents evidence that this relation breaks down for blunt bodies with ratio values of base radius r to nose radius r_n less than 0.6, in which $r_n > r$. He suggests that this is due to the velocity gradient being higher than would be otherwise expected by the deriving $\dot{q}_{s,conv} \propto r_n^{-0.5}$. If possible, this would be a good addition for future work. This is only one example that these heat transfer derivations are not accepted as fact in their application to blunt bodies, but they generate trends that are accepted as generally true for stagnation-point heat transfer.

The form of the correlation shown in Eqn. (4.1) was originally designed for calculating stagnation-point heat flux on a sphere. Since the stagnation-point convective heat flux relies mainly on the geometry nearby the stagnation-point, as opposed to the full body shape and size, it can be approximated by setting the radius of curvature equal to the nose radius. The nose radius is the term that relates the heat flux to the geometry in Eqn. (4.1). For the spherical-segment and spherically-blunted cone axial shapes, determining r_n is a trivial calculation. For the power law axial

shape, the slope of the shape at the tip of the nose may not necessarily be continuous, as in the case of setting $b = 1$, in which a sharp cone axial shape is generated.

As a result, the blunt-bodies with a power law axial shape must have an equivalent nose radius term produced. This equivalent nose radius is only an approximation and should not be accepted as a complete model for power law shapes. First, it is assumed that the power law shape's nose tip is blunted if its slope is discontinuous. Then the profile of the power law shape is examined; for this analysis, a line that is normal to the power law profile and that produces a 15^{o} angle with the horizontal is generated. A segment of that line that begins at the line's intersection with the power law profile and ends at its intersection with the horizontal central axis is produced. The effective radius is assumed to be equal to the average of the length of that line segment and the distance to the nose from the end point of that line segment on the horizontal axis. If the normal line intersects the power law curve beyond the base of the geometry (the intersection occurs outside of the heat shield shape), then the geometry's curvature is assumed sharp and given an effective radius value of 0.001 m. To produce a true method for determining the effective radius of the general power law shape for convective heat transfer is a research topic in itself.

4.2. *Radiation*

Because radiation over a blunt-body can be primarily modeled as an elliptic problem, the radiation at the stagnation point depends on the body of the vehicle in addition to the nose radius. Also, the radiative heat flux is significantly more sensitive to the angle-of-attack of the blunt body than the convective heat flux. In this work, all these effects are incorporated into the term called the effective radius. In order to apply $\dot{q}_{s,rad}$ correlations for spheres to non-spherical blunt-bodies, the effective radius in this work is directly related to the spherical radius for a given set of freestream conditions. This is accomplished by estimating the shock-standoff distance Δ_{so} across from the stagnation point at a given normal shock density ratio ρ_2/ρ_1 of the blunt body.

To calculate the normal shock density ratio ρ_2/ρ_1, high temperature properties of air must be determined in order to calculate an effective specific heat ratio after the normal shock $\gamma_{eff,2}$. Tannehill[54] supplies high temperature air correlations for this work, and they are also located in Chapter 11 of Anderson.[65] The effective specific heat ratio after the normal shock is determined through an iterative process. First, a test variable for $\gamma_{eff,2}$ is called $\gamma_{test,2}$ and set equal to 1.4 as an initial condition. Then the corresponding pressure p_2 and density ρ_2 after the normal shock are calculated based on $\gamma_{test,2}$

$$p_2 = p_1\left(1+\frac{2\gamma_{test,2}}{\gamma_{test,2}+1}\left(M_1^2-1\right)\right), \tag{4.2}$$

$$\rho_2 = \rho_1 \left(\frac{(\gamma_{test,2} + 1) M_1^2}{(\gamma_{test,2} - 1) M_1^2 + 2} \right), \tag{4.3}$$

and these two variables are entered into Tannehill's Fortran code that returns the corresponding enthalpy h_2 and $\gamma_{eff,2}$

$$h_2 = \frac{p_2}{\rho_2} \left(\frac{\gamma_{eff,2}}{\gamma_{eff,2} - 1} \right), \tag{4.4}$$

$$\gamma_{eff,2} = c_1 + c_2 Y + c_3 Z + c_4 YZ + \frac{c_5 + c_6 Y + c_7 Z + c_8 YZ +}{1 + \exp\left(c_9 \left(X + c_{10} Y + c_{11}\right)\right)}, \tag{4.5}$$

$$\text{in which } X = \log_{10}\left(\frac{p_2}{1.292} \right),\ Y = \log_{10}\left(\frac{\rho_2}{1.013 \times 10^5} \right),\ Z = X - Y, \tag{4.6}$$

and coefficients c_1 through c_{11} are curve-fit values tabulated in Tannehill.[54] For this work, only the $\gamma_{eff,2}$ is used. The value of $\gamma_{eff,2}$ is compared to $\gamma_{test,2}$; then $\gamma_{test,2}$ is set equal to the calculated $\gamma_{eff,2}$, and the process is iterated until the absolute value $|\gamma_{eff,2} - \gamma_{test,2}|$ is less than 0.01. Once a converged value of $\gamma_{eff,2}$ is determined, then the corresponding normal shock density ratio ρ_2/ρ_1 has been calculated and could be used in Kaattari's method described in Chapter 3 to approximate the shock-standoff distance.

It is assumed that the effective nose radius for stagnation-point radiative heat transfer, r_{eff}, for a given blunt body is equal to the radius of a particular sphere that maintains an equal shock-standoff distance. After calculating the normal shock-standoff distance, the corresponding spherical radius still would have to be determined.

According to wind tunnel results shown in Figure 4.1, the ratio of the normal shock-standoff distance to a sphere of radius r_{eff} is constant for a given normal-shock density ratio.

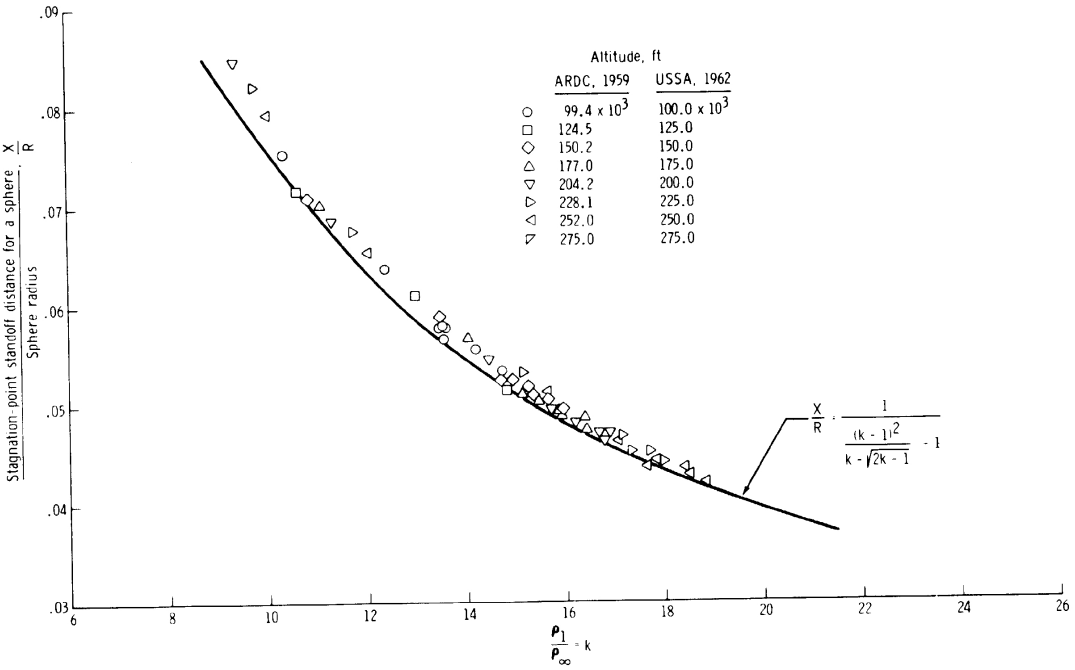

Figure 4.1. Stagnation-point shock-standoff distance wind tunnel data with empirical curve-fit, Ref. [48].

Ried[48] offers an empirical curve-fit that renders an acceptable approximation, also shown in Figure 4.1:

$$\Delta_{so}/r_{eff} = \left(\frac{\left(\frac{\rho_2}{\rho_1} - 1\right)^2}{\frac{\rho_2}{\rho_1} - \sqrt{\frac{2\rho_2}{\rho_1} - 1}} - 1 \right)^{-1} . \tag{4.7}$$

Then the r_{eff} from this equation replaces the sphere's radius in the stagnation-point radiative heat flux correlations. Three $\dot{q}_{s,rad}$ correlations are applied over a range of velocities. For V_∞ < 9000 m/s the correlation of the following form is applied

$$\dot{q}_{s,rad} = r_{eff}\, g_1 \left(\frac{\rho_\infty}{\rho_{sl}}\right)^{g_2} \left(\frac{V_\infty}{10000}\right)^{g_3}, \tag{4.8}$$

in which $g_1 = 100$, $g_2 = 1.6$, and $g_3 = 8.5$ from Ref. [29] for velocities below 7620 m/s and $g_1 = 6.8$, $g_2 = 1.78$, and $g_3 = 12.5$ for velocities from 7620 to 9000 m/s from Ref. [41]. For velocities above 9000 m/s, the Tauber and Sutton[45] equation is applied

$$\dot{q}_{s,rad} = 4.168 \times 10^4\, r_{eff}^H \rho_\infty^{1.22} f(V), \tag{4.9}$$

$$\text{in which } H = 1.072 \times 10^6 V_\infty^{-1.88} \rho_\infty^{-0.325},$$

and

$$f(V) = \begin{cases} -3.93206793 \times 10^{-12}\, \mathrm{V}_\infty^4 + 1.61370008 \times 10^{-7}\, \mathrm{V}_\infty^3 \\ -2.43598601 \times 10^{-3}\, \mathrm{V}_\infty^2 + 16.1078691 \mathrm{V}_\infty - 39494.8753, & 9000 \le V_\infty \le 11500 \text{ m/s} \\ -1.00233100 \times 10^{-12}\, \mathrm{V}_\infty^4 + 4.89774670 \times 10^{-8}\, \mathrm{V}_\infty^3 \\ -8.42982517 \times 10^{-4}\, \mathrm{V}_\infty^2 + 6.25525796 \mathrm{V}_\infty - 17168.3333. & 11500 < V_\infty \le 16000 \text{ m/s} \end{cases}$$

These curve-fit equations for $f(V)$ have < 2% difference with the published values.[45] Note that these curve-fit equations have coefficients with a high number of digits in order to produce the <2% error. It is suggested that all of these digits are maintained; if they are not, the values of $f(V)$ may go below zero for low V_∞ or produce extremely large values for high V_∞, either case producing erroneous results. The high number of digits does not correspond to the number of significant figures from this correlation. It is suggested that no more than three digits should be specified as significant for all three radiation correlations.

Chapter 5. Description of Code and Optimization Process

All of the presented theory has been implemented into a Fortran code for this work. For optimization, this code is linked to VR&D's Design Optimization Tools (DOT).[71] This chapter presents the layout of the code written for this work, a brief introduction to DOT and a summary of the chosen optimization method, and a list of studied objective functions with each one's value to this work.

5.1. Code Layout

The overall code layout is composed of three main components: the operating code, analysis code, and DOT. The overall code layout is shown in Figure 5.1. The operating code is the primary program from which all the other programs are managed. The analysis code determines the aerothermodynamic characteristics of a chosen blunt-body shape at given freestream conditions. Then the operating code calls DOT to determine the values of the design variables to be sent into the analysis code for each iteration of the optimization process.

The operating code includes all the settings and inputs required to operating the analysis and DOT codes. There are three operating modes available in this code. The single case mode can run the analysis code once at the given α and β to get the aerodynamic coefficients and the heat transfer determined. It can also run the analysis code five times in order to also calculate $C_{m,cg,\alpha}$, $C_{l,cg,\beta}$, and $C_{n,cg,\beta}$, which require the values of $C_{m,cg}$, $C_{l,cg}$, and $C_{n,cg}$ at four neighboring conditions (α+0.5^o, β), (α-0.5^o, β),

(α, β+0.5^o), and (α, β-0.5^o) for the second-order accurate finite-difference scheme mentioned in Chapter 3.

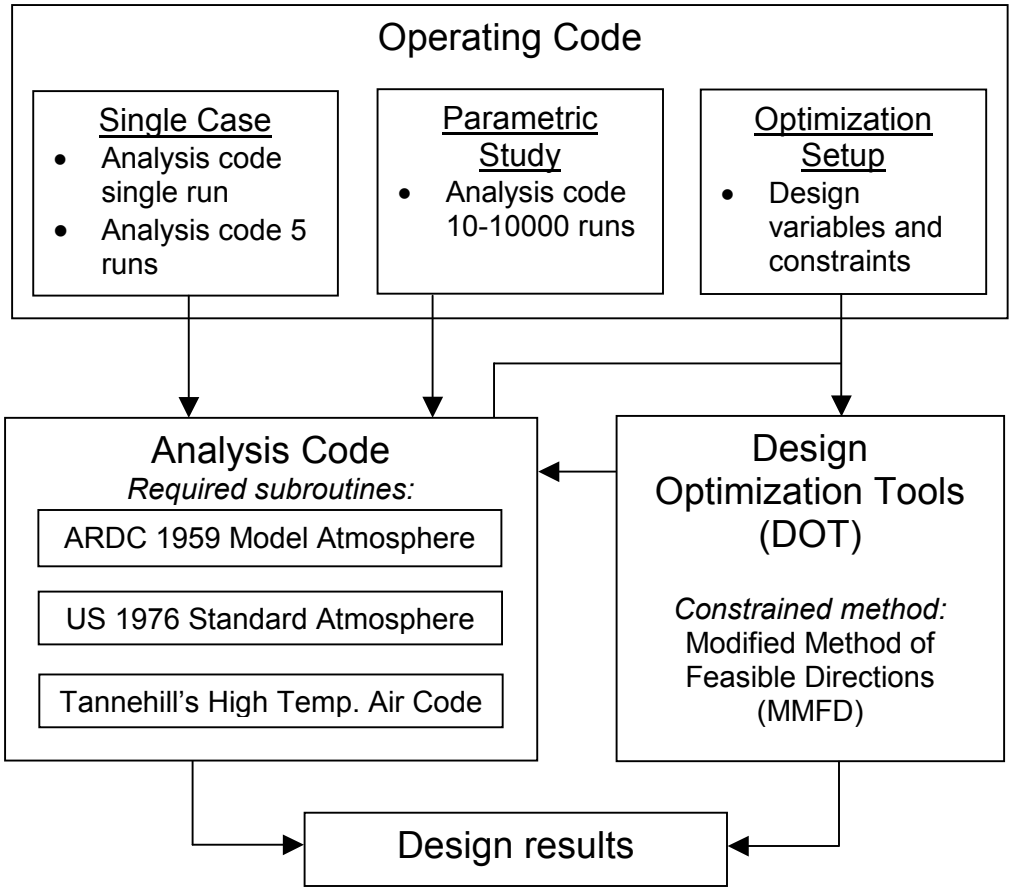

Figure 5.1. Diagram of Overall Code.

The second operating mode allows the user to conduct a parametric study of both geometric and freestream parameters for any geometric shape. It is possible to vary these variables at any resolution desired. Finally the third operating mode is the optimization setup that calls the DOT optimization routine. DOT determines the values of the design variables at which to run the analysis code based on a constrained method. DOT is setup in this work to use the modified method of feasible directions (MMFD) constrained method for optimization.

The analysis code has three objectives: to generate the blunt-body geometry, to determine its geometric properties, and to calculate the aerodynamics, static stability, and the stagnation-point heat transfer. A diagram of the analysis code is given in Figure 5.2. Given the geometric parameters of a chosen base and axial shape, the shape generator produces a 3D mesh of the heat shield geometry. The aerodynamics calculator determines the aerodynamic characteristics of a given shape based on modified Newtonian surface pressure distribution at a given angle-of-attack, sideslip angle, and Mach number. The primary variables that are calculated in the aerodynamics code are M_∞, α, C_L, C_D, L/D, C_N, C_A, $C_{m,0}$, $C_{l,0}$, $C_{n,0}$, X_{cp}/L, Y_{cp}/L, Z_{cp}/L.

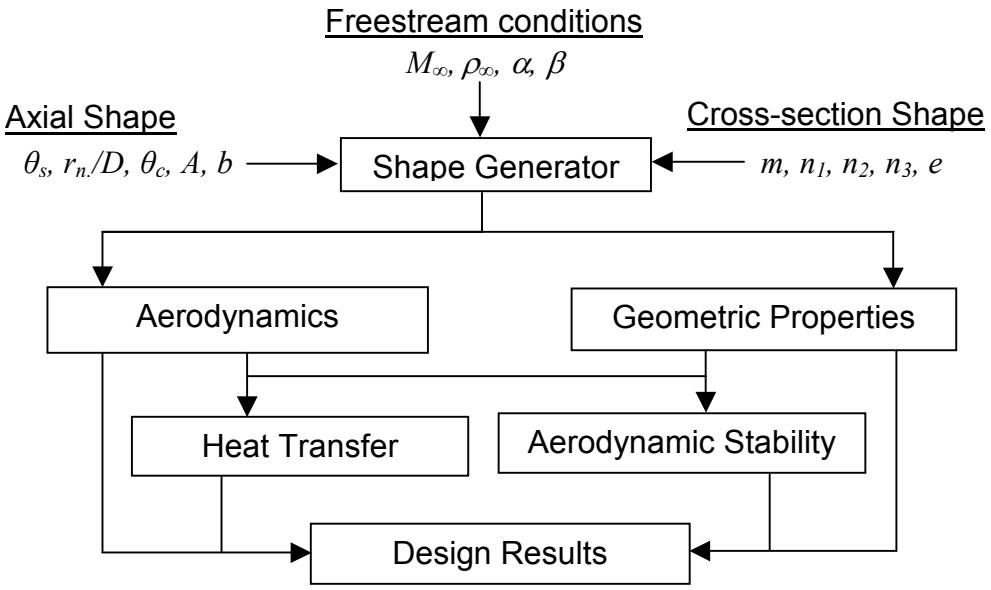

Figure 5.2. Diagram of Analysis Code.

The aerodynamics calculator is acceptable for determining blunt-body shape hypersonic aerodynamics at fine mesh sizes with extremely low run times (usually a fraction of a second for a j_{max} = 121, k_{max} = 203 mesh). Additionally, the aerodynamics code uses Tannehill's code to determine $\gamma_{\text{eff},2}$ and ρ_2/ρ_1, and it uses Kaattari's method to determine the shock-standoff distance Δ_{so} to the stagnation-point

that are used in the heat transfer portion of the code. The primary output of the heat transfer portion of the code are r_{eff}, $\dot{q}_{s,conv}$, and $\dot{q}_{s,rad}$.

The analysis code applies a 5th-order accurate Simpson's Rule integration method to determine the aerodynamic characteristics and center of gravity location. The center of pressure location is then determined. Geometric properties such as the volume, surface area, and planform area are calculated in the analysis code. Additionally, a center of gravity can be either chosen or calculated assuming a uniform density volume. The static stability calculator uses the aerodynamics in conjunction with the location of the center of gravity to determine the moment coefficients about the center of gravity and the pitch, yaw, and roll stability derivatives. Note that the analysis code requires two atmospheric models and Tannehill's high temperature air code. Two atmospheric models are programmed in order to use the older atmospheric model for part of the validation process of the heat transfer correlations.

5.2. Design Optimization Tools (DOT)

Vanderplaats Research & Development, Inc.'s Design Optimization Tools (DOT)[71] is professional software program that varies design variables based on a gradient-based minimization method to determine an optimum value of an objective function. DOT offers both unconstrained and constrained minimization methods. Broydon-Fletcher-Goldfarb-Shanno (BFGS) and Fletcher-Reeves (F.R.) are the two unconstrained minimization methods available in DOT. When DOT refers to unconstrained methods, it means that there are no constraints present except those on

the design variables that DOT varies. The constrained methods offer the ability to restrict values on non-design variables or a combination of variables based on theory limits or other reasons. The constrained minimization methods available in DOT include the Modified Method of Feasible Directions (MMFD), Sequential Linear Programming (SLP), and Sequential Quadratic Programming (SQP). MMFD is the most reliable of the three and requires less memory than the other two methods.[71]

The following optimization problem is solved by DOT: find the values of NDV design variables contained in $\vec{X}$ that will minimize or maximize $\text{OBJ} = O(\vec{X})$, in which the OBJ is the objective function, subject to constraints $G_q(\vec{X}) \leq 0$ for $q = 1$ to NCON, in which NCON is the number of constraints, and design variables X_p have side constraints $X_p^L \leq X_p \leq X_p^U$ for $p = 1$ *to* NDV, in which NDV is the number of design variables.[71]

For this work, DOT has been setup to use MMFD to vary the design variables to find an optimum value of an objective function, in this case, an aerothermodynamic parameter or combination of parameters. MMFD uses the following overall process. The objective function and constraints are first evaluated at the user inputted initial values of the design variables. Then the gradient of the objective function and constraints are calculated, and a search direction E is created. Then a one-dimensional search is completed to find the scalar parameter α^* that minimizes $O(\vec{X})$. Scalar parameter α^* is used to find a new $\vec{X}$ that is set equal to the sum of the initial $\vec{X}$ and the product of α^* and the search direction,

$$\vec{X}^u = \vec{X}^{u-1} + \alpha^* E^u, \tag{5.1}$$

in which u is the iteration number. If convergence is not satisfied, then iterations of the following process are completed until convergence requirements including the Kuhn-Tucker conditions are satisfied.[71]

The three Kuhn-Tucker conditions[71] must be satisfied for obtaining convergence using MMFD. The first is that optimum design $\vec{X}^*$ must be feasible, or produce constraint values $G_q(\vec{X}^*) \leq 0$ for q = 1 to NCON. The second condition is that the product of the Lagrange multiplier λ_q and $G_q(\vec{X}^*)$ must be zero. The third condition is that the gradient of the Lagrangian becomes zero, in which the gradient of the Lagrangian is

$$\nabla O(\vec{X}^*) + \sum_{q}^{\text{NCON}} \lambda_q \nabla G_q(\vec{X}^*) = 0. \tag{5.2}$$

Detailed descriptions of MMFD and the Kuhn-Tucker conditions are included in Appendix E of Ref. (71). A quick analysis of several different objective functions is discussed in the next section.

5.3. *Choosing Objective Functions*

A quick analysis of the results of 57 unconstrained optimizations on 57 different objective functions has been completed to determine which objective functions to use, to observe any trends in the results, and to notice any unexpected results. For this analysis, each objective function was maximized. The design variables and their initial designs for this preliminary optimization for a hexagonal m = 6, n_1 = 2.3 superellipse cross-section shape and spherical-segment axial shape are

$$\vec{X}^0 = \begin{bmatrix} \theta_s \\ n_2 \\ e \end{bmatrix} = \begin{bmatrix} 35^o \\ 2.5 \\ -0.2 \end{bmatrix}. \tag{5.3}$$

The ranges of values for these design variables are $5^o \leq \theta_S \leq 89^o$, $-0.95 \leq e \leq 0.95$, and $1.50 \leq n_2 \leq 4.0$. The freestream conditions for the Newtonian flow model include $M_\infty = 30$ and negative $\alpha = 25^o$ at an altitude of 200,000 ft.

In addition to single term objective functions, the fifty-seven are composed also of linear combinations or products of aerodynamic coefficients, stability coefficients, and geometric parameters. The objective functions included in Table 5.1 rendered the better aerodynamic results out of the 57 objective functions and are thereby listed as the most useful objective functions. Each number in the left column corresponds to the number of variables in each objective function.

Table 5.1. Most useful objective functions.

	Objective Functions
1	C_L, C_D, L/D, L_V/D, L_H/D, $C_{L,V}$, $C_{L,H}$, $C_{m,cg}$, $-C_{m,cg,\alpha}$, $C_{n,cg,\beta}$, $-C_{l,cg,\beta}$, η_v
2	$C_L C_D$, $C_L + L/D$, $C_{n,cg,\beta} - C_{m,cg,\alpha}$, $-\eta_v C_{m,cg,\alpha}$, $\eta_v L/D$
3	$-C_{m,cg,\alpha} + C_L + L/D$, $-C_{m,cg,\alpha} + C_{n,cg,\beta} - C_{l,cg,\beta}$
4	$-C_{m,cg,\alpha} + C_{n,cg,\beta} - C_{l,cg,\beta} + L/D$

The better objective functions that are made up of three or four variables were noticed to not be multiplied, only added. The objective functions that produced results that were either not as good but still acceptable or produced mediocre results are as questionable objective functions in Table 5.2.

Table 5.2. Questionable objective functions.

Objective Functions	
2	$-C_{m,cg,\alpha} + C_L$, $-(C_{m,cg,\alpha} + C_{l,cg,\beta})$, $L/D - C_{m,cg,\alpha}$, $C_{m,cg} - C_{m,cg,\alpha}$, $C_{m,cg}\, C_{m,cg,\alpha}$, $-C_{m,cg,\alpha} C_{l,cg,\beta}$
3	$C_L + C_D + L/D$, $-(C_{m,cg,\alpha} + C_{l,cg,\beta})\, C_{n,cg,\beta}$

Then there are several objective functions that produced results that were not acceptable from an aerodynamic and static stability standpoint. These objective functions are listed in Table 5.3.

Table 5.3. Objective functions to use with caution.

Objective Functions	
1	C_L^2, S_{hs}, V_{hs}
2	$C_L + C_D$, $C_L\, L/D$, $C_D + L/D$, $-C_{m,cg,\alpha} C_L$, $-C_{m,cg,\alpha}\, L/D$, $-C_{m,cg,\alpha}\, S_{hs}$, $-C_{m,cg,\alpha}\, \eta_v$, $\eta_v\, S_{hs}$, $L/D\, S_{hs}$, $C_L\, S_{hs}$, $C_D\, S_{hs}$, $L/D\, V_{hs}$
3	$C_L\, L/D + C_D$, $-C_{m,cg,\alpha} + C_L\, L/D$, $C_{m,cg,\alpha} C_{n,cg,\beta} C_{l,cg,\beta}$, $C_{m,cg,\alpha} C_{l,cg,\beta} + C_{n,cg,\beta}$, $C_L\, L/D((C_{m,cg,\alpha})^2)^{1/4}$, $-C_{m,cg,\alpha}\, \eta_v\, S_{hs}$
4	$C_{m,cg,\alpha} C_{l,cg,\beta} + C_{n,cg,\beta} + L/D$, $-(C_{m,cg,\alpha} + C_{l,cg,\beta}) C_{n,cg,\beta}\, L/D$

Some of these results may not be intuitive. For example, this analysis suggests that maximizing surface area or volume individually produces results that are not as acceptable from an aerodynamic and static stability standpoint as maximizing objective functions from the other two sets. Note that this is not meant to be a perfect test of objective function effectiveness but just a way to determine which objective functions would be worth working with first.

Chapter 6. Design Code Validation

To validate the design code, and the corresponding implemented theories, results of the design code are compared to data from the Apollo and FIRE II missions. The results are divided into two areas: (1) aerodynamic performance and static stability and (2) stagnation-point heat transfer. The first section notes that the aerodynamic coefficients and stability derivatives match the Apollo data within 15%. The second section observes that the maximum heat transfer heat flux and heat load is within 15% of actual predictions after the stagnation-point heat transfer heat flux is related to the maximum heat flux according to wind tunnel data.

6.1. Aerodynamics and Static Stability

The aerodynamic performance and static stability are compared to both Apollo wind tunnel data and Apollo flight test data. There is more certainty in the Apollo wind tunnel data than in the Apollo flight test data, and most of the wind tunnel data is for $M_\infty = 6$ while the flight test data is for $M_\infty = 36$. To convert from the listed angle of attack value of the NASA Apollo reports to the angle of attack value used in this work, defined in Figure 3.1(a), subtract 180^o from the NASA reported value. This should usually convert the NASA reported value to a negative angle of attack. Note that there is not any truly acceptable experimental data on the rolling moment stability coefficient, but predictions are compared to Whitmore's recent computational work.[28]

6.1.1. *Comparison with Apollo Wind Tunnel Data*

Results from the code based on modified Newtonian theory, have been compared to wind tunnel[8,9] data of the Apollo Command Module (CM). The center of gravity is offset from the central body axis in order to trim the Apollo CM at a specific angle-of-attack during re-entry.[10] Different center of gravity locations were considered in the wind tunnel models during the design of the CM. [8,9,11] In Figure 6.1, the center of gravity location is $X_{cg}/l = 2.171$, $Y_{cg}/l = 0.3158$, and $Z_{cg}/l = 0.0$ according to the body-fixed coordinate system in Figure 3.1(b).

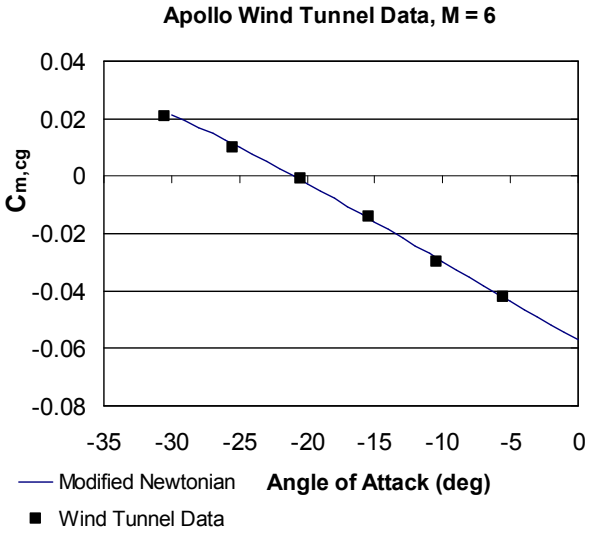

Figure 6.1. $C_{m,cg}$ comparison between modified Newtonian and wind tunnel data, Ref. [8].

Additionally, because $X_{cg}/l > 1$, the center of gravity location of the CM is past the heat shield. The Newtonian results for the pitching moment $C_{m,cg}$ at $M_\infty = 6$ in Fig. 5 produce $C_{m,cg,\alpha} = -0.16$/rad; the modified Newtonian results follow the behavior and closely agree with the values of the Apollo wind tunnel (WT) data.[8] As a result, this is evidence that the modified Newtonian results can match the pitching moment closely and thus predict α_{trim}, and it is well-known to match the lift-to-drag ratio for a blunt body better than the lift or drag coefficients.

The wind tunnel data for the rolling moment C_l was scattered near zero and has values that are two orders of magnitude smaller than those measured for C_m. Although the data accuracy of C_l and C_m is not reported for this wind tunnel data, the scattering and smaller values of the C_l data points in Fig. 6 suggest that the measurement instruments did not have the precision required to obtain a clear data set of the CM's rolling moment behavior.

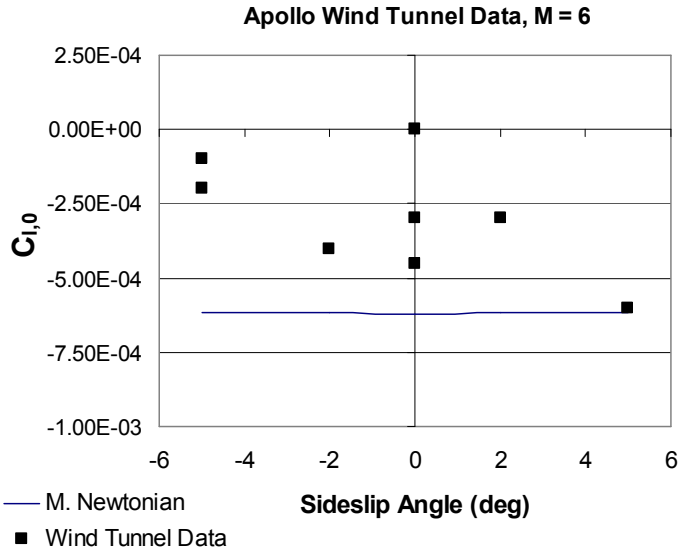

Figure 6.2. $C_{l,0}$ comparison between modified Newtonian and wind tunnel data, Ref. [8].

The wind tunnel data suggest a neutrally stable spherical-segment at -20° angle-of-attack, and the modified Newtonian results agree. A mesh with j_{max} = 203 and k_{max} = 121 has been chosen based on a grid convergence study. Since the Apollo CM is axisymmetric, the yawing moment coefficient $C_{n,0}$ at a given sideslip angle (the condition $\beta_1 \neq 0$, $\alpha_1 = 0$) would be equivalent to the pitching moment coefficient $C_{m,0}$ at a given angle-of-attack (the condition $\alpha_2 = \beta_1$, $\beta_2 = 0$). This is one reason that no specific $C_{n,0}$ data exists in the references.

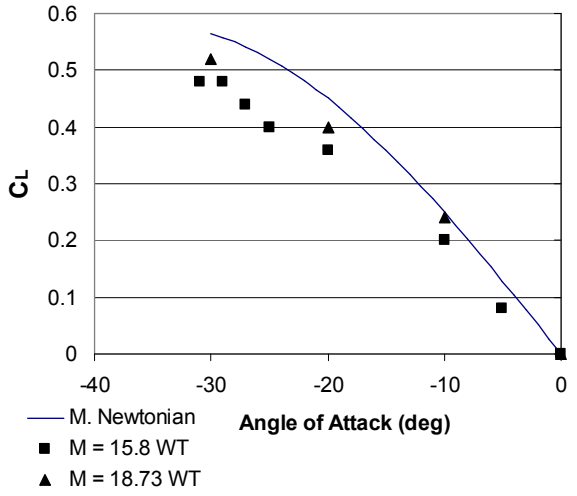

a) Validation of C_L results.

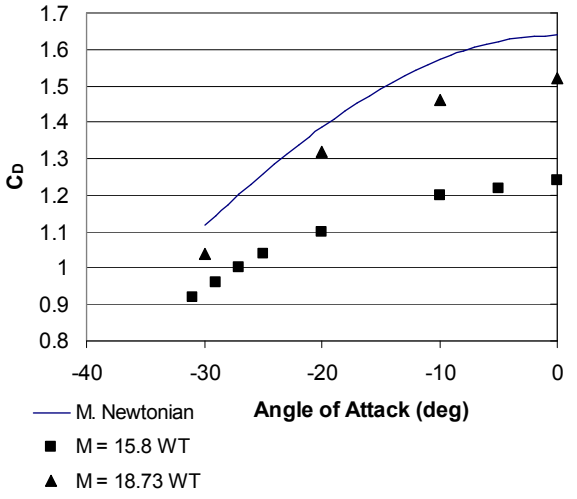

b) Validation of C_D results.

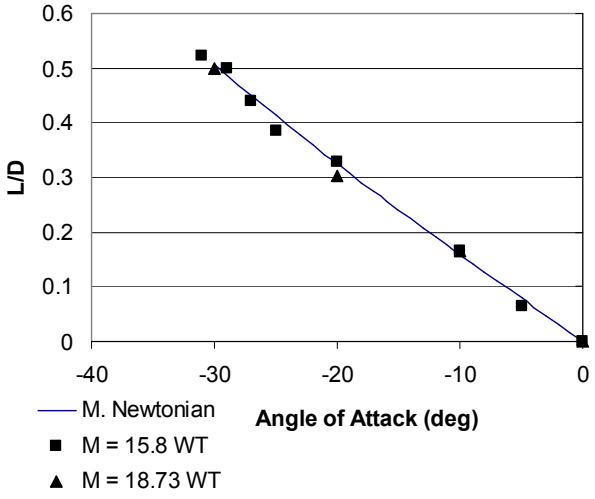

c) Validation of *L/D* results.

Figure 6.3. Aerodynamic force comparisons between modified Newtonian and wind tunnel data, Ref. [8].

The modified Newtonian results in Figure 6.3 were calculated at $M_\infty = 18.73$, but the difference between these results and those at $M_\infty = 15.8$ is negligible (0.05% difference at $\alpha = -20^o$). Modified Newtonian results for the lift and drag coefficients are larger than values from both datasets shown in Figure 6.3(a) and (b). However, the increase in lift and drag with an increase in Mach number in the wind tunnel data is more significant than expected; this may suggest the presence of significant wind tunnel effects. At M_∞=18.73, C_L and C_D from Newtonian theory are at most 9.6% and 7.2% larger than the wind tunnel data respectively, and they are within the uncertainty of the wind tunnel data of ±0.114 for C_L and ± 0.10 for C_D.[8] *L/D* Newtonian results shown in Figure 6.3(c) agree very well with the wind tunnel data (better than for the individual C_L and C_D as expected).

At lower freestream Mach numbers, such as M_∞=9, the errors are larger than 10% for the lift coefficient as shown in Table 6.1. While the data presented for M_∞=15.8 and 18.73 are based on Apollo CM models with r_c/d of approximately 0.1, the data in Table 6.1 corresponds to r_c/d = 0.0. Moseley conducted a survey of the effect of increasing r_c/d, and his wind tunnel results for M_∞=9 at r_c/d = 0.1 would increase the errors from those values in Table 6.1, for C_L to approximately 22% and C_D to approximately 13% while the error in *L/D* was constant at 8% at $\alpha = -15^o$.

Table 6.1. Percent error of Newtonian computations compared to wind tunnel data, $M_\infty = 9$, in Ref. [9], Percent error averaged over $-30^o \le \alpha \le 0^o$.

	Average Percent Error	Maximum Percent Error	α of Maximum Percent Error
C_L	0.45	0.534	18.6%
C_D	1.25	1.296	3.70%
L/D	0.37	0.412	11.3%

As the code used in this work does not account for corner radius in determining the surface pressure distribution, this is one reason for the increase in error. The Newtonian surface pressure distribution is known to become more accurate with an increase in Mach number, and the validation results are consistent with this understanding. However, it is shown in the next section that comparisons with the flight test data from Apollo AS-202 result in an amount of error similar to that for M_∞=9. Overall, the modified Newtonian results are within 10% of the wind tunnel data with corner radius for $M_\infty \geq 18.73$, within 15% of the wind tunnel data without corner radius for $M_\infty \geq 9$, and within 25% of wind tunnel data with corner radius for $M_\infty \leq 18.73$.

6.1.2. Comparison with Apollo Flight Test Data

Results from the code have been compared to flight test[6,7] data for the Apollo Command Module (CM) for mission AS-202 and Apollo 4 (also known as AS-501). The CM in AS-202 re-entered Earth's atmosphere at satellite orbit speed 8.23 km/s (27,000 ft/s) while the Apollo 4 CM produced the expected re-entry velocity from lunar return of 10.7 km/s (35,000 ft/s).

The uncertainty in the flight data varies throughout the trajectory, and so the more steady aerodynamic data was identified and utilized. Of the two datasets, the flight data from AS-202 had the smaller uncertainty in the flight coefficient data of ±9% at 4900 s into the mission. The coefficients of the normal force, lift, and lift-to-drag ratio have percentage errors around this error. However, the coefficients of the

axial force and drag have higher errors around 17%. The Newtonian results are compared to the AS-202 flight data in Table 6.2.

Table 6.2. Comparison of Apollo AS-201 Data and Computations, $M_\infty = 14$, $\alpha = -16.5^o$ at 4900 s.

	AS-201 [ref. 6]	Mod. Newtonian	% Error
C_N	-0.05	-0.0454	-9.2%
C_A	1.34	1.56	16.2%
C_L	0.37	0.399	7.8%
C_D	1.28	1.51	17.6%
L/D	0.289	0.265	-8.4%

The trend in the percentage error being higher for C_L than C_D seen in the wind tunnel data comparison is the opposite for AS-201. Because the corner radius is not accounted for, it is expected that the error in L/D to stay constant at 8%, for C_L, according to wind tunnel results, to have approximately 22% error instead of 7.8% and C_D to have approximately 13% instead of 17.6%. Note that these percentage errors are nearly constant, at least over the range of angle of attack values from -30^o to 0^o. It is completely feasible for C_D to have a difference in error of 4.6% since the uncertainty is a higher percentage, and so the only surprising trend is that the lift coefficient has 14% less error than expected.

From the wind tunnel data, it is suggested that the corner radius affects the lift and drag coefficients less at higher freestream Mach numbers, but this is countered with the higher errors present in the AS-201 flight test data. In fact, wind tunnel effects could be changing the trends also, and so it is apparent that there is not consistency throughout this wind tunnel and flight test data to the resolution required to reason for the different percentage errors. Therefore, no conclusions could be made concerning whether the modified Newtonian results are less than 18±9% accurate.

Compared to flight data for Apollo 4 at $M_\infty = 30$, Newtonian theory produces a C_D that is 3.7% larger and a C_L that is 18.6% larger as shown in Table 2.[7] According to Hillje, the best flight-derived data for C_N (near maximum freestream dynamic pressure) has an uncertainty of ±0.048.[7] Because the normal force coefficient has a small magnitude, small precision errors in C_N strongly affect the calculation of C_L. The contribution of C_N to C_L is one order of magnitude less than the contribution of C_A to C_L. However, the contribution of C_N to C_D is two orders of magnitude less than the contribution of C_A to C_D, and so an error in C_N will not affect C_D as much as C_L. This produces significant increase in accuracy of the Newtonian results for C_D at 3.7% compared to C_L at 18.6%.

Table 6.3. Comparison of Apollo 4 Data and Computations, $M_\infty = 30$, $\alpha = -25^o$ at 30040 s.

	Apollo 4 [ref. 7]	Mod. Newtonian	% Error
C_N	-0.11	-0.06387	-41.9%
C_A	1.32	1.400	6.1%
C_L	0.45	0.5337	18.6%
C_D	1.25	1.296	3.7%
L/D	0.37	0.4119	11.3%

Additionally, Newtonian theory produces results that trim the CM within 1.2° for both Apollo missions AS-202 ($\alpha = 17.5^o \pm 0.5^o$)[6] and Apollo 4 ($\alpha = 25.5^o \pm 3^o$).[7] For all these reasons, it is concluded that the C_N flight data is probably inaccurate, rendering the higher percentage errors in C_L and L/D. Since the percentage differences between Newtonian theory and the acceptable CM experimental wind tunnel and flight data is less than 15%, and since the theory follows the behavior of the wind tunnel data, modified Newtonian flow is considered acceptable for comparing the basic hypersonic aerodynamic characteristics of the investigated blunt-

body heat shield shapes with low computational time. Only the rolling moment values and stability derivatives have not been completely validated since a lack of this data exists, but it is partly validated in the next section.

6.1.3. Comparison with Additional Sources

Whitmore[28] offers a recent analysis of the Apollo capsule as well as other human-rated lunar return vehicles such as a flattened bi-conic with trim flaps and an HL-20-derived lifting body configuration. His numerical results on the stability characteristics of the Apollo capsule closely match the results of this work's code. Whitmore also uses a modified Newtonian surface pressure distribution to determine the aerodynamics of each vehicle.

Both the results of this work and of Whitmore suggest that the Apollo capsule is slightly statically unstable in the roll direction. In this case, to be statically roll stable, the vehicle would have a negative value of $C_{l,cg,\beta}$ since vertical lift is positive at negative angles of attack for the Apollo CM. Both works indicate that the Apollo capsule would have slightly positive values for the $C_{l,cg,\beta}$, if the center of gravity is above the central axis during planetary entry.

Since the Apollo CM had a Reaction Control System (RCS) that could control the Command Module's roll angle, one guess is that the RCS may have been used once in a while to fix the CM's roll alignment. Another guess is that the $C_{l,cg,\beta}$ had a negligible value for the CM. Whitmore reports a value of $C_{l,cg,\beta}$ = 0.0065/rad while this work produces a value of $C_{l,cg,\beta}$ = 0.00541/rad at $\alpha = -16^{o}$ to produce L/D = 0.25. Since both of our works concur and Whitmore's work is the only source in the

literature search that offered a value to compare, this is the extent that the $C_{l,cg,\beta}$ is validated in this work.

Magazu[26] investigated the feasibility and aerothermodynamic performance of a 12-sided parashield re-entry vehicle that has a shape similar to a 12-sided umbrella with no more than 7% concavity. The reproduction of this heat shield shape is defined as having a spherical-segment axial shape with $\theta_s \approx 45^o$ and a dodecagon cross-section without any concavity. The superformula of the superellipse Eqn. (2.8) can approximate a sharp dodecagon with the following parameters $m = 12$, $n_1 = 10.75$, $n_2 = n_3 = 1$. With these parameters, this work's code produced a lift-to-drag ratio of 0.19 compared to the reported 0.18 in Ref. [26] at $\alpha = -15^o$.

6.2. Stagnation-Point Heat Transfer

Validating the results of this work's stagnation-point heat transfer methods against Apollo and FIRE II experimental and flight data is completed in this section. It is shown that the methods produce results with < 15% error. Note that it is not the purpose of this work to imply from these low errors that heat transfer during planetary entry is well understood. CFD would also produce results with errors of approximately 10-15% also. Additionally, although the percentage error is low for the stagnation-point heat transfer methods of this work, the error would probably increase dramatically for entry velocities greater than 12 km/s, in which it is expected that radiation cooling and convection coupling would lower the radiative heat flux. However, it is unknown precisely how much reduction there would be since no instrumented flight tests have been completed on flights with entry speeds greater

than 11.4 km/s from the FIRE II. Several questions still exist on laminar, transitional, and turbulent boundary layer heat transfer during planetary entry. As a result, experimental research in this area would be especially worthwhile as future work.

6.2.1. Apollo 4

The peak radiative heat flux for the Apollo 4 mission occurred at an altitude of approximately 200000 ft around 30030 s into the mission at which point the Command Module was moving at a speed of 34000 ft/s. For the portion of the trajectory with high radiative heat flux, Figure 6.4 shows the calculated normal-shock density ratio and corresponding specific heat ratio using Tannehill's correlation set.[54]

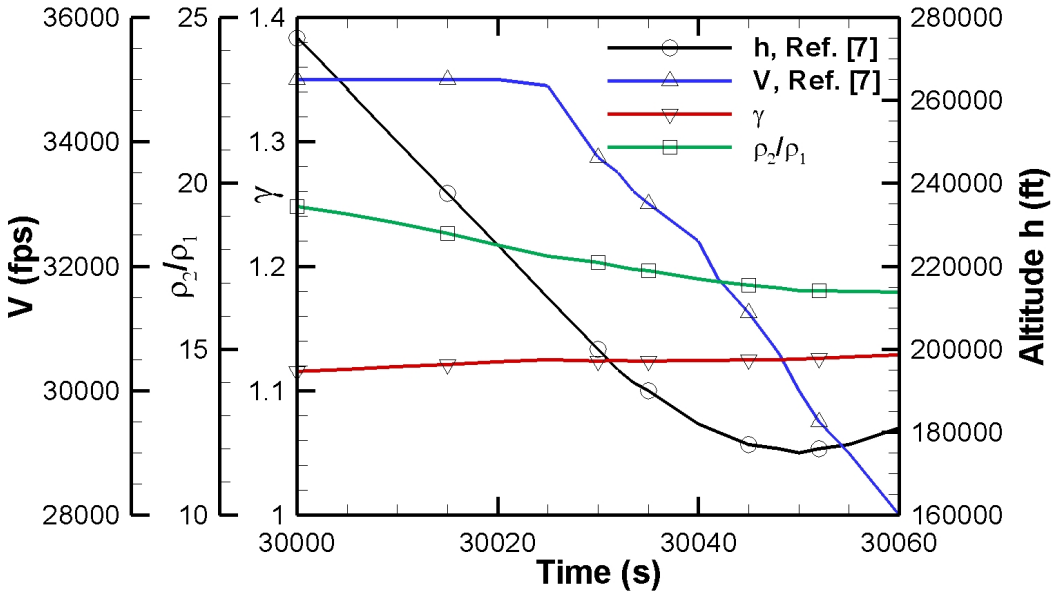

Figure 6.4. Normal-shock density and specific heat ratios for the high radiative heat flux portion of the Apollo 4 trajectory.

The altitudes and velocities during this portion of the Apollo 4 trajectory are also shown in Figure 6.4. The stagnation point on a blunt-body is usually across from the part of the bow shock that is normal to the freestream. As a result, the normal-shock density ratio ρ_2/ρ_1 and corresponding effective specific heat ratio after the shock can

be used to approximate the effective radius-of-curvature at the stagnation point. Kaattari's method requires ρ_2/ρ_1 and $\gamma_{eff,2}$ to determine r_{eff}. To validate the implementation of Kaattari's method in this work, in Figure 6.5 it is compared to other methods of determining the shock-standoff distance for the case of a sphere. This figure is partially a reproduction of Figure 4.1 in which the empirical curve-fit Eqn. (4.8) is compared to wind tunnel data. As a result, it can be observed that Kaattari's method in Figure 6.5 follows the experimental data closer than the empirical curve-fit at the lower values of ρ_2/ρ_1. Rasmussen[30] provided the solutions to the Vorticity method and parabolic thin shock layer approximation in his textbook. The solution from the Vorticity method follows the behavior of Eqn. (4.8) almost perfectly while the parabolic thin shock layer approximation produces shock-standoff distances that are at least 25% larger than wind tunnel results.

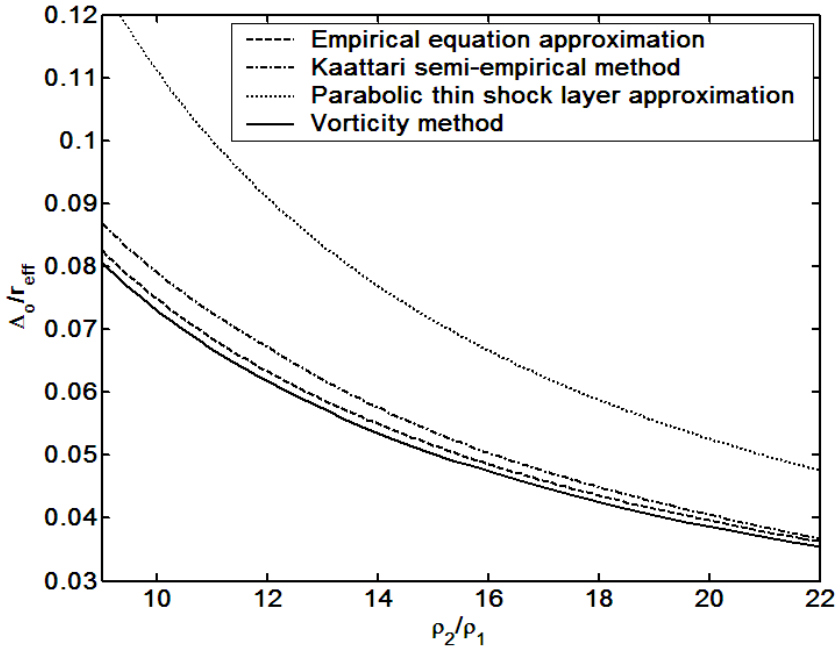

Figure 6.5. Shock-standoff distance method comparison.

It is noticed that Kaattari's method and Eqn. (4.8) bracket most of the wind tunnel results shown in Figure 4.1. After Kaattari's method determines the shock-standoff distance at zero angle of attack, the modified method for finding the shock-standoff distance at the prescribed angle of attack is accounted for through the effective radius term. For the Apollo 4, Ried[48] generated predictions with early 1970 computer technology using CFD. Ried produced an effective radius at the stagnation point that would apply for radiative heat transfer, and it is compared to the results of Kaattari's modified method in Figure 6.6.

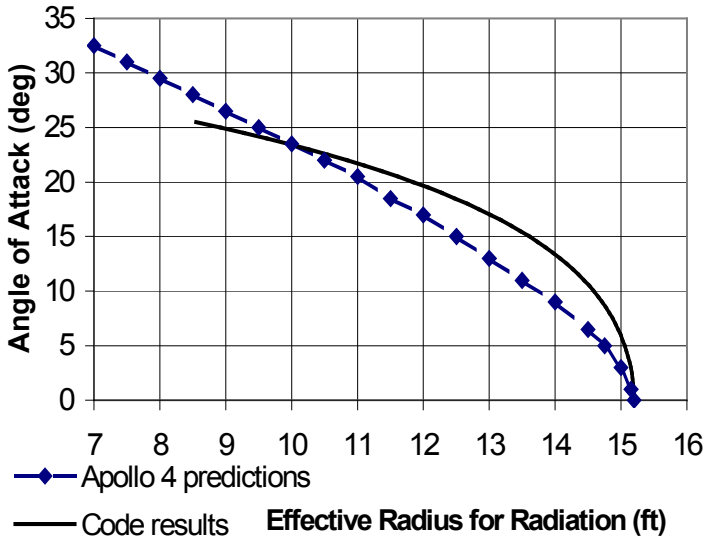

Figure 6.6. Apollo 4 r_{eff} for stagnation-point radiative heat transfer.

Kaattari's modified method varies no more than 10% from Ried's predictions. Then the r_{eff} is applied in the radiative heat flux correlation set. To determine which correlations would be best to apply for this work, a plot of the Apollo 4 mission's radiative heat flux shown in Figure 6.7 is used to compare correlations. Figure 6.7 shows these results for the portion of the Apollo 4 trajectory with high radiative heat flux. Both radiometer and calorimeter measurements were made on the Apollo 4 at

the point of maximum heating and the stagnation point, although measurement uncertainties were not recorded. Ried shows that his calculations match the radiometer results that measured only the visible and infrared radiation. He also calculated the UV continuum and UV line radiation.

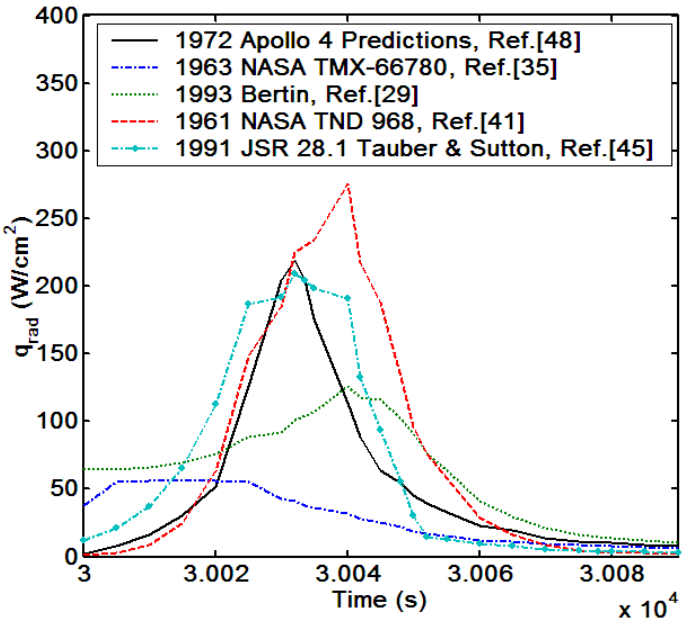

Figure 6.7. Validation of radiative heat flux correlations for Apollo 4.

It made the most sense to compare the values of the correlations to the total radiative heat flux. As a result, the total radiative heat transfer that includes the visible, infrared, UV continuum, and UV lines is shown in Figure 6.7 as the Apollo 4 predictions. The most recent correlation from Tauber and Sutton[45] matched the Apollo 4 results for most of the region. However, the results of this correlation do not match the predictions for speeds less than 9000 m/s.

In fact, both Lovelace[41] and Bertin[29] provide correlations that produce conservative results that are not far from the results for speeds less than 9000 m/s. Since the correlation from Bertin was originally designed for speeds less than 7620 m/s (25000 ft/s), Lovelace's correlation is applied for speeds less than 9000 m/s.

Along with a method to transition between the two correlations, Lovelace and Tauber's correlations are used in this code and produce the results shown in Figure 6.8. Together, these correlations produce results that are conservative but close enough for first-order optimization results.

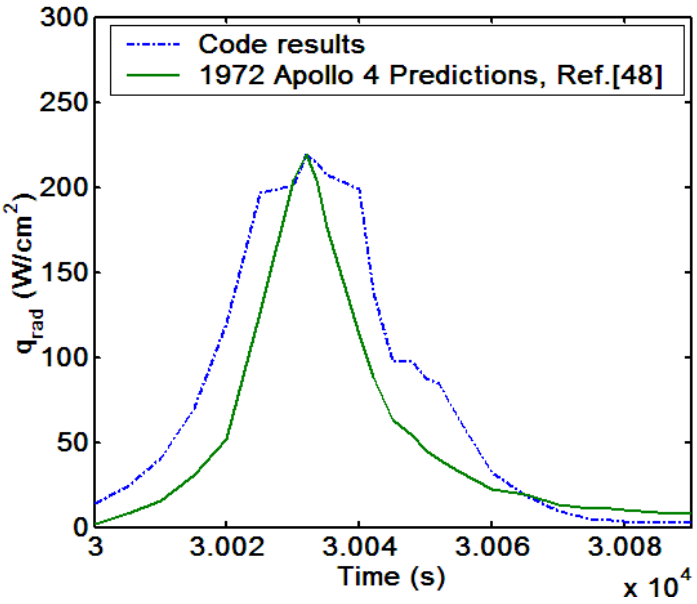

Figure 6.8. Apollo 4 radiative heat transfer code validation.

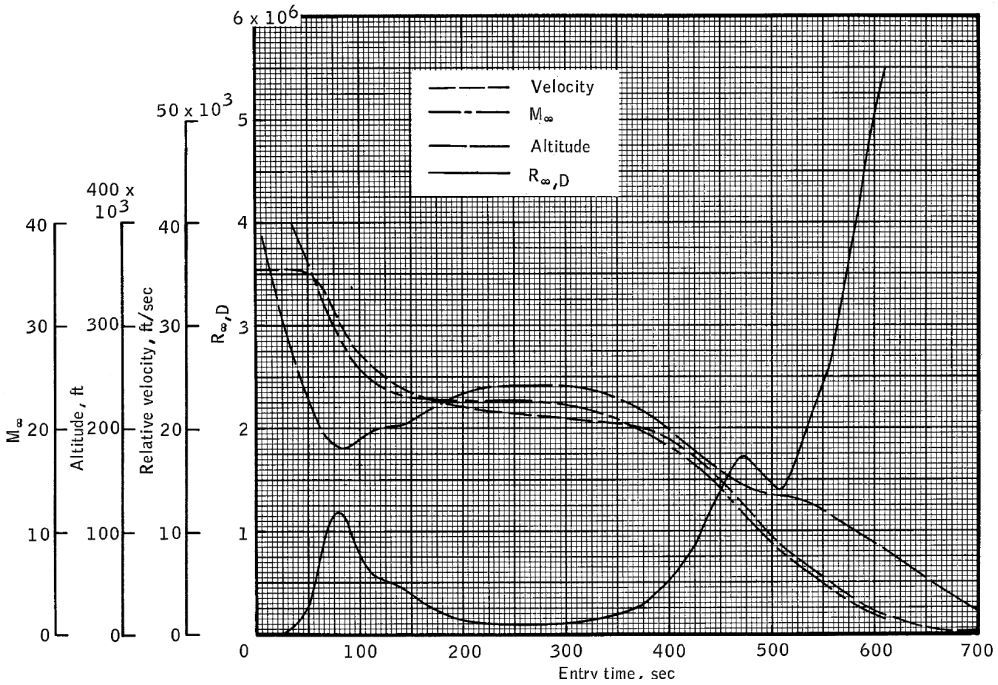

Figure 6.9. Apollo 4 Trajectory from Ref. [36].

To validate the convective heat flux, radiative heat flux, and the corresponding heat load values, results have been generated using the Apollo 4 trajectory shown in Figure 6.9. Apollo 4's maximum Mach number[7] during Earth entry was Mach 40, and because it had the highest entry velocity of all the Apollo missions, it also had the largest heat load. The total heat flux and heat loads are calculated using both Lovelace's Eqn. (4.9) and Tauber's Eqn. (4.10), and so Table 6.4 includes two columns of results. The equations used to produce each results are listed in the title of each column. These results are within 15% of the reported values.

Table 6.4. Apollo 4 Comparison of Total Heat Transfer.

Parameter	**Apollo 4, Ref. [38]**	**Results from [1.6*1.06*Eqn. (4.1)+Eqn. (4.9)]**	**Results from [1.6*1.06*Eqn. (4.1)+Eqn. (4.10)]**
$q_{max,tot}$ (W/cm^2)	483	542 (+12%)	469 (-2.9%)
$Q_{max,tot}$ (J/cm^2)	42600	46200 (+8.5%)	38700 (-9.2%)

NASA reported the values of the heat flux and heat load at the point of maximum heating, which in the case of the Apollo CM was not at the stagnation point. Although this work calculates the stagnation-point heating only as explained in Chapter 4, these reported values can still be used for validation. As shown in Figure 6.10, the maximum convective heating for the Apollo CM at α = -25^o was 60% larger than the stagnation-point convective heat flux at zero angle of attack.

Maximum heating is located at S/R = 0.9 while the stagnation point at α = -25^o is located at S/R = 0.74. Since the stagnation point at α = -25^o has a 10% higher heat flux than that at zero angle of attack, the maximum heat flux is 45% larger than the stagnation-point heat flux at α = -25^o. Although angle of attack has been

accounted for by this work's radiative heat flux calculations, it has been assumed that the convective heat flux would be kept constant at the nose.

Due to the Apollo CM's low spherical-segment angle of 25^o and corner geometry, the stagnation-point does not have the highest convective heat flux at $\alpha = 25^o$. Bertin[29] notes that a correction factor of 1.06 to the correlation for a sphere can be used to account for the change in the sonic line location from 45^o to approximately 25^o for the CM. As a result, after multiplying the convective heat flux by 1.06 and then 1.60 to account for the corner radius' effect that produces maximum heating, the convective heat flux can be added to the radiative heat flux to produce maximum heat flux and heat load results within 12% of the reported values.

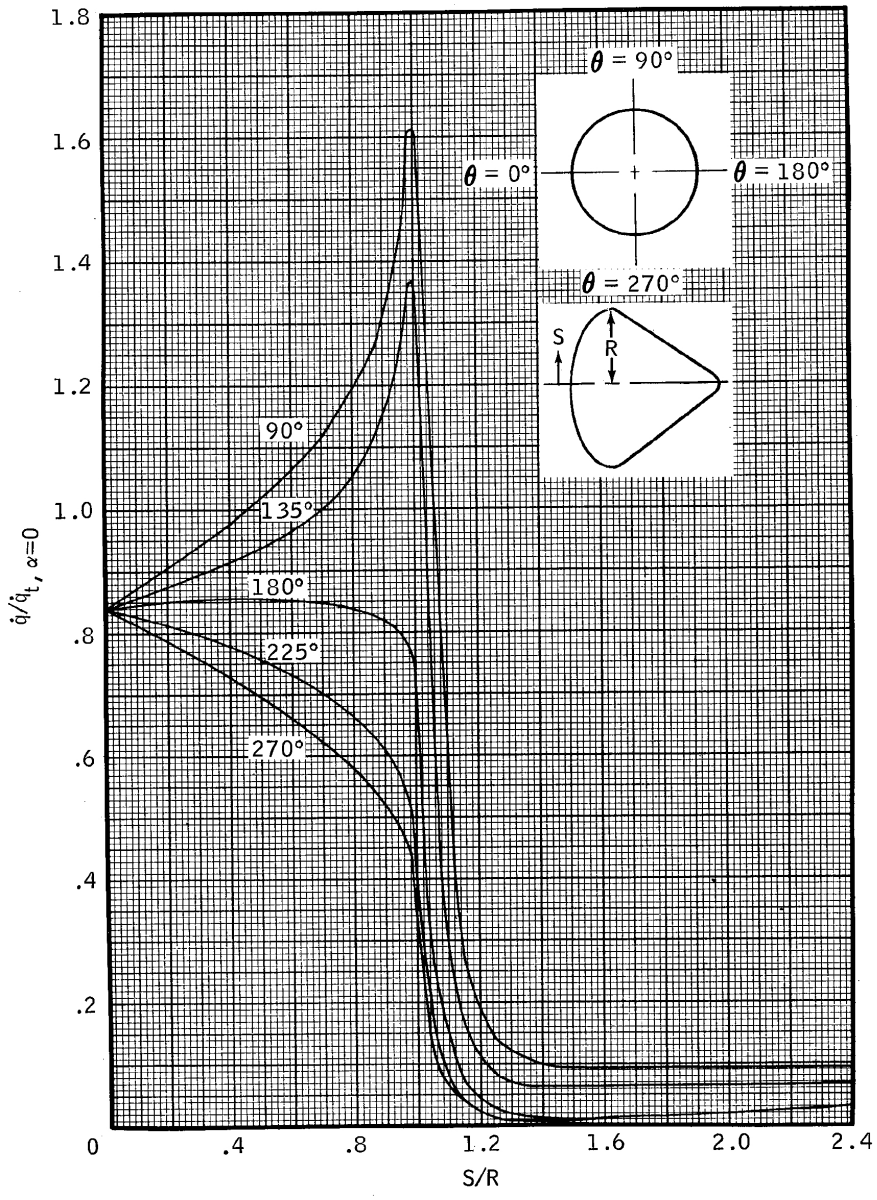

Figure 6.10. Convective heat flux distribution of Apollo Command Module at $\alpha = 25^{o}$ from Ref. [36].

6.2.2. FIRE II

In the case of the FIRE II flight, the entry vehicle's stagnation point was equal to the point of maximum heating, and it traveled mainly at zero angle of attack. As a result, it would be expected that this work would match the FIRE II data more closely than the Apollo 4 data. However, the FIRE II had an entry velocity of 11.4 km/s

(37400 ft/s), which is slightly faster than the entry velocity of Apollo 4 at 10.7 km/s. Because FIRE II had an entry Mach number greater than forty, it is possible for there to be coupled effects between convection and radiation that would reduce the total heat flux. The FIRE II had three heat shields of different radii placed on top of each other. One heat shield would be jettisoned at a time to acquire heat transfer data for each heat shield. Since the heat shields have different radii, discontinuities in the flight data are expected. As shown in Figure 6.11, flight data from the calorimeter produced a noticeably smaller heat flux value than the theory that does not assume coupling.

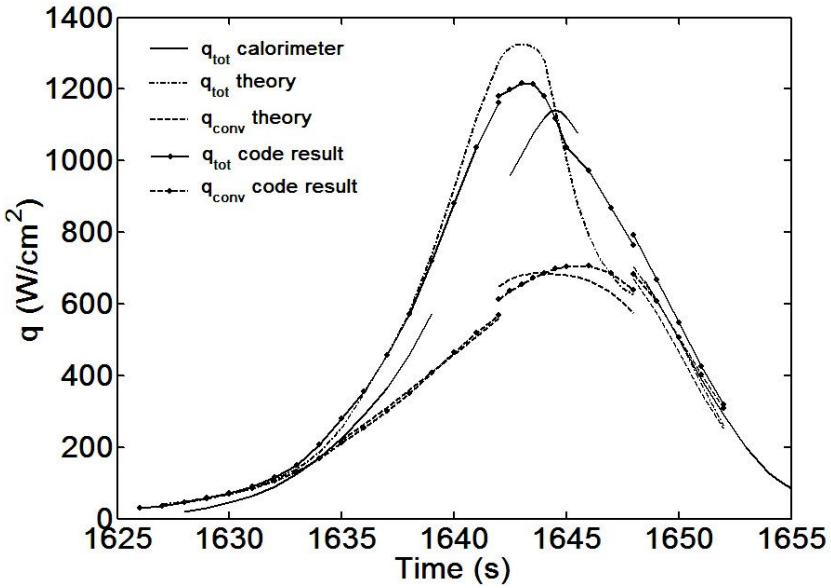

Figure 6.11. FIRE II Total heat flux comparison with flight data from Ref. [47].

The correlations of this work, which are labeled as code results, also do not assume coupling. The maximum total heat calculated by this work is 9% larger than the flight data. The interesting part is that the convective theory curve that assumes coupling and the code results nearly match perfectly for the first shield and do not vary greatly for the other two. However, it is apparent that the correlations fall approximately

halfway in-between the theory that assumes no coupling and the calorimeter data. It is believed that the FIRE II had some coupling, and that this is the reason why the total heat flux theory without coupling and the code results produce a peak at a different time than the FIRE II calorimeter data. As a result, it would be expected that this work's accuracy would begin to disappear at slightly higher velocities.

Chapter 7. Parametric Analysis

In order to become familiar with the design space that will be used in optimization, a parametric analysis has been conducted. Familiarity with the design space and previous work allows one to know whether optimization results are reasonable and provides simple test cases for verifying that the optimizer is working properly. Also, better initial designs for optimizing a given objective function may also be discovered throughout the parametric analysis. Most of this parametric analysis is included in Ref. [72].

7.1. Selecting a Superelliptical Base

Aerothermodynamic results were acquired for several axial and base shape combinations with the parameters in Table 2.1. One of the main considerations in choosing a polygon of *m*-sides is for it to be passively longitudinally stable over a range of cross-sections, and so one of the most longitudinally stable shapes is desirable. In order to compare the value of the pitching moment consistently throughout the given shapes, moments about the tip of the nose are considered. Moments about the shape's center of gravity are accounted for later in this analysis. The derivative of the pitching moment coefficient $C_{m,0,\alpha}$ shown in Figure 7.1 varies slightly with the rounded-edge concave *m*-gon compared to its variance with eccentricity. Because the hexagon has the most stable value for pitching and yawing moments, it was decided that a superellipse with $m = 6$ would be featured in this

analysis. The results in this section focus on heat shield geometries with the rounded-edge and concave hexagonal (m = 6) and elliptical cross-sections.

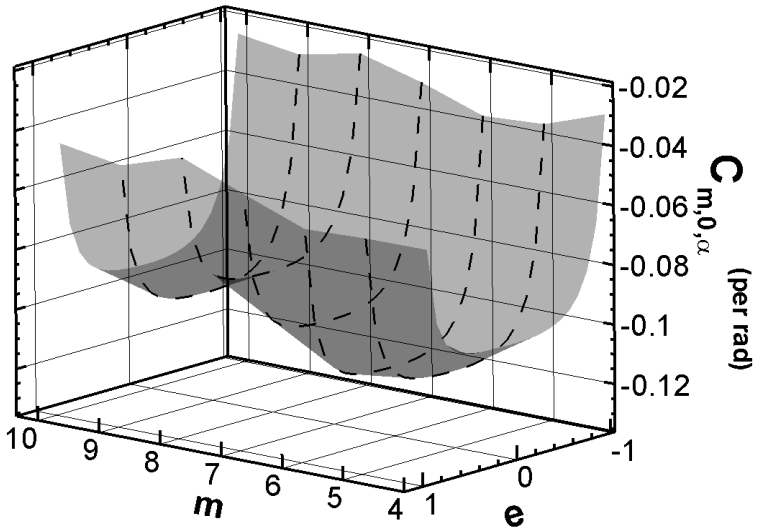

Figure 7.1. $C_{m,0,\alpha}$ distribution varying m-gon and e with spherical-segment axial shape and rounded-edge concave cross-sections, α=-20°, β = 5°.

The $C_{m,0,\alpha}$ distribution also suggests that eccentricity always decreases longitudinal static stability for the shapes considered. Positive values of the eccentricity correspond to the prolate shapes, and negative values to the oblate ones. A prolate eccentricity value of 0.5 was chosen as the constant eccentricity at which to present results because it does not considerably lower vehicle stability and since data on eccentric heat shields is scarce. Note that a particular oblate shape with a larger L/D but smaller C_L than the common non-eccentric spherical-segment will be discussed later in this analysis.

7.2. Heat Shield Shapes and Aerodynamic Performance

The results are acquired at M_∞ = 36, the re-entry Mach number from lunar return for the trajectory of the Apollo CM. The code was run over several ranges of geometric parameter values and angles-of-attack for each of the axial shapes and

cross-sections. The set of superelliptic bases included a rounded-edge hexagon, an ellipse, and a rounded-edge concave hexagon, each with an eccentricity of 0.5 as shown in Figure 7.2, along with examples of axial shapes.

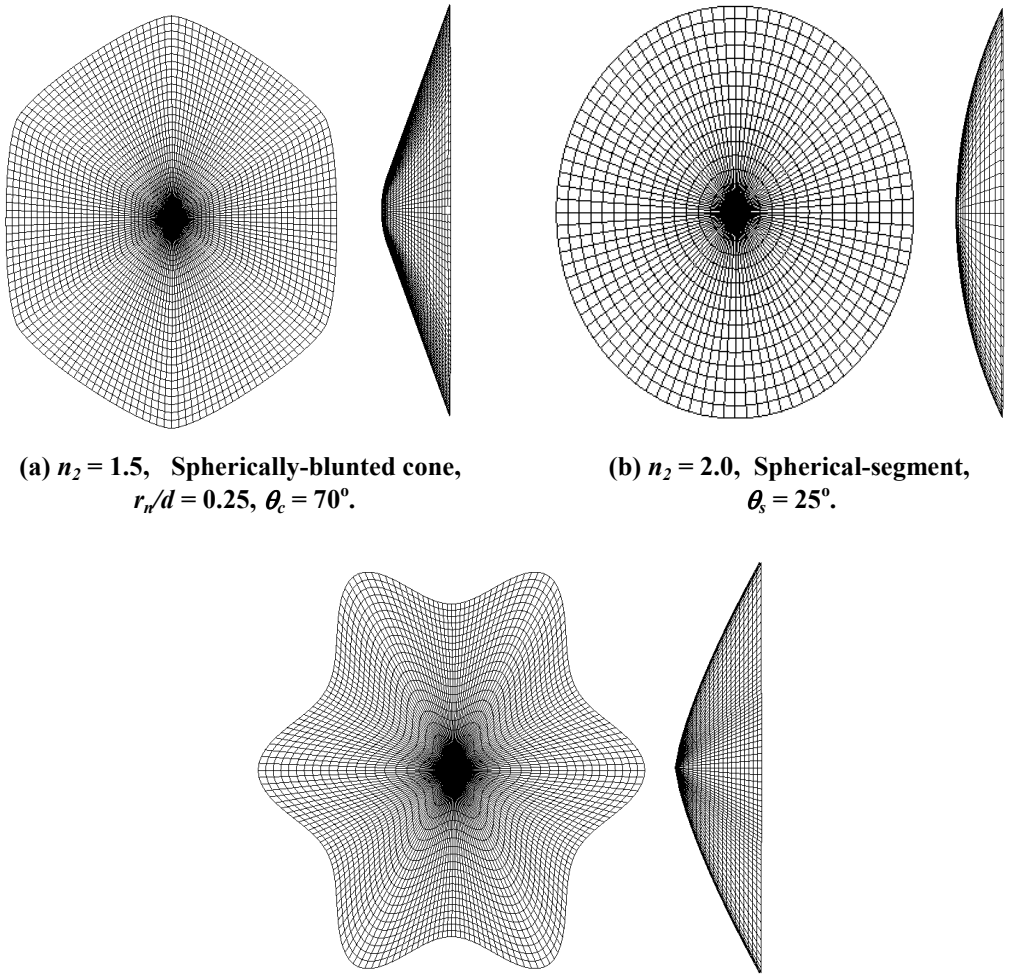

(a) n_2 = 1.5, Spherically-blunted cone, r_n/d = 0.25, θ_c = 70°.

(b) n_2 = 2.0, Spherical-segment, θ_s = 25°.

(c) n_2 = 4.0, Power law shape, A = 2, b = 0.75.

Figure 7.2. Chosen heat shield shapes for parametric analysis.

The ranges of the geometric variables for the axial shapes are included in Table 7.1; this table has ranges that are applied to most of the analysis, including the results in Table 7.2. The axial shapes shown in Figure 7.2 are those applied when varying α; of these three axial shapes, the one with the smallest geometric l/r is the spherical-segment, followed by the spherically-blunted cone, and then the power law shape.

As used in previous work, a sideslip angle of five degrees has been chosen in calculating the values of $C_{n,\beta}$ and $C_{l,\beta}$. Apollo 4 had a maximum sideslip of $\beta = 2^o$, but wind tunnel tests have tested the Aeroassist Flight Experiment[32,33] (AFE) at sideslip values up to $\beta = \pm 5^o$.[32] Note that it is convention to combine the three normal vectors C_A, C_N, and C_Y into two vectors C_L and C_D; this produces vertical and horizontal (with respect to the body axis) components of lift, represented by L_V and L_H respectively for cases with $\beta \neq 0$.[20,21] Even though L_H is negligible in this particular analysis since β is small compared to α, L_V is listed in results with $\beta \neq 0$ in order to be consistent with general theory.

Table 7.1. Variable ranges and constants for each axial shape.

Axial Shape	Variable Range	Constants
Spherical-segment	$-30^o \leq \alpha \leq 0^o$	$\theta_s = 25^o$ (Apollo Command Module)
	$5^o \leq \theta_s \leq 90^o$	$\alpha = -20^o$
Spherically-blunted Cone	$-30^o \leq \alpha \leq 0^o$	$\theta_c = 70^o$, $r_n/d = 0.25$ (Viking Mars Lander)
	$30^o \leq \theta_c \leq 89^o$	$\alpha = -20^o$, $r_n/d = 0.25$
	$0.01 \leq r_n/d \leq 1.00$	$\alpha = -20^o$, $\theta_c = 70^o$
Power Law Shape	$-30^o \leq \alpha \leq 0^o$	$A = 2$, $b = 0.75$
	$1 \leq A \leq 6$	$\alpha = -20^o$, $b = 0.75$
	$0.1 \leq b \leq 0.999$	$\alpha = -20^o$, $A = 2$

The coordinate system shown in Figure 3.1(a) has the direction of positive sideslip and negative angle-of-attack. The direction of positive moments is shown in Figure 3.1(b) for both positive and negative L_V, which only changes the convention of the rolling moment for reasons explained in Chapter 3. Since blunt-bodies produce positive lift at negative angles-of-attack (for $\theta_c > 45^o$), this analysis mainly focuses on how geometric variables vary with a constant negative angle-of-attack. Since the

Apollo CM had trim angles of attack equal to -17.5° and -25.5° during orbital re-entry and lunar return respectively, the effects of the geometric parameters are analyzed at an angle of attack in-between them at -20°.

7.3. *Hypersonic Aerodynamic Performance and Stability*

The effects of the power law's slenderness ratio, A, and cross-section parameter, n_2, on $C_{m,0,\alpha}$ are shown in Figure 7.3. This plot is typical of the results for all of the aerodynamic parameters in that they are much more sensitive to a change in axial shape than to a change in cross-section. As a result, the effects of varying the cross-section at a fixed eccentricity are not usually as important compared to the effects of changing the axial shape for longitudinal static stability.

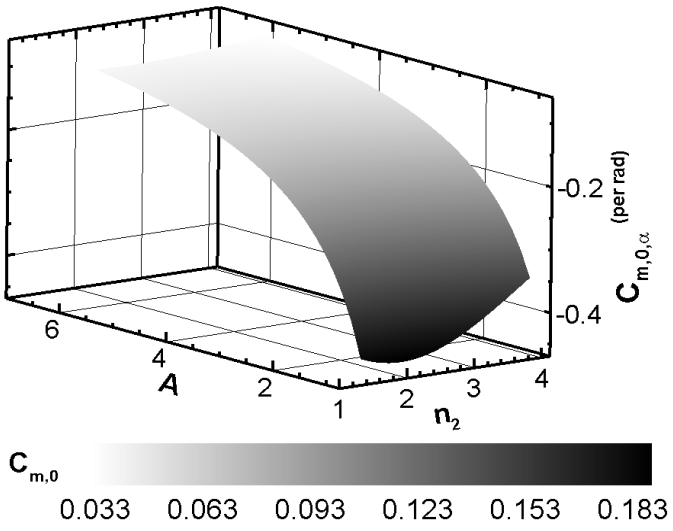

Figure 7.3. $C_{m,0,\alpha}$ distribution for power law A and n_2, b = 0.75, e = 0.5, α=-20°, β = 5°.

However, a cross-section's eccentricity can affect the vehicle's static roll stability significantly and is discussed later in this analysis. Figure 7.4 shows a similar trend for $C_{m,cg,\alpha}$ but also that there is a minimum of –0.22/rad near A = 1.5 and n_2 = 2. Both

$C_{m,0,\alpha}$ and $C_{m,cg,\alpha}$ have maximum absolute values at n_2 = 2, and this is also characteristic of the yawing moment stability derivative. The minimum $C_{m,cg,\alpha}$ may change in value and occur at a different (A, n_2) with a base of different eccentricity, or different values of b, α, or β. Because there are several combinations of variables that affect it, the process of optimization, which can vary any or all of the variables, will be an effective tool for locating extrema.

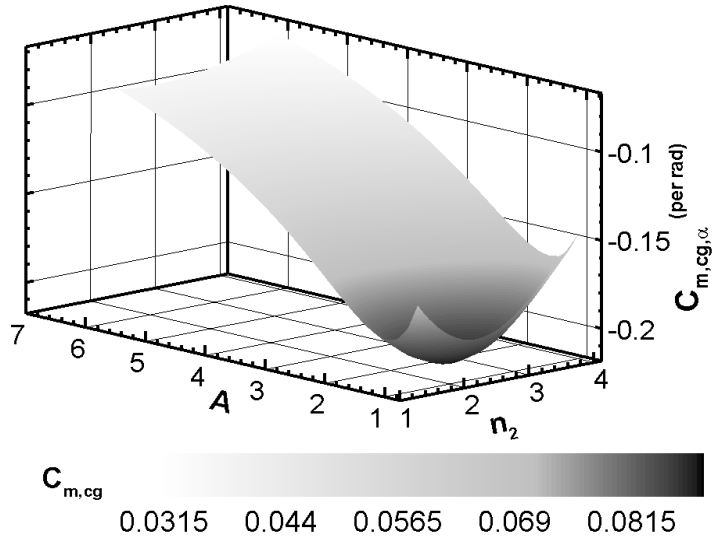

Figure 7.4. $C_{m,cg,\alpha}$ distribution for power law A and n_2, b = 0.75, e = 0.5, α=-20°, β = 5°.

Table 7.2 offers a summary of the sensitivity of main aerodynamic parameters (no heat transfer) by arranging the values of percentage difference of the parameter's minimum and maximum into six groups, labeled 0 through 5, in which coefficients in category five have the largest percentage difference. Each group corresponds to a range of percent difference values. Since the aerodynamic parameters do not vary considerably with a change in cross-section, as discussed earlier and shown in Figure 7.3 and Figure 7.4, the percentage differences as well as the actual values are close to each other and the same in sign when varying the cross-section. As a result, Table 7.2

includes one column of data for the set of three base cases instead of three separate columns.

Table 7.2. Effects of geometric parameters and α on aerodynamic performance.

	Spherical Segment		Spherically-blunted Cone			Power Law Shape		
	α	θ_s	α	θ_c	r_n/d	α	A	b
$C_{L,V}$	5	5	5	4	1	5	5	4
L_V/D	5	5	5	3	0	5	4	3
C_m	5	5	5	5	0	5	4	1
$C_{m,\alpha}$	2	5	2	3	0	2	3	1
C_n	1	5	2	5	0	1	4	1
$C_{n,\beta}$	1	5	1	5	0	1	4	1
C_l	1	5	1	5	0	3	5	1
$C_{l,\beta}$	0	5	0	5	0	4	5	5
X_{cp}/l	0	2	0	1	1	0	3	2
Y_{cp}/l	5	3	5	1	1	5	2	1
Z_{cp}/l	0	2	1	1	1	0	1	1
η_v	N	4	N	4	1	N	3	1

Note: Ranges of α, θ_s, θ_c, r_n/d, A, b given in Table 7.1.

Percent Difference Key
0: < 14%
1: 15% - 39%
2: 40% - 75%
3: 76% - 400%
4: 401% - 999%
5: 1000% +
N: Not applicable.

Of the three moment coefficients, only C_m varies over two orders of magnitude with α while $C_{m,\alpha}$ only varies by approximately 50%. C_m also varies in two orders of magnitude with α, θ_s, θ_c, and A. In general, the moment coefficients and stability derivatives varied strongly with θ_s, θ_c, and A for the given range. For the

spherically-blunted cone, r_n/d only had a small effect, by varying the aerodynamic parameters ≈ 5-10% at most. The exponent b for the power law shape varied them ≈ 25% except for $C_{l,\beta}$ that was affected strongly, although this does not necessarily mean that an extremely high value of $C_{l,\beta}$ was acquired; it only means that it varied strongly with b from a possibly negligible to significant value. As a result, a high percentage does not necessarily mean varying strongly from one significant value to another one, and some high percentages were produced since the smaller of the two absolute values was near zero ($<10^{-5}$). In the least, these results can be compared to more advanced analyses in future investigations.

A human planetary entry vehicle may require a reaction control system (RCS) to control the roll angle for human safety and follow the entry trajectory. If the rolling moment stability derivative is unstable but small, a less powerful rolling moment control system would be needed. Also, the units of the stability derivatives are per radian rather than per degree, and so reasonable rolling moment derivative and yawing moment derivative values from the AFE include $C_{l,\beta}$=-0.04584/rad = -0.0008/^{o} and $C_{n,\beta}$ = 0.1318/rad = 0.002300/^{o}.[21] The AFE has a circular cross-section with a blunted-nose, raked-cone axial shape that produces values of $C_{l,\beta}$ that are within the range of values acquired in this analysis, and the AFE's values of $C_{n,\beta}$ are within the mid-range of values acquired in this analysis.

Moment coefficients and stability derivatives shown in Figure 7.5 at α = -20^o, β = 5^o, are affected strongly by varying the geometric parameters. Although the magnitudes are not equal, the plot of $C_{m,\alpha}$ in Figure 7.5(b) would show the same behavior as that of C_m in Figure 7.5(a) if the data were reflected about the horizontal

axis. Figure 7.5(c) and (d) show C_n and $C_{n,\beta}$ have the same behavior, although C_n is an order of magnitude smaller.

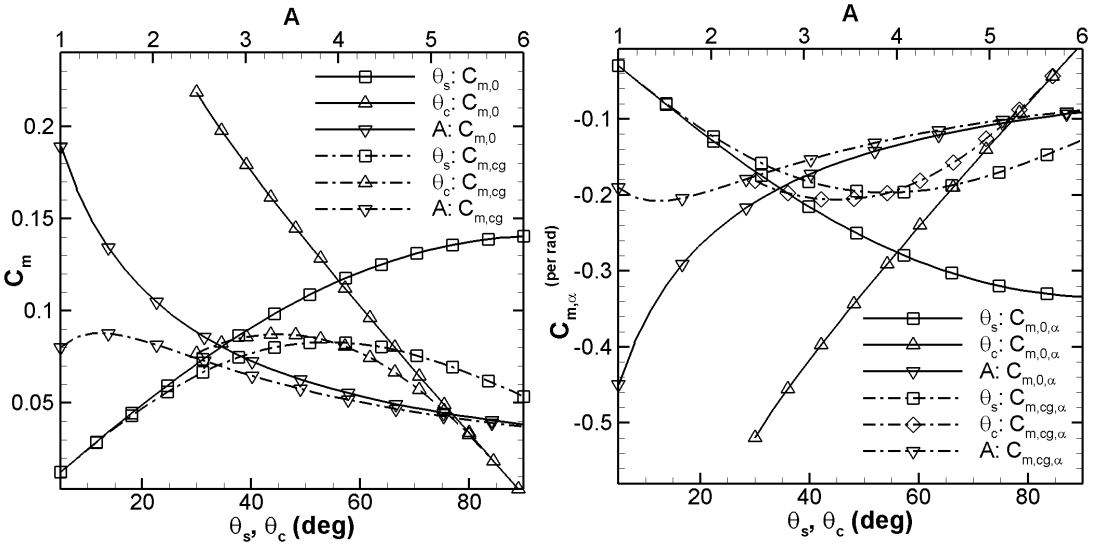

a) Variations in C_m. **b) Variations in $C_{m,\alpha}$.**

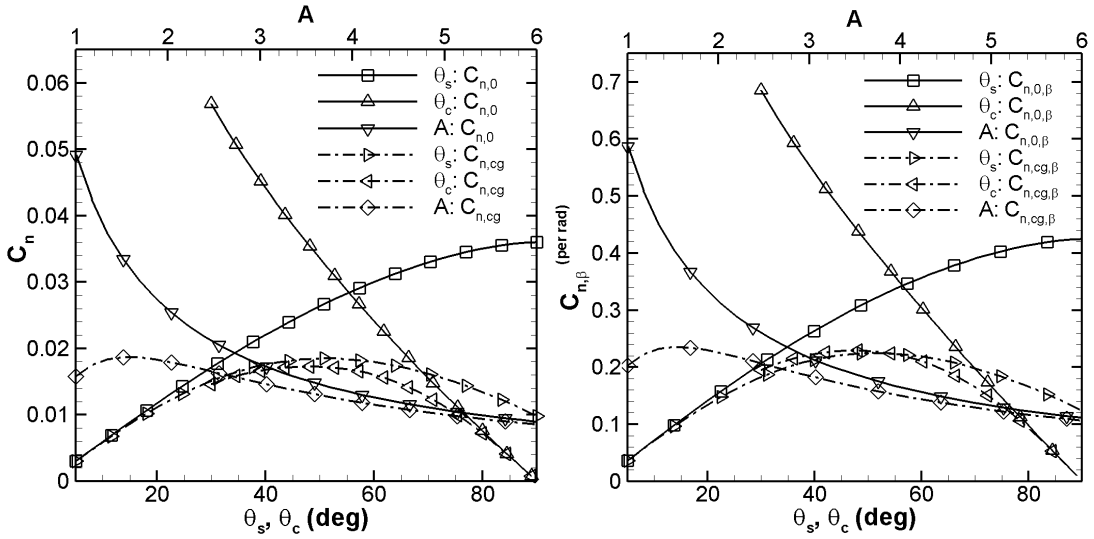

c) Variations in C_n. **d) Variations in $C_{n,\beta}$.**

Figure 7.5. Effects of θ_s, θ_c (r_n/d = 0.25), A (b = 0.75) on stability coefficients and derivatives, α = -20°, β = 5°.

All four variables show that the center of gravity moments and derivatives first increase in magnitude with an increase in the geometric parameter, then produces a minimum or maximum, and then decreases in magnitude, which is a different behavior from that of the moments about the nose that usually have maximum and

minimum values near or at the end points of the range. As a result, it is important to note that the values of the moments about the nose may neither be near the values of the moments about the center of gravity nor share the same behavior. It is noticed that $C_{m,cg}$, $C_{m,cg,\alpha}$, $C_{n,cg}$, and $C_{n,cg,\beta}$ all have maximum magnitudes near the same value, suggesting that a value of –0.22/rad for $C_{m,cg,\alpha}$ for a power law shape with A = 1.5 would also be produced with both a spherically-blunted cone of θ_c = 42.5° and a spherical-segment of θ_s = 52.5°. Heat shields with equivalent values of $C_{n,cg,\beta}$, which has a maximum magnitude of 0.24/rad, can also be determined. Both the C_l and $C_{l,\beta}$ have values within those acquired in wind tunnel for the AFE that are of the order of 0.01/rad for $C_{l,\beta}$ and 0.001 for C_l.[21]

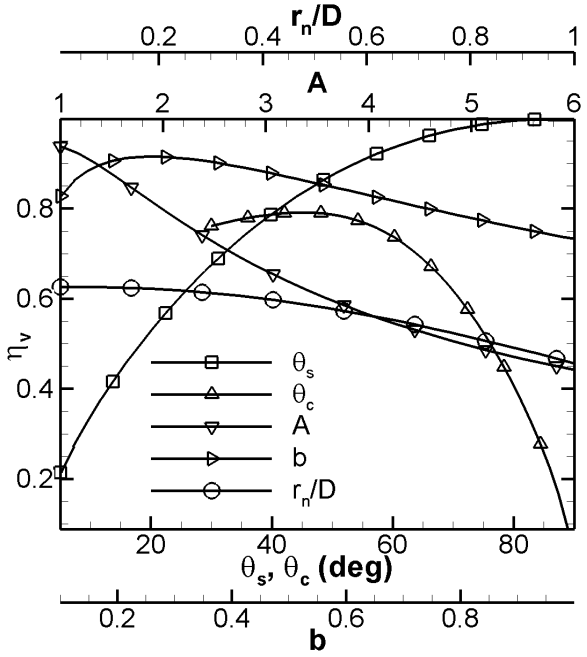

Figure 7.6. Effects of θ_s, θ_c (r_n/d = 0.25), A (b = 0.75), and b (A = 2) on η_v, α = -20°, β = 5°.

Figure 7.6 shows how all five geometric variables affect the volumetric efficiency of the heat shields. The volumetric efficiency in this case is normalized to a

hemisphere in Eqn. (2.15), and this results in the most volumetrically efficient shape being the non-eccentric spherical-segment at θ_s = 90°. The volumetric efficiency is varied with eccentricity and θ_s for a range of spherical-segments in Figure 7.7.

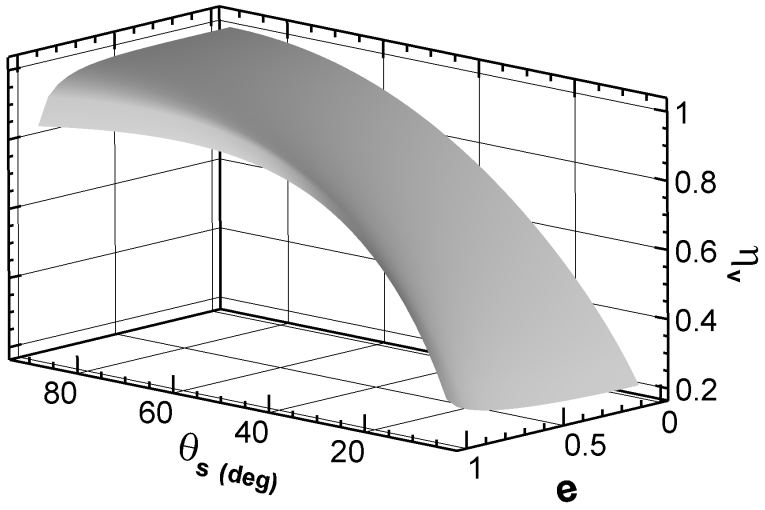

Figure 7.7. η_v distribution for spherical-segment, elliptical base (n_2 = 2), varying e and θ_s.

For θ_s = 90°, an increase in eccentricity decreases the volumetric efficiency, but a saddle point exists at θ_s = 35°; as a result, below θ_s = 35° eccentricity increases the volumetric efficiency by up to 10%.

7.4. Effect of Eccentricity on Aerodynamic Performance

The stability derivative of the rolling moment about the center of gravity, in Figure 7.8 does not become significantly affected by eccentricity until θ_s > 20°. Beyond this value of θ_s, it is observed that the magnitude of $C_{l,cg,\beta}$ increases. For clarity purposes, the stable configurations are shown as $C_{l,cg,\beta} \leq 0$ in Figure 7.8. While some of the oblate shapes are stable or unstable, the non-eccentric and prolate shapes (e > 0) are statically roll stable.

An analysis of the effect of eccentricity on L_V/D was conducted to determine if there were any possible shapes that were not completely stable but could give a noticeable increase in L_V/D. Figure 7.9 shows the L_V/D distribution for varying θ_s and eccentricity.

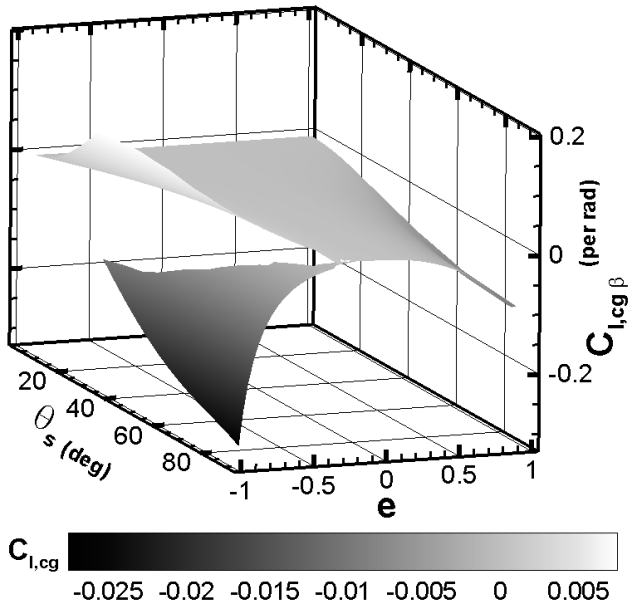

Figure 7.8. $C_{l,cg,\beta}$ distribution for spherical-segment, elliptical base (n_2 = 2), varying e and θ_s, α = 20°, β = 5°.

Shown in Figure 7.10, a positive α dataset produced the positive L_V/D value of 0.584, a 56.1% increase, at $\theta_s = 90^o$ for an oblate shape with e = -0.95, in which b_1 = 1.0 and a_1 = 0.311 at $\alpha = 20^o$ compared to a less round, more blunt $\theta_s = 5^o$ with e = 0.0 with a positive L_V/D value of 0.374 at $\alpha = -20^o$. However, $C_{L,V}$ drops to 0.282 from 0.56, a 49.6% decrease.

Table 7.3 lists the aerodynamic and stability characteristics based on modified Newtonian flow and uniform density heat shield geometries. The characteristics of the following geometries are listed in Table 7.3: $\theta_s = 5^o$ & e=0.0, $\theta_s = 25^o$ & e = 0.0 (similar to the Apollo CM heat shield), and $\theta_s = 90^o$ & e = -0.95. All three have stable

yawing moments also, with $\theta_s = 25^o$, $e = 0.0$ at the largest value of 0.0138 for $C_{n,cg}$, and the other two have smaller yawing moment coefficients on the order of 0.003.

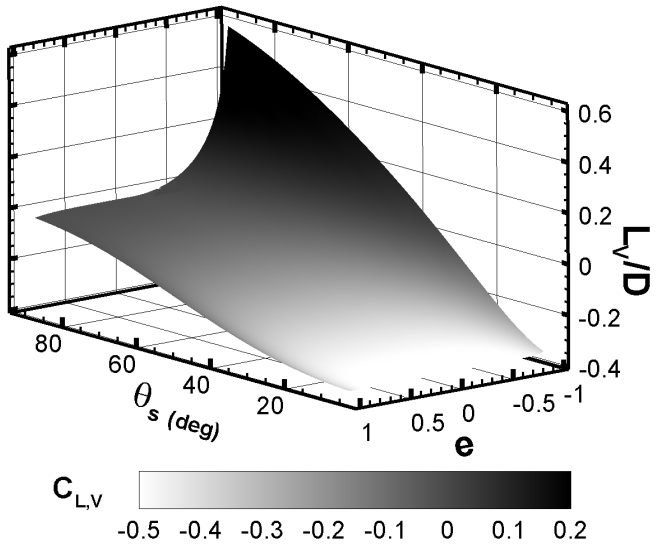

Figure 7.9. L_V/D distribution for spherical-segment: elliptical base ($n_2 = 2$), varying e and θ_s, $\alpha = 20^o$, $\beta = 5^o$.

While the yawing moment derivative $C_{l,0,\beta}$ for $\theta_s = 5^o$ & $e = 0.0$ is only 27.7% of the $C_{l,0,\beta}$ for the AFE, both the oblate $\theta_s = 90^o$, $e = -0.95$ and non-eccentric $\theta_s = 25^o$ have values of the same order as the AFE's. The rolling moment derivative about the center of gravity for $\theta_s = 5^o$, $e = 0.0$ is negligible, but the oblate $\theta_s = 90^o$, $e = -0.95$ has a $C_{l,0,\beta} = -0.0924$ that is twice the stability derivative of the AFE. The volumetric efficiency is lower for the blunt shapes $\theta_s = 5^o$ and $\theta_s = 25^o$ with values of 0.204 and 0.583 respectively compared to a value of 0.922 for $\theta_s = 90^o$, $e = -0.95$. The two non-eccentric cases have stable pitching moments.

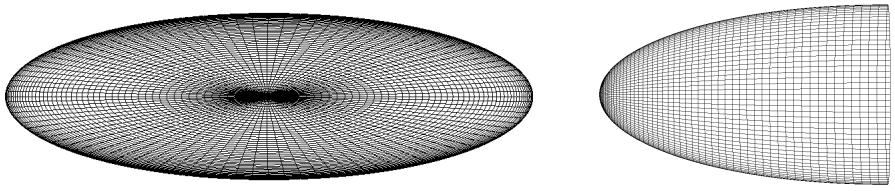

a) Front view. **b) Side view.**

Figure 7.10. Spherical-segment $\theta_s = 90^o$, $e = -0.95$ with an increase of 56% in L_V/D.

Table 7.3 Aerodynamic comparison of spherical-segments ($\beta = 5^o$).

	$e = 0$, $n_2 = 2$		$e = -0.95$ $n_2 = 2$
	$\theta_s = 5^o$ $\alpha = -20^o$	$\theta_s = 25^o$ $\alpha = -20^o$	$\theta_s = 90^o$ $\alpha = 20^o$
$C_{L,V}$	0.560	0.468	0.282
L_V/D	0.374	0.335	0.584
$(L_V/D)_\alpha$	-1.10	-0.961	0.469
$C_{m,0}$	0.0126	0.0613	-0.105
$C_{m,0,\alpha}$	-0.0299	-0.145	-0.363
$C_{n,0}$	0.00302	0.0147	0.0133
$C_{n,0,\beta}$	0.0365	0.177	0.161
$C_{l,0}$	0.000	-3.38E-5	-0.00808
$C_{l,0,\beta}$	—	-4.06E-5	-0.0924
$C_{m,cg}$	0.0126	0.0575	-0.0195 (0.0310)
$C_{m,cg,\alpha}$(/rad)	-0.0299	-0.136	-0.0990 (0.0566)
$C_{n,cg}$	0.00301	0.0138	0.00785 (0.00488)
$C_{n,cg,\beta}$(/rad)	0.0364	0.166	0.0916 (0.0541)
$C_{l,cg}$	0.000	-3.38E-5	-0.00808 (-0.00808)
$C_{l,cg,\beta}$(/rad)	—	-4.06E-5	-0.0924 (-0.0924)
X_{cg}/l	0.663	0.662	0.400 (0.635)
η_v	0.204	0.583	0.922

With the high eccentricity of e = -0.95 comes the unstable pitching moment derivative $C_{m,cg,\alpha}$ = 0.0566/rad if a uniform density heat shield is assumed. However, if the uniform density value X_{cg}/l = 0.635 is switched to X_{cg}/l = 0.400, then the pitching moment becomes stable with $C_{m,cg,\alpha}$ = -0.099/rad. In addition to values of aerodynamic moments at X_{cg}/l = 0.400, Table 7.3 includes moment and derivative values for this geometry with X_{cg}/l = 0.635 in parentheses. As a result, it may be advantageous to further study oblate geometries that produce higher L_V/D since an

increase in trim L_V/D opens a larger range of entry flight path angles available for planetary entry and significantly increases the range capability of the space capsule.[1]

7.5. Comparison of Aerothermodynamic Performance on Two Heat Shields

After conducting the optimization cases discussed in the next chapter, it was determined that a heat shield with a parallelogram cross-section (m = 4) produces a higher L/D than one with a hexagonal cross-section. As a result, a brief parametric comparison of the m = 6 and the m = 4 shapes based on stagnation-point heating and L/D is conducted. This is completed with a spherically-blunted cone axial shape with a 55° half-cone angle and r_n/d = 0.05 at α = -20°. As noted in the next chapter, the minimum r_n/d for this work is 0.05, and the minimum half-cone angle is 55°; this parametric study attempts to show some of the effects of one of the expected worst cases from a stagnation-point heating approach.

The total stagnation-point heating varies with n_2 and e for m = 6 in Figure 7.11(a). Since the method of determining the shock-standoff distance is a piecewise, the plot of $\dot{q}_{s,tot}$ is expected to have discontinuous slopes. This ripple effect is more pronounced in Figure 7.11(b) for m = 4. From an optimization standpoint, this indicates that the optimizer will have to run numerous sets of initial designs to find a set of local minima that may exist in-between the ripples and then determine the global minimum. Note that in these cases, the r_n/d solely determines the convective heat transfer while r_{eff} and α determine the radiative heat transfer. As a result, the values for the convective heat transfer are constant for Figure 7.11(a) and (b) at 961 W/cm^2. Since the convective heat transfer correlations are accepted as reasonably

accurate and since radiation is a current line of research, only the radiative heat transfer correlations were explored further.

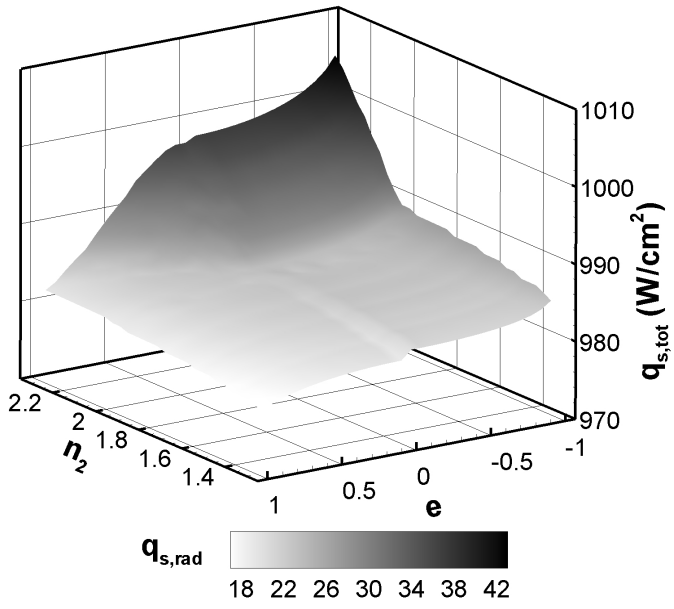

a) Hexagonal base (m = 6).

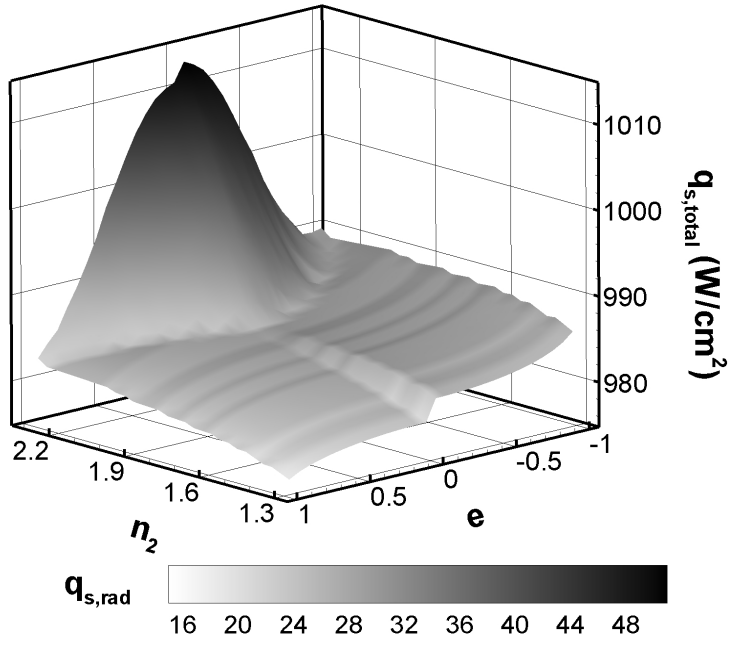

b) Parallelogram base (m = 4).

Figure 7.11. $\dot{q}_{s,tot}$ distributions for m = 4 and 6, spherically-blunted cone axial shape, $\theta_c = 55^o$, r_n/d =0.05, varying e and n_2 = 1.3 to 2.3, M_∞ = 32.8, $\alpha = -20^o$.

Each of these figures includes a drop of 1-5 W/cm^2 in at least the $n_2 < 2$ region, due to using a piecewise method. Since the drop is small compared to the magnitude of the total heat flux, it is not significant in this case. For additional plots, it is shown that this drop becomes larger but does not exceed 20% of the radiative heat flux.

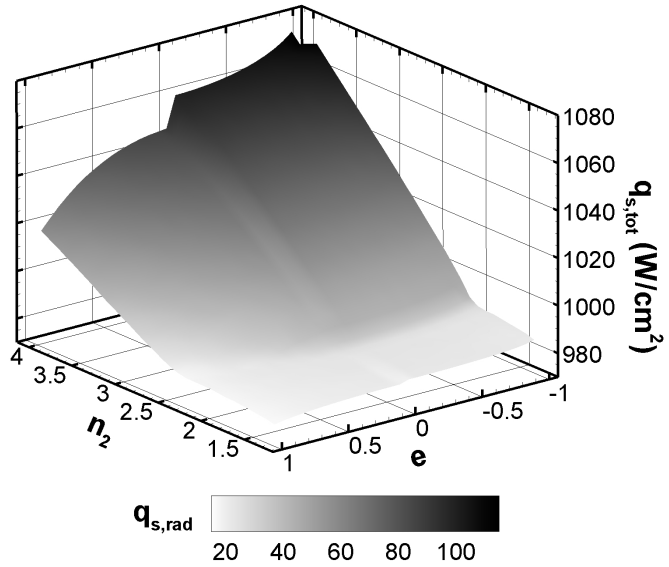

a) Hexagonal base (m = 6).

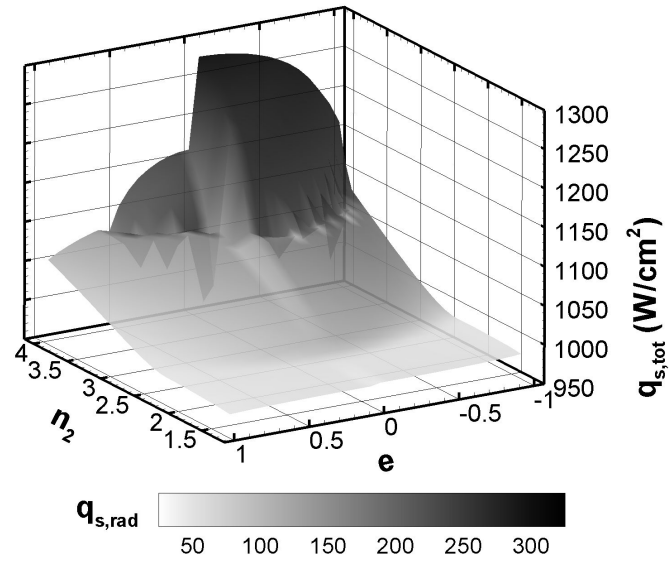

a) Parallelogram base (m = 4).

Figure 7.12. $\dot{q}_{s,tot}$ distributions for m = 4 and 6, spherically-blunted cone axial shape, θ_c = 55°, r_n/d =0.05, varying e and n_2 = 1.3 to 4.0, M_∞ = 32.8, α = -20°.

If the parametric analysis is furthered to n_2 = 4, then the $\dot{q}_{s,tot}$ varies for m = 6 in Figure 7.12(a) better than it does for m = 4 in Figure 7.12(b) since the method begins to break down around n_2 = 3 for the parallelogram. This breakdown is shown in Figure 7.12(b) with the troughs that are seen through the main slope. This is not present in the hexagonal cross-sectional case.

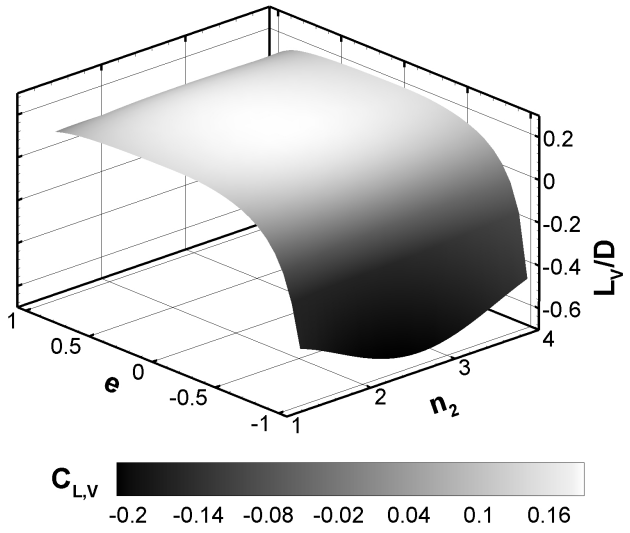

a) Hexagonal base (m = 6).

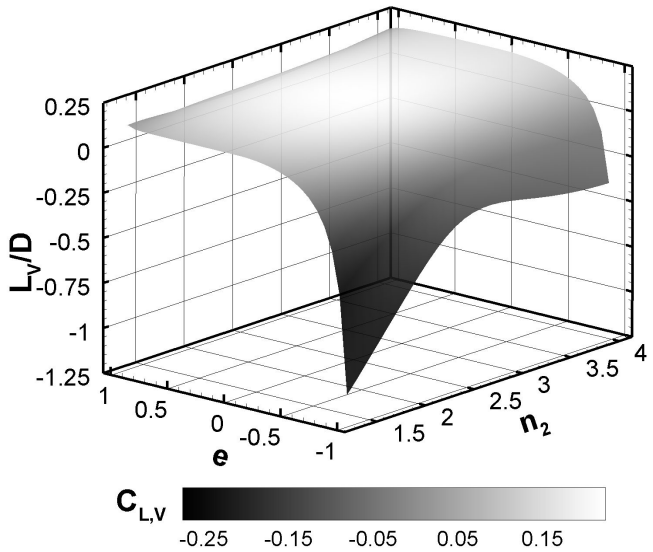

a) Parallelogram base (m = 4).

Figure 7.13. L_V/D distribution for m = 4 and 6, spherically-blunted cone axial shape, θ_c = 55°, r_n/d =0.05, varying e and n_2 = 1.3 to 4.0, M_∞ = 32.8, α = -20°.

L_V/D is shown to have a maximum magnitude of 0.61 with an oblate, rounded-edge concave hexagon in Figure 7.13(a). In this case the value is negative, which means that the hexagonal shape could produce a positive L_V/D of equal magnitude at positive angle of attack since it is symmetric about the horizontal axis (z-axis). The main result found through optimization is that the magnitude of L_V/D as shown in Figure 7.13(b) could be increased past 1.0 for the oblate rounded-edge parallelogram.

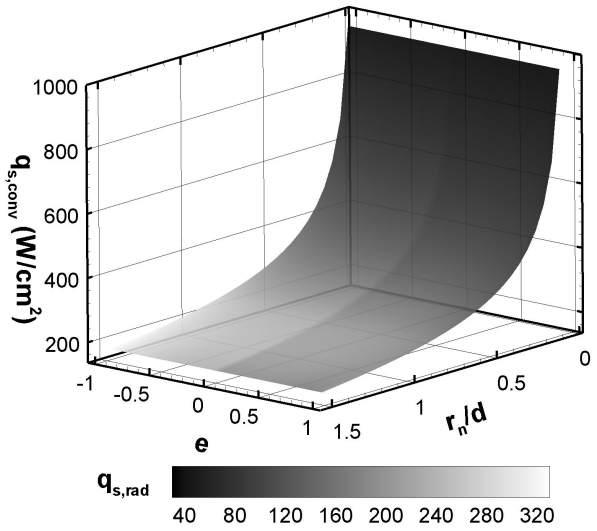

a) $\dot{q}_{s,conv}$ **distribution.**

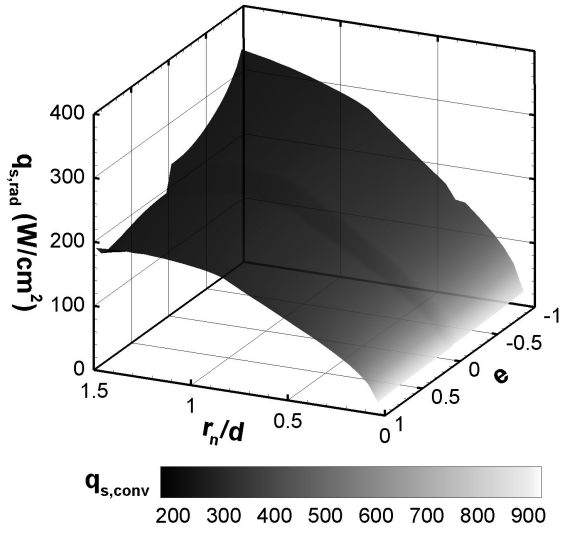

b) $\dot{q}_{s,rad}$ **distribution.**

Figure 7.14. $\dot{q}_{s,conv}$ **and** $\dot{q}_{s,rad}$ **distributions for parallelogram base (*m* = 4, n_2 = 1.4), spherically-blunted cone axial shape, $\theta_c = 55^o$, varying *e* and r_n/d, $M_\infty = 32.8$, $\alpha = -20^o$.**

For m = 4, the variation in convective heat flux with eccentricity and r_n/d is included in Figure 7.14(a). The eccentricity does not modify the nose radius dramatically, and so the convective heat flux does not vary with eccentricity. However, an increase in nose radius alleviates much of the convective heat flux. The radiative heat flux shown in Figure 7.14(b) shows the opposite trend: an increase in nose radius produces more radiative heat flux. However, the prolate cases show a maximum at r_n/d = 1.3 while the oblate cases continue to increase. Some uncertainty is present with these results since prolate and oblate heat transfer analyses have not been researched in-depth. This would be a good topic of future research. It is believed that the maximum heat flux of the oblate cases provides a conservative limit on the heat flux expected on an actual heat shield based on the way the eccentricity correction factor is applied in Eqns. (3.52) and (3.53).

The trade-off between convection and radiation produce a total heat flux that has a local minimum at r_n/d = 0.5 for e = -1 and r_n/d = 0.8 for e = 1, as shown in Figure 7.15(a). Figure 7.15(b) provides another view of the total heat flux for clarity. For r_n/d > 1, some of the oblate cases increase in total heat flux while all the other cases continue to decrease. However, even with this increase, the overall change in heat flux is small and suggests that heat shields at 200000 ft and Mach number 32.8 should either have an r_n/d between 0.5 and 0.8 or greater than 1. The Apollo CM's design had a r_n/d = 1.18 and thus is in the lower region of heat transfer shown in Figure 7.15(a). For an increase in freestream Mach number, the radiative heat transfer becomes greater, and the results of optimizing the total heat transfer throughout the Mach numbers is included in Chapter 8.

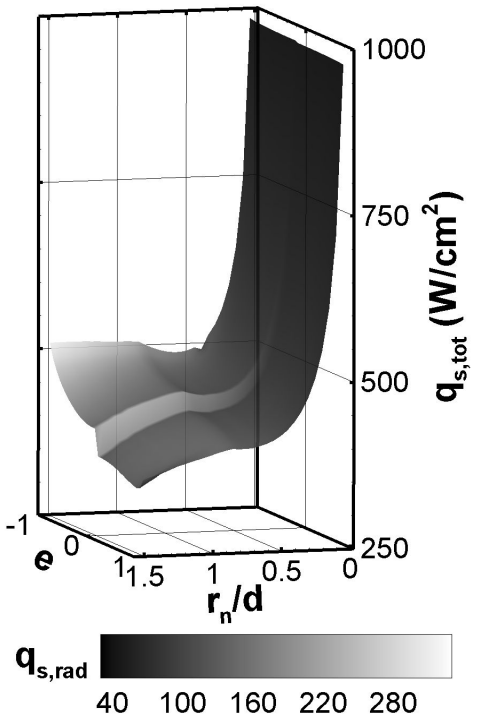

a) Emphasis on the local minima.

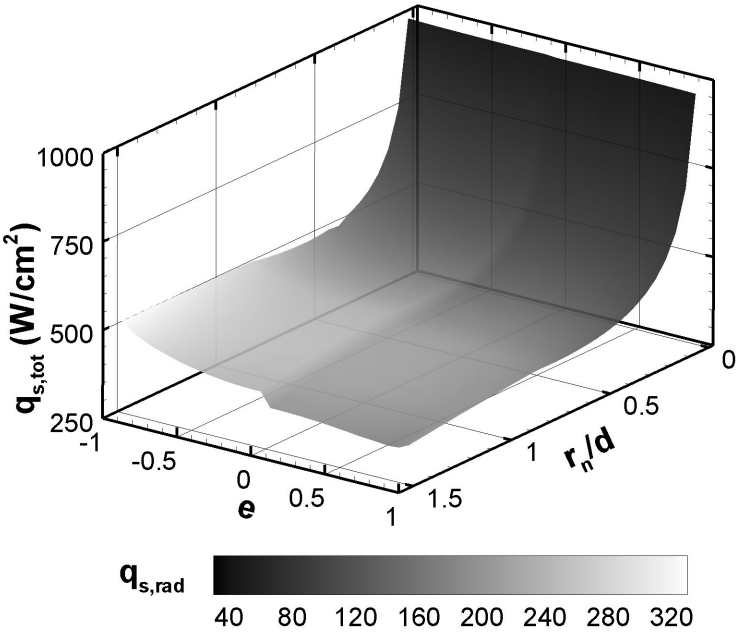

b) Emphasis on overall distribution.

Figure 7.15. $\dot{q}_{s,tot}$ **distribution for parallelogram base (*m* = 4, n_2 = 1.4), spherically-blunted cone axial shape, $\theta_c = 55^o$, varying *e* and r_n/d, $M_\infty = 32.8$, $\alpha = -20^o$.**

Chapter 8. Optimal Configurations

The optimization results of several objective functions are provided for the geometry whose axial shape produces the most ideal results. The main optimization results are provided as iteration histories of the objective function, design variables, and constraints, a 3D image, and a table of its aerothermodynamic characteristics. The iteration histories are located in the appendix. The objective functions in this analysis consist of maximizing L_V/D, $\eta_v(L_V/D)$, $L_V/D/\dot{q}_{s,tot}$, and of minimizing $\dot{q}_{s,tot}$ and $C_{m,cg,\alpha}$. A separate optimization is run for each of the three axial shapes, and this work provides iteration histories of the design variables in non-dimensionalized form so that all of them can be shown on the same figure. For each axial shape, the design variables with their lower and upper constraint values are given along with their non-dimensional value counterparts in Table 8.1. For the geometries with a spherical segment axial shape, the limit of 5^o on θ_s was chosen as the lower limit in order to provide a blunt-body that is not completely flat, and 89^o was chosen as an upper limit since the code would produce a zero in the denominator in some equations for $\underline{\theta_s} = 90^o$ and is a close approximation from a numerical standpoint.

The n_2 variable from Eqn. (2.8) controls whether the cross-section is a polygon, ellipse, or concave polygon. For this analysis, zero radius-of-curvature designs are not considered since they produce high heat concentrations. As a result, the n_2 lower limit of 1.3 produces slightly rounded-edge polygons. As n_2 approaches 2.0, the polygon transforms into an ellipse, and increasing n_2 further transforms the

ellipse into a rounded-edge concave polygon. An upper limit of 4.0 on n_2 generates shapes that still have a reasonable radius-of-curvature.

Table 8.1. Optimization design variables with side constraints.

Spherical Segment	
Dimensional	*Non-dimensional*
$5^o \le \theta_s \le 89^o$	$0.0556 \le \theta_s/90^o \le 0.989$
$1.3 \le n_2 \le 4.0$	$0.325 \le n_2/4 \le 1.0$
$-0.968246 \le e \le 0.968246$	$-0.968246 \le e \le 0.968246$
$-30^o \le \alpha \le 30^o$	$-1.0 \le \alpha/30^o \le 1.0$
Spherically-blunted Cone	
Dimensional	*Non-dimensional*
$55^o \le \theta_c \le 89^o$	$0.611 \le \theta_c/90^o \le 0.989$
$0.15 \le r_n/d \le 2.0$	$0.075 \le (r_n/d)/2 \le 1.0$
$-0.968246 \le e \le 0.968246$	$-0.968246 \le e \le 0.968246$
$1.3 \le n_2 \le 4.0$	$0.325 \le n_2/4 \le 1.0$
$-30^o \le \alpha \le 30^o$	$-1.0 \le \alpha/30^o \le 1.0$
Power law	
Dimensional	*Non-dimensional*
$0.2 \le b \le 0.9999$	$0.2 \le b \le 0.9999$
$0.9 \le A \le 10.0$	$0.09 \le A/10 \le 1.0$
$-0.968246 \le e \le 0.968246$	$-0.968246 \le e \le 0.968246$
$1.3 \le n_2 \le 4.0$	$0.325 \le n_2/4 \le 1.0$
$-30^o \le \alpha \le 30^o$	$-1.0 \le \alpha/30^o \le 1.0$

The eccentricity limits of ±0.968246 were chosen to limit the ratio of the semi-major axis' length to the semi-minor axis' to 4-to-1. This was decided from inspection, by what appeared to be a liberal choice of a reasonable shape by intuition.

The angle of attack is limited to ±30° since human space capsules usually enter at or below 25° and since the heat shield may be only half of the main vehicle's shape depending on the value of θ_s. If θ_s is large, then it is possible that the entire space capsule could fit within the heat shield or in the case of a ballute-type heat shield. These limits could be modified easily for future work.

A non-eccentric heat shield with $\theta_c \approx 45^o$ is the interface at which the spherically-blunted cone begins to produce positive L_V at negative α. If θ_c is less than this value, then negative L_V at negative α. The term blunt-body for re-entry usually insinuates that the vehicle produces positive L_V at negative α and that the shock-standoff distance is substantial. Since Ried[48] approximated that the shock-standoff distance of the Apollo 4 was 14 cm and this work predicts 12.4 cm (for t = 30030 s, M_∞ = 32.8, α = 25° at h = 200000 ft), it was decided that the order of accuracy of Kaattari's method is 2.54 cm. As a result, the spherically-blunted cone that has a shock-standoff distance of 2.54 cm would be designated as the lower limit for θ_c and r_n/d based on these method limitations. For a non-eccentric heat shield, this work predicts a 2.54 cm shock-standoff distance for a spherically blunted cone with θ_c = 55° and r_n/d = 0.25.

Although any solutions that suggest a shock-standoff distance around one to five inches should be reinvestigated, the lower limit on the nose radius-to-diameter ratio does not exceed 0.25 since previous work such as the Mars Viking missions included heat shields with r_n/d = 0.25. The chosen lower limit on r_n/d is 0.15 to widen the design space. For numerical reasons, θ_c is limited to 89° rather than 90°. The upper limit to r_n/d is set at two in order to include some shapes that are pure spherical-

segments; the Apollo Command Module can be approximated with θ_c = 75°, r_n/d =1.1831.

For the geometries with a power law axial shape, the lower limit value of b is 0.2 since it is both blunt and has a slope change in the shape that is less extreme than that for b = 0.1 or 0.01. Newtonian Impact Theory may have a problem with the quick slope changes shown in Figure 2.3 for b = 0.1 or smaller. The upper limit on b produces a nearly linear line, but the code requires the slope of the power law profile to vary at least slightly for numerical reasons. A value of b greater than one would produce concave axial shapes with infinitely sharp noses, which are not included in this analysis. Since previous work blunt-bodies usually have $l \ll d$ (i.e., Apollo CM $l/d \approx 1/9$), it was decided in this work to widen the design space by including $A = (l/d)^{-1} = (10/9)^{-1}$. Then the upper limit of A was decided to be ten since the power law shape loses most of its uniqueness at high A, in comparison with the cone or the spherical-segment axial shapes.

Note that although α is listed as one of the design variables, some of the objective functions may be optimized with fixed angle of attack (this is mentioned if applicable).

This optimization uses the following constraint vector, $\vec{G}$:

$$\vec{G} = \{G_1, \quad G_2, \quad G_3, \quad G_4, \quad G_5, \quad G_6\} \tag{8.1}$$

$$= \left\{ -1 + \frac{|\alpha|}{|\varepsilon + 1|}, \quad \frac{1}{100}\left(1 + \frac{C_{m,cg,\alpha}}{0.001}\right), \quad \frac{1}{100}\left(1 - \frac{C_{n,cg,\beta}}{0.001}\right), \quad \begin{matrix} -1 + \dfrac{C_{l,cg,\beta}}{0.01}, & C_{L,V} \geq 0, \\ -1 - \dfrac{C_{l,cg,\beta}}{0.01}, & C_{L,V} < 0, \end{matrix} \quad -1 + \frac{\dot{q}_{s,tot}}{3000}, \quad 1 - \frac{L/D}{0.30} \right\}.$$

G_1 is the only constraint on the geometry that is affected by freestream conditions. This constraint relates the angle of attack to the tangency angle ε, which is the angle

produced by the heat shield's edge surface and the vertical axis. Because the heat shield shape is not necessarily and not usually the entire vehicle shape, a limit on the angle of attack at which a given heat shield can be analyzed must be chosen in order to keep the assumption that the flow separates before passing over the crew compartment (aft body). This constraint basically requires that a given heat shield must not be placed at an angle of attack more than one degree larger than the tangency angle. In this way, the heat shield's edge is normal to the freestream flow when $\alpha = \varepsilon$. The one-degree above ε was chosen as a small relief factor.

G_2 and G_3 are longitudinal and yaw static stability requirements, respectively; because this is a numerical analysis, the magnitude value of 0.001 is deemed significant rather than 0.000. G_4 is the roll static stability requirement, but it is different from G_2 and G_3 in that it allows for a slight instability up to 0.01/rad in order to produce heat shields such as the Apollo CM, which was slightly unstable at 0.005/rad. This keeps the design space open to previous work. The requirement for roll static stability changes sign when the $C_{L,V}$ changes sign as explained in Chapter 3. G_5 is an upper limit constraint on $\dot{q}_{s,tot}$ of 3000 W/cm^2 and is three times the maximum heat flux of 1000 W/cm^2 at which NASA is designing the CEV. This allows for designs that will become feasible in the next couple decades. G_6 is a constraint on the lift-to-drag ratio that requires improvement over previous work. The Apollo CM had a lift-to-drag ratio of 0.34 during re-entry, which was used as the benchmark to improve upon in this work. Note that not all of these constraints are used in the following results. The constraints from vector $\vec{G}$ that are applied for each

optimization are noted for each optimization as well as the constraint iteration histories.

The design point conditions chosen for this analysis include an altitude of 200000 ft and Mach number M_∞ = 32.8. These were chosen because they are the conditions of Apollo 4 when it experienced the maximum total heat flux. Also, this is a point of high radiative heat flux, and for minimizing the stagnation-point heat transfer flux, the Mach number is increased to show how the optimum nose radius changes due to an increase in radiative heat flux. Although the aerodynamic performance and static stability characteristics can be given in non-dimensional terms, the heat transfer fluxes require the size of the heat shield to be chosen, and so the base diameter of 3.9166 m equal to that of the Apollo Command Module is prescribed. For some of the results, the center of gravity is chosen based on a uniform density distribution. However, after noticing from the parametric analysis that a longitudinally unstable heat shield could become stable by shifting the center of gravity forward a reasonable amount, it was decided that both cases would be tested. It is mentioned for each of the optimization results whether a uniform density distribution is assumed or a center of gravity location is prescribed. The prescribed center of gravity location for these results is equal to that of uniform density except that the prescribed X_{cg} is set to 75% of the uniform density value of X_{cg}. This allowed for a larger design space to be accessed.

This analysis is based on a total of 184 optimization runs, in which all of the initial designs of the design were varied significantly. Each optimization run has a different initial design. The number of sides of the superellipse cross-section has been

considered, and results between geometries with different cross-sections are compared. All three of the axial shapes have been considered, and the engineering global optimum is reported for each in the following sections.

8.1. Maximizing L_V/D and $\eta_V L_V/D$

The vertical lift-to-drag ratio by itself and the product of L_V/D and volumetric efficiency have been maximized. Since the parametric analysis originally encompassed only hexagonal superellipse cross-sections (m = 6), the optimization analysis began with m = 6. For the spherical-segment axial shape, it is shown in Table 8.2 that L_V/D generally increases with a decrease in the number of sides. The parallelogram cross-section has the minimum number of sides examined and thus offers the optimum lift-to-drag configurations in this analysis. The optimized m = 4, 5, and 6 shapes are shown in Figure 8.1.

Nineteen optimization runs of the spherical-segment, four of the spherically-blunted cone, and twenty-eight of the power law geometries were completed for maximizing L_V/D. Constraints G_1 through G_5 have been applied. The initial designs have values of n_2 usually equal to 1.6, 2.0, and 3.0. Ideally, the optimizer would be able to check if there is a local maximum near the 1.3 side constraint when starting from 1.6, in case the local maximum is overlooked when starting from the other two initial designs.

The spherical-segment angle constraint is active for these optimized shapes at $\theta_s = 89^o$. This high spherical-segment angle creates geometries that produce positive lift at positive angles of attack because the geometries have normal forces that

contribute more to the lift force than the axial force. In the classic case of the Apollo Command Module with $\theta_s = 25^o$, the axial force contributed more to the lift force, thereby making a negative angle of attack required for positive lift.

Table 8.2. Initial and Optimal Designs for maximizing L_V/D for different m.

Spherical Segment Axial Shape								
Initial Design				Optimal Design				Objective Functions
θ_s	n_2	e	α	θ_s	n_2	e	α	L_V/D
85^o	1.4	-0.9	25^o	89.0^o	1.3	-0.968	21.2^o	0.822 (m = 8)
85^o	1.4	-0.9	25^o	89.0^o	1.3	-0.968	19.8^o	0.755 (m = 7)
85^o	1.4	-0.9	25^o	89.0^o	2.61	-0.968	22.0^o	0.753 (m = 6)
85^o	1.4	-0.9	25^o	89.0^o	1.3	-0.968	24.1^o	0.878 (m = 5)
85^o	1.5	-0.9	25^o	89.0^o	1.3	-0.968	17.6^o	1.10 (m = 4)

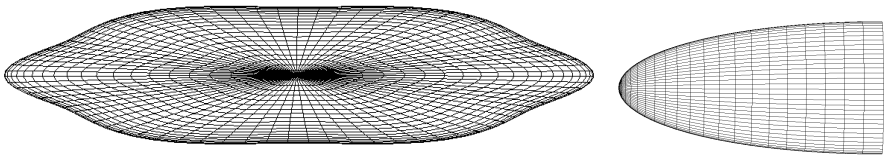

a) Hexagonal cross-section, L_V/D = 0.753.

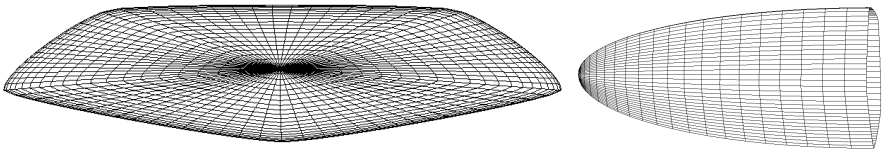

b) Pentagonal cross-section, L_V/D = 0.878.

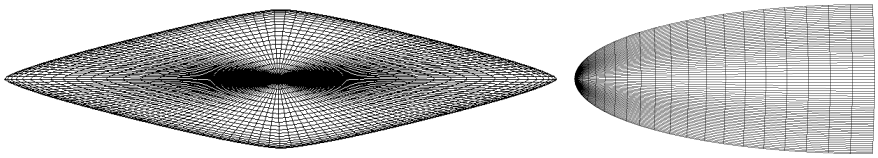

c) Parallelogram cross-section, L_V/D = 1.10.

Figure 8.1. Optimized geometries from Table 8.2.

The iteration histories of the objective function, design variables, and constraints are shown for the hexagonal cross-section spherical-segment geometry in

Figure A.0.1 in the appendix. The main increase in L_V/D occurs in the first iteration in which the geometry becomes more oblate and θ_s is increased to 89°, in which the minimum e and the maximum θ_s constraints become active, respectively. During the entire optimization, the G constraints are neither active nor violated. Because L_V/D is one of the most important aerodynamic characteristics of a lifting re-entry vehicle, and because a high L_V/D is desired for several reasons, such as increasing the range of available landing sites, the remainder of this optimization analysis is completed with parallelogram cross-sections ($m = 4$).

The spherically blunted cone with maximum L_V/D also has a four-sided cross-section, shown in Figure 8.2(a). Originally, the optimum was at $L_V/D = 1.14$, but the calculated shock-standoff distance was 2 cm, which is smaller than the estimated error of 2.54 cm. As a result, the side constraints on the spherical-segment angle and the nose-radius-to-diameter ratio were increased to 59° and 0.15 from 55° and 0.10 respectively. As a result, the calculated shock-standoff distance became 3 cm with $L_V/D = 0.95$. However, the shock-standoff distance of the optimum spherical-segment is 11 cm. This means that the spherical-segment shock-standoff distance is probably more reliable than the 3 cm calculation and may make the spherical-segment option a more desirable configuration.

A total of seventy-two function evaluations of the power law geometry were completed over seven iterations to find a maximum L_V/D of 2.10. The optimum power law geometry has a significant increase in heat transfer flux over the other two geometries, and also has heat flux constraint G_5 active. The power law shape is allowed to have radii as small as 0.001 m while the spherically-blunted cone is

restricted to 0.587 m due to limitations in calculating the shock-standoff distance. As a result, only the power law shape can produce 1000+ W/cm^2 fluxes in this work at the given design point using the variable limits listed in Table 8.1. The increase in L_V/D is based on the different curvature that is offered by the power law compared to the spherically-blunted cone and the spherical-segment. The iteration histories of the power law geometry are included in Figure A.0.2 and show that all of the design variables except for coefficient A are modified significantly.

Three optimization runs of the spherical-segment, two of the spherically-blunted cone, and eleven of the power law geometries were completed for maximizing $\eta_V L_V/D$. Fewer optimization runs were seen as necessary since the initial designs for maximum L_V/D had already been located. The calculated aerothermodynamic characteristics of the best configurations for each of the three axial shapes is shown for both objective functions in Table 8.3. Note that the initial designs for each optimization are written in the last lines of each table. The final results for the spherical-segment did not change between the two objective functions and has the highest L_V/D equal to 1.10. Although the same is true for the power law axial shape, different local minima exist for the two objective functions, and so a different initial design for maximizing $\eta_V L_V/D$ was required to find the same minimum. The spherical-segment has the smallest total heat flux, followed by the spherically-blunted cone that is 14% greater and the power law that is five times larger. Note that the shock-standoff distance given for the two power law cases may be inaccurate on the scale of comparing them to the other two axial shapes. The power law case had a method written in this work that is meant to give rough answers

rather than results precise enough to compare shapes with values closer than ± 100 W/cm^2 at the given design point.

Table 8.3. Aerothermodynamic comparison of L_V/D and $\eta_V L_V/D$ results at M_∞ = 32.8255 (m = 4).

	Maximum L_V/D			***Maximum $\eta_V L_V/D$***		
	SS* $\theta_s = 89^o$ $n_2 = 1.3$ $e = -0.968$ $\alpha = 17.6^o$	SC $\theta_c = 59^o$ r_n/d=0.15 n_2 =1.3 e =-0.968 $\alpha = 15.1^o$	PL b = 0.642 A = 0.900 n_2=1.3 e =-0.968 α= 9.51^o	SS $\theta_s = 89^o$ $n_2 = 1.3$ e = -0.968 $\alpha = 17.6^o$	SC $\theta_c = 56.7^o$ r_n/d=0.24 n_2 =1.57 e =-0.968 $\alpha = 20.0^o$	PL b = 0.642 A = 0.900 n_2=1.3 e =-0.968 α= 9.51^o
$C_{L,V}$	0.262	0.196	0.155	0.262	0.235	0.155
L_V/D	1.10	0.946	2.10	1.10	0.752	2.10
$(L_V/D)_\alpha$	-0.0184	-0.0233	-1.69	-0.0184	-0.582	-1.69
$C_{m,cg,\alpha}$ (/rad)	-0.0806	-0.163	-0.0377	-0.0806	-0.00096	-0.0377
$C_{n,cg,\beta}$ (/rad)	0.0302	0.0523	0.00652	0.0302	0.0778	0.00652
$C_{l,cg,\beta}$ (/rad)	-0.0719	-0.0754	-0.0183	-0.0719	-0.119	-0.0183
$q_{s,tot}$ (W/cm^2)	491	666	3000	491	558	3000
$q_{s,conv}$ (W/cm^2)	304	555	2820	304	435	2820
$q_{s,rad}$ (W/cm^2)	187	110	180	187	123	180
Δ_{so} (cm)	11.0	3.3	10.3	11.0	4.2	10.3
X_{cp}/l	0.423	0.636	0.562	0.423	0.618	0.562
X_{cg}/l	0.641	0.723	0.683	0.641	0.705	0.683
CG type**	X75	X75	X75	X75	X75	X75
η_v	89.0%	83.6%	84.7%	89.0%	85.2%	84.7%
	Initial designs					
	$\theta_s = 85^o$ $n_2 = 1.5$ e = -0.9 $\alpha = 25^o$	$\theta_c = 60^o$ r_n/d=0.25 n_2 =1.6 e =-0.9 $\alpha = 20^o$	b = 0.80 A = 1.5 n_2=1.8 e =-0.01 $\alpha = 20^o$	$\theta_s = 85^o$ $n_2 = 1.5$ e = -0.9 $\alpha = 25^o$	$\theta_c = 60^o$ r_n/d=0.25 n_2 =-1.6 e =-0.9 $\alpha = 20^o$	b = 0.6 A = 0.9 n_2 = 1.3 e = -0.968 $\alpha = 9.51^o$

*Axial shape key: SS: spherical segment, SC: spherically-blunted cone, PL: power law.
** CG type key: UD: uniform density, X75: uniform density except $X_{cg,75} = 75\% X_{cg,UD}$.

Additionally, the power law shape has a slope that is discontinuous at the nose, which could render an attached shock rather than a bow shock if it is not blunted. Resolving such effects would be a good topic for future work.

These results can be compared to those of the parametric analysis in Table 7.3. Of the spherically-blunted cone and power law geometries shown in Table 8.3, the better of the two of each are plotted in Figure 8.2 for comparison against Figure 8.1(c).

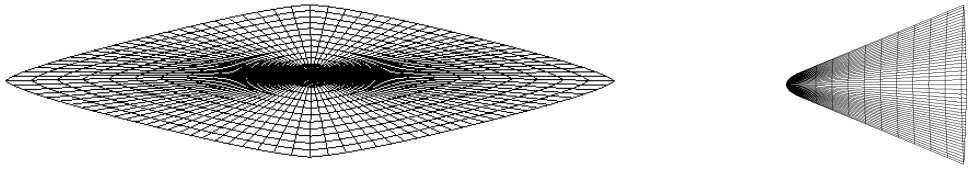

a) Spherically-blunted cone axial shape with L_V/D = 0.946.

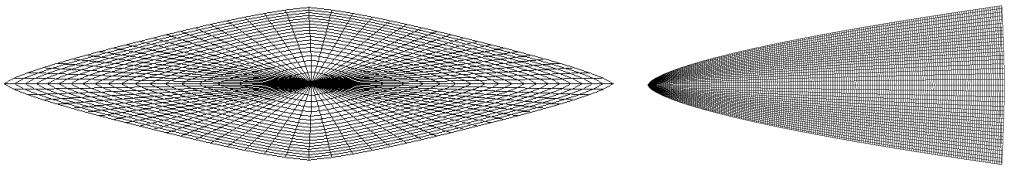

b) Power law axial shape with L_V/D = 2.10.

Figure 8.2. Optimized geometries from Table 8.3.

Once the shapes are visually compared, the reason for the power law having an extremely high convective heat transfer flux is due to its small nose radius. The results in Table 8.3 are consistent with this understanding.

The iteration histories for the spherically-blunted cone axial shape with maximum $\eta_V L_V/D$ are included in Figure A.0.3. The iteration history of the objective function indicates an increase of more than 400% over the initial design. Although the design variables appear to barely change at first glance, an eccentricity change from –0.90 to –0.968 changes the semi-major to semi-minor axis length ratio from two to four, which is a substantial change from an aerodynamic standpoint.

To determine if Mach number independence existed for the aerodynamics, the spherically-blunted cone was run at initial designs of $\theta_c = 60^o$, $r_n/d = 0.25$, $n_2 = 1.6$, $e = -0.9$, $\alpha = 20^o$ for $M_\infty = 30$ through 41 at an altitude of 200000 ft. For $M_\infty > 42$,

Tannehill's correlations[54] are out of their pressure and density ranges at 200000 ft, producing a limit on this code. The solution for maximizing L_V/D is the same throughout the hypersonic freestream Mach number range 30 through 41. The spherically-blunted cone solution has an $L_V/D = 0.946$ at $\alpha = 15.1^o$ and is included in Table 8.3.

8.2. *Maximizing* $(L_V/D)/q_{s,tot}$

Seven optimization runs of the spherical-segment, five of the spherically-blunted cone, and seven of the power law geometries were completed for maximizing $(L_V/D)/q_{s,tot}$. Constraints G_1 through G_5 have been applied. Although different initial designs were tested in this analysis, the initial designs for the spherical-segment and spherically-blunted cone for this optimization are the same as that required for maximizing L_V/D. The aerothermodynamic performance and stability characteristics of the heat shield shapes with maximum $(L_V/D)/q_{s,tot}$ are included in Table 8.4, with the initial designs listed at the bottom.

The maximized $(L_V/D)/q_{s,tot}$ spherical-segment configuration is identical to its maximized (L_V/D) configuration. Since the spherical-segment configuration is shown in Figure 8.1(c), the other two configurations are shown in Figure 8.3. The spherically-blunted cone cases have nearly identical L_V/D, but the configuration in this optimization has a 27.4% lower $q_{s,tot}$ than the maximized (L_V/D) configuration. The optimizer accomplishes this by increasing the nose-radius-to-base-diameter ratio and increasing angle of attack, as shown in the iteration histories included in Figure A.0.4. This configurations r_n/d is 145% larger than that of the maximized (L_V/D)

configuration. The optimizer also found a slighter higher L_V/D in this optimization, but they are within 8% of each other.

Table 8.4. Aerothermodynamic comparison of $(L_V/D)/q_{s,tot}$ results at $M_\infty = 32.8255$ ($m = 4$).

	Maximum $(L_V/D)/q_{s,tot}$		
	SS* $\theta_s = 89^o$ $n_2 = 1.3$ $e = -0.968$ $\alpha = 17.6^o$	SC $\theta_c = 55^o$ r_n/d=0.367 n_2 =1.3 e =-0.968 $\alpha = 15.5^o$	PL $b = 0.426$ $A = 0.900$ n_2=1.3 e =-0.968 α= 14.3^o
$C_{L,V}$	0.262	0.198	0.221
L_V/D	1.10	0.942	1.35
$(L_V/D)_\alpha$ (/rad)	-0.0184	-0.118	0.0429
$C_{m,cg,\alpha}$(/rad)	-0.0806	-0.141	-0.0463
$C_{n,cg,\beta}$(/rad)	0.0302	0.0468	0.00627
$C_{l,cg,\beta}$(/rad)	-0.0719	-0.0682	-0.0134
$q_{s,tot}$ (W/cm^2)	491	483	916
$q_{s,conv}$ (W/cm^2)	304	355	600
$q_{s,rad}$ (W/cm^2)	187	129	316
Δ_{so} (cm)	11.0	4.6	36.8
X_{cp}/l	0.423	0.591	0.490
X_{cg}/l	0.641	0.679	0.630
CG type**	X75	X75	X75
η_v	89.0%	86.4%	84.6%
	Initial designs		
	$\theta_s = 85^o$ $n_2 = 1.5$ $e = -0.9$ $\alpha = 25^o$	$\theta_c = 60^o$ r_n/d=0.25 n_2 =1.6 e =-0.9 $\alpha = 20^o$	$b = 0.5$ $A = 1.0$ n_2=1.4 e =-0.9 $\alpha = 10.0^o$

*Axial shape key: SS: spherical segment,
SC: spherically-blunted cone, PL: power law.
** CG type key: UD: uniform density,
X75: uniform density except $X_{cg,75} = 75\% X_{cg,UD}$.

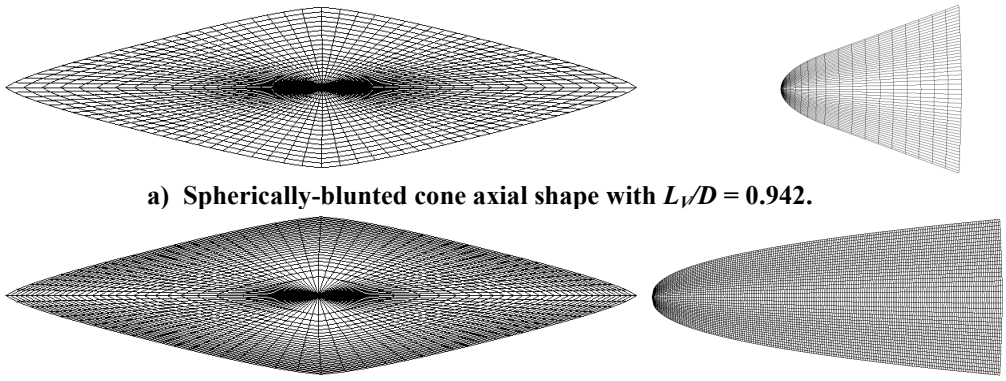

a) Spherically-blunted cone axial shape with L_V/D = 0.942.

b) Power law axial shape with L_V/D = 1.35.

Figure 8.3. Maximized $(L_V/D)/q_{s,tot}$ geometries from Table 8.4.

The optimum power law geometry produced the largest L_V/D of 1.35 and total heat flux of 916 W/cm^2. The stagnation-point heat fluxes for these vehicles are within the feasibility range of modern materials such as the Crew Exploration Vehicle, which is being designed for 1000 W/cm^2. The variance in shock-standoff distance shows the limitations of the method. It should not be used to compare power law and spherically-blunted cone axial shapes.

A short analysis of the objective function $(L_V/D)/(q_{s,tot})^n$ was completed with n = 0.25, 0.50, 0.75, 1.0, 2.0, and 3.0 using the spherical segment. The results did not change except at n = 3.0. For this case, the L_V/D was reduced from 1.10 to 0.54, and $q_{s,tot}$ was slightly reduced from 493 to 479. Since there is no significant difference between the total heat flux values even though the lift-to-drag ratio was halved, it was decided that the n = 3.0 configuration had lower performance. Overall, the optimization is not sensitive to a change in n < 3.0, and when it is sensitive, there is evidence that it lowers aerodynamic performance. Since the proportions of convective and radiative heat flux to the total heat flux change with velocity, the optimization has been run over a range of Mach numbers to observe how much the configurations change. The spherically-blunted cone axial shape is chosen for this study since it is

directly connected to the convective heat flux correlation used in this work. The r_n/d generally decreases with an increase in Mach number as shown in Figure 8.4. This is expected since the proportion of radiative heat transfer to the total increases dramatically over this range and surpasses the convective have flux around Mach 40. While the total heat flux steadily increases with Mach number, the optimized configurations have L_V/D values that increase and decrease. Table A.0.1 in the appendix provides complete configuration information for this Mach number study.

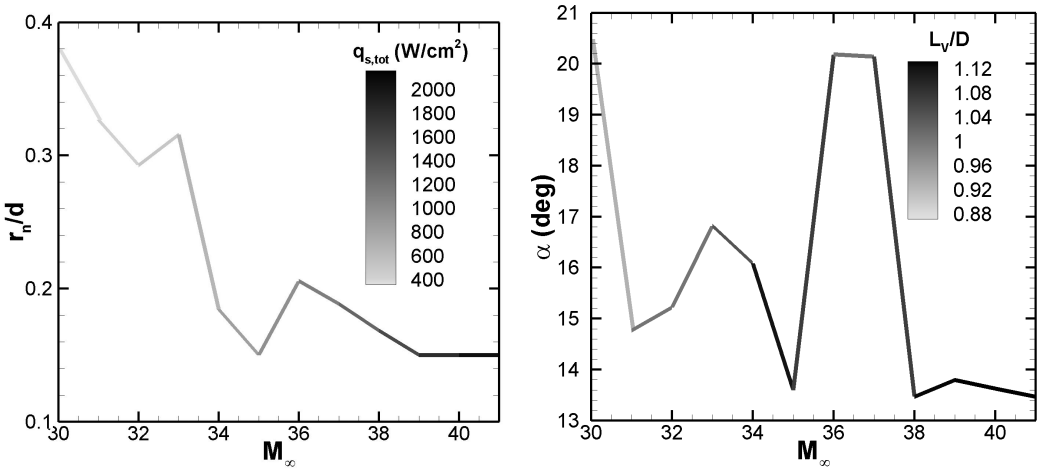

a) Heat transfer flux $q_{s,tot}$ results. **b) L_V/D results.**

Figure 8.4. Maximized $(L_V/D)/q_{s,tot}$ results for $M_\infty = 30 - 41$.

8.3. Minimizing $q_{s,tot}$

Since $q_{s,tot}$ was the first objective function optimized, fifty-two optimization runs were completed of the spherical-segment to minimize $q_{s,tot}$. Also, twelve runs of the spherically-blunted cone and six runs of the power law geometries were completed. Constraints G_1 through G_5 were applied. When changing m to vary the number of sides of the cross-section, the minimum $q_{s,tot}$ was nearly constant. For m = 5, 6, and 7, the minimum total heat flux was between 375 and 390 W/cm^2. The

parallelogram m = 4 cross-section had a slightly lower minimum at 339 W/cm^2, but the employed methods should not be taken as accurate to the extent of differentiating between shapes with ±50 W/cm^2 of each other. Instead it is concluded that all these cases have approximately the same minimum within 10-15% of each other.

Not all of the shapes with local minimum necessarily look similar to each other. As shown in Figure 8.5, the optimal solution for the parallelogram is concave while the hexagonal geometry is not although they both were run at the same initial designs. Still these shapes have similar stagnation-point heat transfer fluxes. For the optimized parallelogram, the radiative heat flux is 180 W/cm^2 while the convective heat flux is 160 W/cm^2 since the r_n/d is much greater than one.

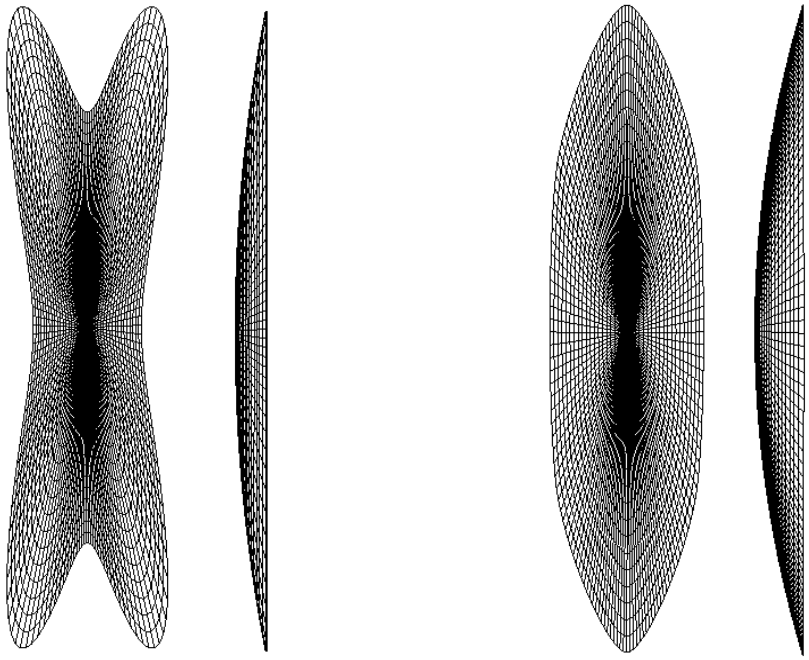

a) m = 4, θ_s = 16.1°, n_2 = 4.0, e = 0.968, α = -12.6°. **b) m = 6, θ_s = 15.9°, n_2 = 1.67, e = 0.968, α = -10.9°.**

Figure 8.5. Minimum $q_{s,tot}$ configurations, spherical-segment axial shape.

Table 8.5 provides the optimized results for parallelogram geometries with each of the three axial shapes. While L_V/D is approximately the same for each axial

shape, the vertical lift coefficient of the power law shape is three times greater than that of the other two. The spherical-segment and spherically-blunted cone results are similar because that they are similar shapes.

Table 8.5. Aerothermodynamic comparison of $q_{s,tot}$ results at M_∞ = 32.8255 (m = 4).

	Minimum $q_{s,tot}$		
	SS* θ_s = 16.1° n_2 = 4.0 e = 0.968 α = -12.6°	SC θ_c = 55° r_n/d=2.0 n_2 =4.0 e = 0.968 α = -12.3°	PL b = 0.485 A = 7.71 n_2=1.56 e = -0.0771 α = -12.5°
$C_{L,V}$	0.113	0.117	0.347
L_V/D	0.215	0.212	0.211
$(L_V/D)_\alpha$ (/rad)	-1.01	-1.01	-0.998
$C_{m,cg,\alpha}$(/rad)	-0.0276	-0.0259	-0.103
$C_{n,cg,\beta}$(/rad)	0.0173	0.0178	0.0553
$C_{l,cg,\beta}$(/rad)	-0.00264	-0.0021	0.00000235
$q_{s,tot}$ (W/cm^2)	339	393	349
$q_{s,conv}$ (W/cm^2)	160	152	154
$q_{s,rad}$ (W/cm^2)	179	242	195
Δ_{so} (cm)	9.90	19.5	12.4
X_{cp}/l	0.641	0.644	0.661
X_{cg}/l	0.664	0.596	0.589
CG type**	X75	X75	X75
η_v	40.2%	37.6%	44.0%
	Initial designs		
	θ_s = 25° n_2 = 1.3 e = -0.8 α = -10°	θ_c = 65° r_n/d=1.183 n_2 =1.8 e =-0.8 α = -10°	b = 0.35 A = 7.0 n_2=1.5 e =-0.10 α = -12.0°

*Axial shape key: SS: spherical segment,
SC: spherically-blunted cone, PL: power law.
** CG type key: UD: uniform density,
X75: uniform density except $X_{cg,75}$ = 75% $X_{cg,UD}$.

The blunted cone has an ε = 14.4° compared to the 16.1° of the spherical-segment. The high value of r_n/d indicates that this blunted cone is a disguised spherical-segment. The iteration histories for the optimized spherical-segment are included in Figure A.0.5. The geometries with the spherically-blunted cone and power law axial shapes are shown in Figure 8.6.

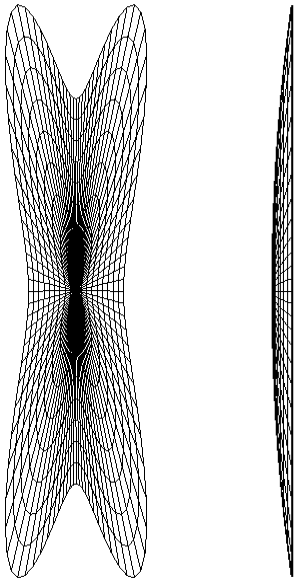

a) Spherically-blunted cone axial shape with $q_{s,tot}$ = 393 W/cm^2.

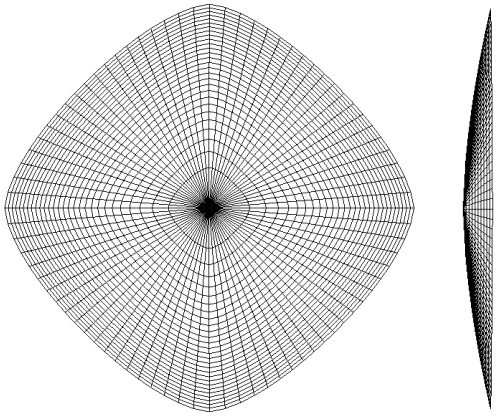

b) Power law axial shape with $q_{s,tot}$ = 349 W/cm^2.

Figure 8.6. Minimum $q_{s,tot}$ geometries from Table 8.5.

The trend that is suggested from this observation is that if a concave rounded-edge polygon and a rounded-edge polygon have the same L_V/D, the vertical lift coefficient of the rounded-edge polygon is probably greater than that of its concave counterpart.

Because this spherically-blunted cone has an $r_n/d = 2$, it is a spherical-segment. One could approximate the Apollo CM spherical segment with a larger nose-radius-to-diameter ratio $r_n/d = 1.1831$ and a half-cone angle of 65^o. The initial designs for the blunted cone are the dimensions of the Apollo CM except for the oblate eccentricity. The spherically-blunted cone axial shape allows the optimization to cover some of the spherical-segment shapes in its own design space.

The heat shield with the spherical-segment axial shape has the smallest total heat flux, but as mentioned before, all that can be concluded from these results is that the three axial shapes have approximately the same minimum. It would be expected that the spherical-segment axial shape would produce the smallest total heat flux since it can produce the highest nose radius in a region where convection easily dominates if the nose radius is not large.

Since the heat flux increases with an increase in velocity, the optimal geometry may change. To observe any geometric changes to the optimal configurations, optimization throughout the freestream re-entry Mach number range from 30 to 41 has been completed. It is expected for the radiative heat flux to begin to dominate as the freestream Mach number is increased from $M_\infty = 30$. Because the radiative heat flux for blunt bodies increases with an increase in nose radius, according to the correlations, the nose radius of the optimized vehicle should generally drop when the freestream Mach number is increased. Figure 8.7 shows how the nose-radius-to-diameter radius drops with increasing M_∞, and complete geometric characteristics of the optimized configurations are listed in Table A.0.2. For this objective function at the given initial designs, the major drop in nose radius occurs

between $M_\infty = 33$ and 34. In this case, it could be that the spherically-blunted cone is a spherical-segment at $M_\infty = 33$ that changes into a spherically-blunted cone at $M_\infty = 34$.

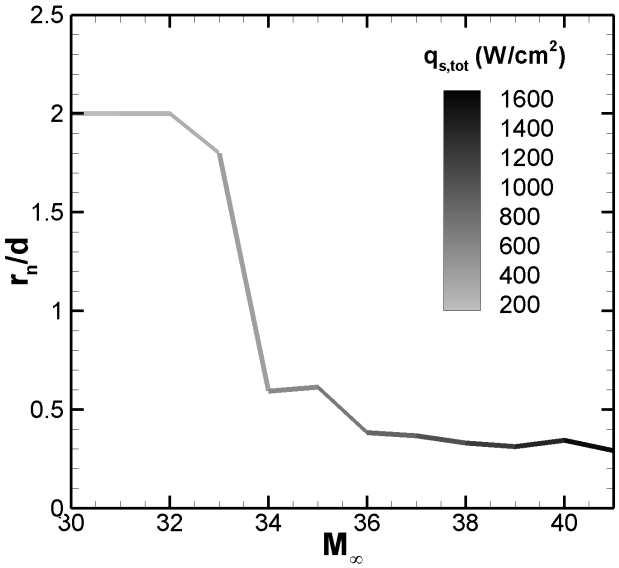

Figure 8.7. Minimized $q_{s,tot}$ results for $M_\infty = 30 - 41$.

It can be concluded that the spherically-blunted cone would be the choice for missions with highest heat fluxes present at an altitude of 200000 ft moving at $M_\infty \geq 34$. At this altitude, the Apollo CM was moving at $M_\infty = 32.8255$, and strictly from a heat transfer standpoint, the results of this optimization are consistent with the decision to use a spherical-segment for Project Apollo.

8.4. Minimizing $C_{m,cg,\alpha}$

Nineteen optimization runs of the power law, six of the spherical-segment, and three of the spherically-blunted cone were completed for minimizing the pitching moment derivative $C_{m,cg,\alpha}$. If the blunt-body is entering an atmosphere at angle of attack, then the magnitude of the pitching moment derivative is probably the largest out of the three stability derivatives. In this case, minimizing $C_{m,cg,\alpha}$ generates

negative values with large magnitudes, and this corresponds to the most statically stable configuration in the longitudinal direction. Constraints G_1 through G_5 have been applied. Since the pitching moment stability requirement constraint G_3 is being used, MMFD requires the initial configuration to be longitudinally stable. As a result, $C_{m,cg,\alpha}$ is already negative before the optimization begins, and so the optimizer is searching for the stable configuration with a larger $|C_{m,cg,\alpha}|$.

The three configurations that are the most statically stable longitudinally are shown in Figure 8.8.

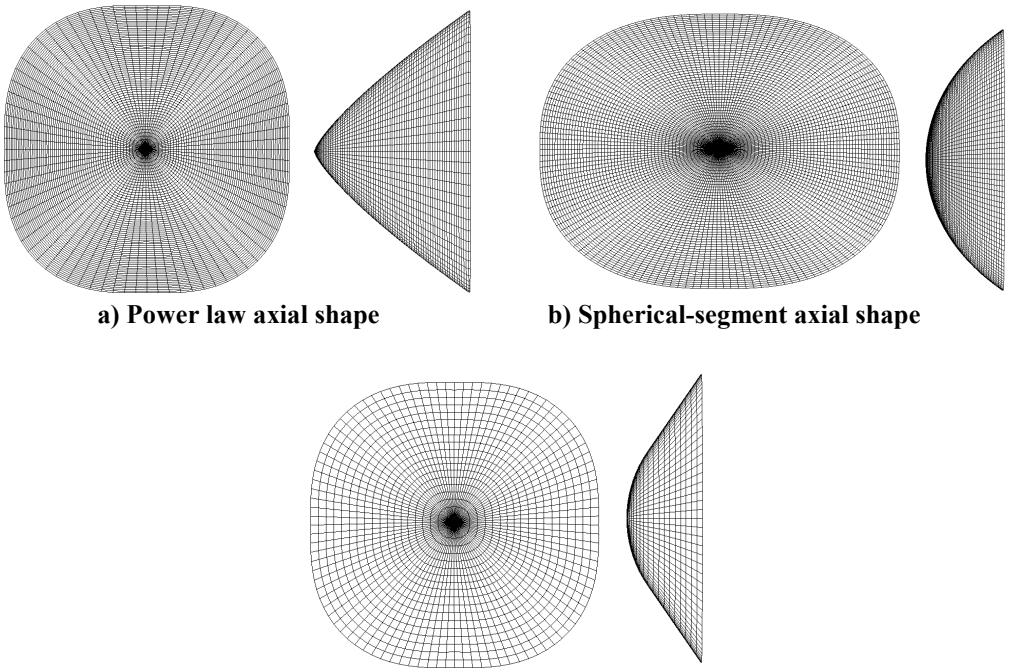

a) Power law axial shape **b) Spherical-segment axial shape**

c) Spherically-blunted cone axial shape

Figure 8.8. Minimum $C_{m,cg,\alpha}$ geometries (m = 4) in Table 8.6.

The optimized power law geometry has a pointed nose, and the heat flux constraint is active. The spherically-blunted cone has a smaller nose radius than the spherical-segment. Neither the blunt cone nor the power law have the eccentricity of the spherical-segment. The aerothermodynamic performance and stability characteristics of these shapes are listed in Table 8.6. All three shapes have a minimum value of

approximately –0.30/rad for the pitching moment stability derivative, and the power law shape has value that is at least 27% larger in magnitude than the other two geometries.

Table 8.6. Aerothermodynamic comparison of $C_{m,cg,\alpha}$ results at $M_\infty = 32.8255$ ($m = 4$).

	Minimum $C_{m,cg,\alpha}$		
	SS* $\theta_s = 47.9^o$ $n_2 = 2.24$ $e = -0.64655$ $\alpha = -2.68^o$	SC $\theta_c = 55^o$ r_n/d=0.403 n_2 =2.25 e = 0.0149 $\alpha = -0.656^o$	PL b = 0.78 A = 0.90 n_2=2.28 e = 0.119 $\alpha = 26.8^o$
$C_{L,V}$	0.0269	0.00918	0.0139
L_V/D	0.0219	0.00705	0.0184
$(L_V/D)_\alpha$ (/rad)	-0.452	-0.474	0.379
$C_{m,cg,\alpha}$(/rad)	-0.285	-0.276	-0.363
$C_{n,cg,\beta}$(/rad)	0.165	0.138	0.00369
$C_{l,cg,\beta}$(/rad)	0.00170	-1.6E-5	0.0000888
$q_{s,tot}$ (W/cm^2)	452	469	3000
$q_{s,conv}$ (W/cm^2)	262	338	2890
$q_{s,rad}$ (W/cm^2)	190	131	110
Δ_{so} (cm)	11.3	4.87	3.56
X_{cp}/l	0.617	0.622	0.636
X_{cg}/l	0.656	0.669	0.707
CG type**	X75	X75	X75
η_v	85.9%	79.8%	93.2%
	Initial designs		
	$\theta_s = 85^o$ $n_2 = 2.0$ $e = -0.8$ $\alpha = 25^o$	$\theta_c = 60^o$ r_n/d=0.25 n_2 =1.6 e =0.01 $\alpha = -20^o$	b = 0.75 A = 2.0 n_2=2.0 e = 0.5 $\alpha = -20^o$

*Axial shape key: SS: spherical segment, SC: spherically-blunted cone, PL: power law.
** CG type key: UD: uniform density, X75: uniform density except $X_{cg,75} = 75\% X_{cg,UD}$.

The value of –0.30/rad is approximately twice the pitching stability derivative of the Apollo Command Module.[8] This can also be noticed when comparing the results of

this work in Table 7.3. The optimum angle of attack for each is near zero and due to the fact that these shapes are symmetric about the horizontal body axis, the lift-to-drag ratio is nearly zero.

Similar to the Apollo Command Module, the spherical-segment has a slightly unstable rolling moment. This is allowed in the constraints on purpose in order to allow the optimizer to choose heat shields similar to the Apollo Command Module's if desired. The Apollo CM is estimated to have had a $C_{l,cg,\beta}$ of 0.005/rad (discussed in Chapter 6).

The iteration histories for the optimized power law configuration are included in Figure A.0.6. The optimizer produced a geometry with greater stability by decreasing coefficient A and the eccentricity, and greatly decreasing the magnitude of α to 0^o. The iteration histories for the spherical-segment configuration with maximum longitudinal static stability are included in Figure A.0.7. The optimizer decreased the magnitude of α and θ_s dramatically and originally changed the eccentricity greatly, but then it brought the eccentricity back to nearly its original value.

Most of the results from optimizing other objective functions have magnitudes of $C_{m,cg,\alpha}$ less than 0.10/rad, and only some of the spherically-blunted cone and power law results for other objective functions have magnitudes greater than 0.10/rad. The maximum $\eta_V L_V/D$ blunted cone configuration is neutrally longitudinally stable. As a result, stability has to be traded-off with L_V/D and $q_{s,tot}$ to produce an optimal-set geometry.

The configurations with optimal sets of aerothermodynamic characteristics have cross-sections that are rounded-edge parallelograms and are generated by

maximizing (L_V/D)/$q_{s,tot}$. These configurations have the characteristics listed in Table 8.4. All of them have high lift-to-drag ratios (above 0.5) for space capsules, total heat fluxes less than or at most equal to the design requirement for NASA's CEV of 1000 W/cm^2, and stable stability derivatives. The spherically-blunted cone configuration has a pitching stability derivative value of –0.14/rad that is near the –0.16/rad of the Apollo CM, but the required magnitudes for this and the other stability derivatives have yet to be determined. Most of this optimization analysis is included concisely in Ref. [73].

8.5. Limitations of this Optimization

Several optimization runs were completed since different minima were encountered with different initial designs. The design space does not have only one minimum for each objective function. These optimization runs found local minimum, and the one that had the lowest value is identified as the engineering global minimum. The design space has several minima. For example, if the initial design for maximizing L_V/D for the spherical segment were changed from $\theta_s = 85^o$, $n_2 = 1.5$, $e = -0.9$, and $\alpha = 25^o$ to $\theta_s = 25^o$, $n_2 = 1.4$, $e = -0.01$, and $\alpha = -10^o$, the optimizer finds a local optimum value of 0.320 instead of 1.10 for L_V/D. If the optimizer runs without constraint vector $\vec{G}$, then it finds a value of 0.575 instead of 1.10. It is understandable for the design space to have more than one maximum, but one has to accept that there could be a better optimum in the design space that was not found. There are other optimization methods for finding the global maximum, but it is unknown to the author whether those methods would provide better results.

In finding the maximum L_V/D, the optimizer had to be given initial designs based on the parametric analysis in order to find the global minimum. The parametric analysis gave the best starting point for the optimizer in maximizing L_V/D by setting some of the initial designs equal to the maximum in Figure 7.9. Then the optimizer was able to find the maximum. This exemplifies the importance of a well-constructed parametric analysis.

In a few cases, the optimizer did not vary one or two of the design variables. In maximizing $\eta_V L_V/D$, there was no variance in angle of attack for the spherically-blunted cone case. This work uses a semi-empirical method for varying the radiative heat flux with angle of attack, and this method is modified to account for n_2 and eccentricity, as well as the power law and blunted cone axial shapes. It is shown in Figure 7.11 that this modified method produces several ripples in the design space. Aside from the ripples, it is also nearly flat for $n_2 < 2$, and it is believed that these are the reasons that the optimizer does not find an optimum angle of attack far from the initial angle of attack when minimizing $q_{s,tot}$. Better optima may be found in future work.

Chapter 9. Conclusions

9.1. Summary of Results

9.1.1. Parametric Analysis

A parametric analysis of candidate blunt-body heat shield shapes for a Crew Exploration Vehicle has been conducted to determine the main effects of several geometric parameters on the aerothermodynamic performance and stability of the vehicle. This analysis is completed by picking a cross-section and an axial shape to generate a heat shield mesh, and then by placing the mesh into an aerodynamics program based on modified Newtonian flow. The results were validated with wind tunnel and flight test data, and $C_{m,cg}$ and L/D matched the values of the Apollo Command Module (CM) closer than the results of C_L and C_D.

Although the hexagon is the most aerodynamically stable of the polygons (m = 4–10), it did not have the highest L_V/D, and L_V/D became larger as n_2 approaches the elliptical cross-section (n_2 = 2). There is a tradeoff between L_V/D and the pitching moment stability derivative. Although the increase in L_V/D of 56.1% may be beneficial by making the cross-section strongly oblate at e = -0.95, the heat shield would be longitudinally statically unstable assuming uniform density. One way to remove this instability is by moving the center of gravity forward by 23.5% to X_{cg}/l = 0.400, and moving the x-location of the center of gravity forward by 25% (was applied in some of the optimization runs to further open up the design space).

A change in cross-section did not affect the aerodynamic performance of the heat shield as significantly as a change in axial shape. A change in axial shape rendered a larger range of aerodynamic characteristics. It was also observed that the magnitudes of the longitudinal and directional stability derivatives are maximized with an elliptical base as opposed to a rounded-edge hexagonal concave base. Table 7.3 summarized the sensitivities of the aerodynamic parameters to the geometric parameters. C_m varied strongly with α, θ_s, θ_c, and A while the other moment coefficients and stability derivatives varied strongly with θ_s, θ_c, and A. The results of $C_{l,\beta}$ are of the same order of magnitude as other blunt-body designs. For $\theta_s < 35^o$, an increase in eccentricity from 0.0 to 0.95 increases the volumetric efficiency by up to 10%.

9.1.2. Optimization Results

Incorporating all of these parameters into an optimization process has assisted in producing heat shield shapes with improved combinations of aerodynamic characteristics. By maximizing L_V/D it was noticed that the parallelogram base cross-section (m = 4) provides the highest L_V/D. Because this is one of the two most important characteristics, the other being $q_{s,tot}$, the optimization continued with m = 4 rather than at the m = 6 that produced the most longitudinally stable configurations.

Minimizing the heat transfer flux $q_{s,tot}$ produced polygon bases with and without concavity, and the trend was noticed that even though two shapes may have the same L_V/D, they do not necessarily have the same $C_{L,V}$. In this case, the rounded-edge polygon had a greater vertical lift coefficient by 300%.

The results of maximizing L_V/D or minimizing $q_{s,tot}$, or $C_{m,cg,\alpha}$ was not as promising as maximizing a combinations of these parameters. Each of these has trade-offs with the other. The maximum L_V/D was usually located between an $|\alpha|$ of 20^o and 30^o while the minimum $C_{m,cg,\alpha}$ would be present near zero angle of attack. Most of the optimum heat shields shapes are symmetric about the horizontal axis, and thus produce no lift at zero angle of attack, rendering a low lift-to-drag ratio. The minimum $q_{s,tot}$ configurations all had $L_V/D \approx 0.2$, which is lower than the Apollo CM's 0.34. The maximum L_V/D would produce high $q_{s,tot}$ especially for the spherically-blunted cone and power law axial shapes. However, by choosing to maximize $(L_V/D)/q_{s,tot}$, the optimizer was able to produce a better, more optimal set of aerothermodynamic characteristics. In this case, the geometries with rounded-edge parallelogram cross-sections and maximum $(L_V/D)/q_{s,tot}$ provide the most desired set of characteristics (listed in Table 8.4) for the design point altitude of 200000 ft and $M_\infty = 32.8255$.

Since the heat transfer increases with freestream Mach number, an analysis was conducted on how the optimum shape changes for $M_\infty = 30 - 41$. When minimizing $q_{s,tot}$ by itself, a large drop in the optimum r_n/d ratio occurs between Mach 33 and Mach 34. The value of r_n/d at Mach 33 generates a spherical-segment while the value at Mach 34 generates a spherically-blunted cone, and this drop shows at which Mach number it would be ideal to switch between the two. Since the Apollo 4 CM was traveling at $M_\infty = 32.8255$, and the manned Apollo Command Modules traveled slower at this altitude, this research agrees with the choice to use a spherical-segment instead of a spherically-blunted cone for Project Apollo from a heat transfer

standpoint. However, when maximizing $(L_V/D)/q_{s,tot}$ over this range of freestream Mach numbers, all the optimum results suggest a spherically-blunted cone over the spherical-segment. This renders a higher $q_{s,tot}$ than produced during the Apollo 4 trajectory and may have created a technology difficulty at the time.

Due to the fact that the design space had several local minima, perhaps another optimization method would have been better suited for locating a global minimum. Since several optimization runs have been completed, it is certain that these results are near the value of the global minimum, but there is the possibility that the true global minimum has not been found. However, several optimal heat shield designs with improved characteristics over previous work have been discovered.

9.2. Suggestions for Future Work

A substantial amount of future work in planetary entry vehicles can be completed to improve upon both this work and the general understanding of the field. To increase the accuracy of the aerothermodynamics code, the following additions could be made:

- Account for corner radius. The work of Zoby[44] may also assist in distinguishing heat shields of the same axial shape and cross-section but different corner radii. The corner radius geometry can also be added to the 3D mesh so that the surface pressure distribution accounts for it.
- Improve the method for estimating the shock-standoff distance for angles of attack, especially for the power law axial shape and in accounting for base eccentricity.

- Use a more accurate method to determine the surface pressure distribution. For this work Newtonian Impact Theory was validated, but if the scope of the project were to include analyzing the boundary layer, advanced CFD would need to be utilized.

To increase the scope of the aerothermodynamics code, the following additions could be made:

- Include a second-order trajectory for determining non-oscillatory trajectories. Loh[74] offers a way to modify second-order trajectory theory to approximate oscillatory trajectories. A second-order trajectory code does not require the computational time of full trajectory packages such as POST or OTIS. As a result, the heat transfer correlations can be applied at each point in the trajectory to approximate the heat transfer load on the vehicle.
- Incorporate more axial shapes: the raked, biconic, and bent-biconic cones.
- Include thermal material properties and temperature constraints.
- Include a model for high temperature gas properties at 200000 ft, $M_\infty > 42$. The Tannehill correlations are outside their range for these freestream Mach numbers.
- Develop a method of determining the point of maximum heating for a general 3D body. The velocity gradient could be modeled to determine the point of maximum convective heating for a general 3D body. Zoby[44] provides some results based on the change in the velocity gradient in order to calculate the convection for values of $r_n/d > 2$ more accurately than using the inverse square-root of the nose radius.

- Validation of the stagnation-point radiative heat transfer curve-fits of Suttles[75] for hyperbolic earth entry with velocities from 11 to 16 km/s.

Future work concerning planetary entry vehicles outside this computational code that would benefit the field:

- Study laminar, transition, and turbulent boundary layer heat transfer on blunt bodies for $M_\infty > 25$. Wind tunnel analysis of rounded-edge concave heat shields would help in investigating these phenomena. The Apollo Command Module's heat shield experienced laminar heat transfer. Turbulent heat transfer is unknown at $M_\infty > 40$, especially the effects of radiation cooling and convective-radiative coupling that reduce the total heat transfer flux. For a phenomena that increases exponentially with Mach number, the radiative heat transfer can easily be miscalculated for $M_\infty > 40$.
- Static and dynamic stability guidelines for human space capsules.
- Flight tests and wind tunnel experiments for $M_\infty > 40$ ranging up to $M_\infty = 55$. This could provide arguably the most useful results concerning planetary entry at $M_\infty > 40$. Current aerothermodynamic understanding of this region of freestream Mach numbers is modest. Since rolling moment experimental and flight data is almost nonexistent, measuring the rolling moment on both axisymmetric and non-axisymmetric heat shields would be beneficial. High temperature correlations, radiation and general heat transfer models could be produced for the first time. Hypersonic aerothermodynamic models can be improved. Some models do exist, but they do not apply well to $M_\infty > 40$.

Appendix A: Optimization Iteration Histories

A.1 Maximizing Lv/D and ηvLv/D

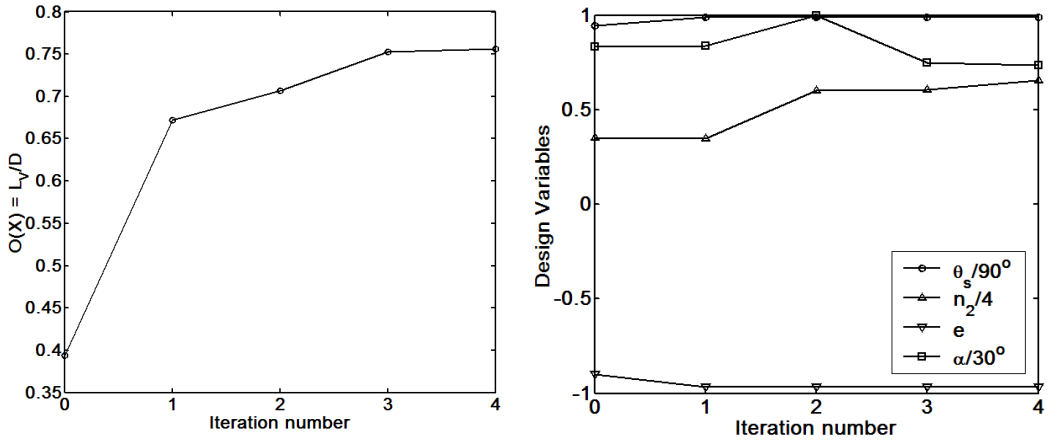

a) Objective function iteration history. **b) Design variable iteration history**

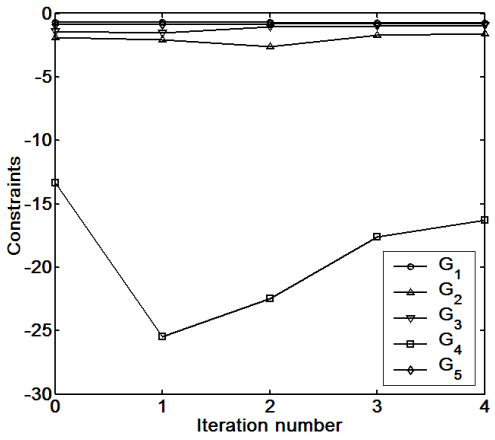

c) Constraints iteration history.

Figure A.0.1. Iteration history for maximum L_V/D hexagonal shape (m = 6) in Table 8.2.

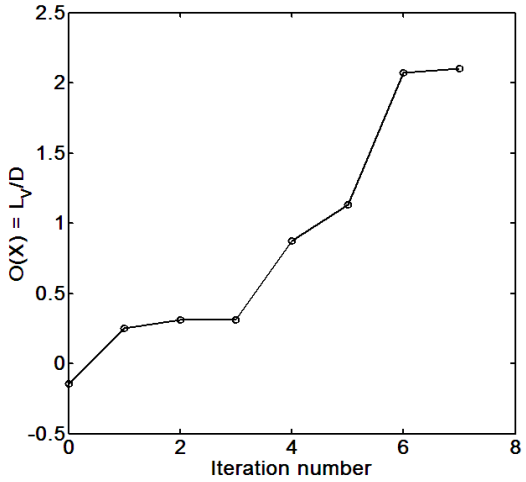

a) Objective function iteration history.

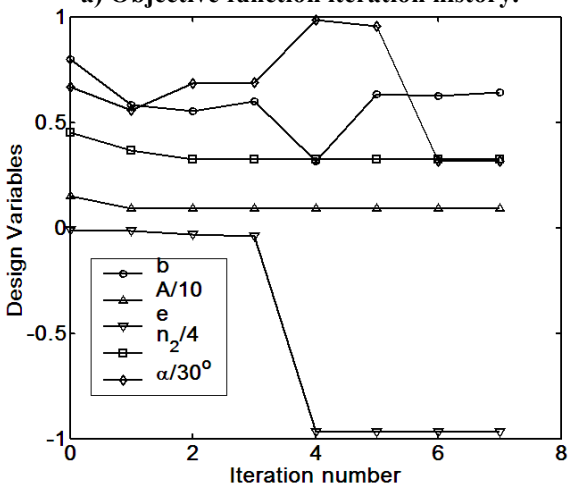

b) Design variable iteration history

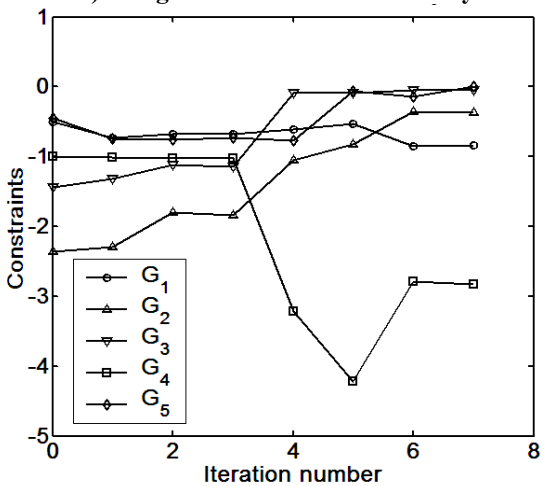

c) Constraints iteration history.

Figure A.0.2. Iteration history for maximum L_V/D power law/parallelogram (m = 4) in Table 8.3.

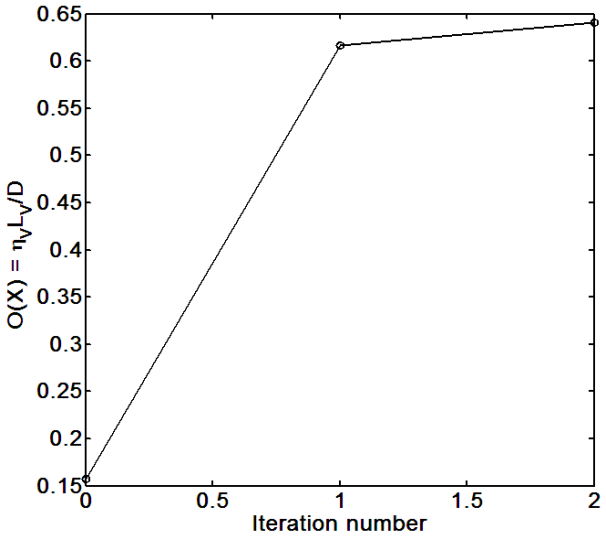

a) Objective function iteration history.

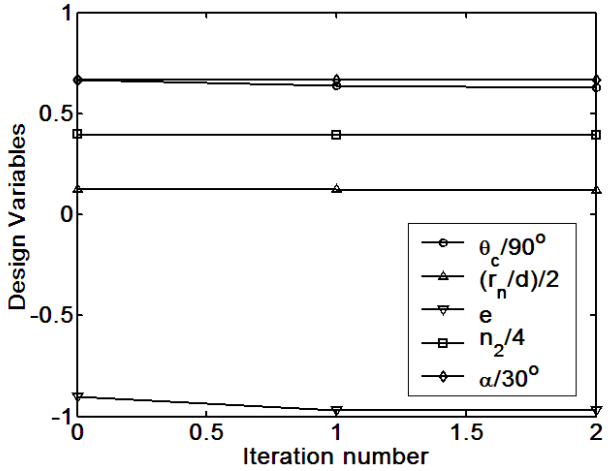

b) Design variable iteration history

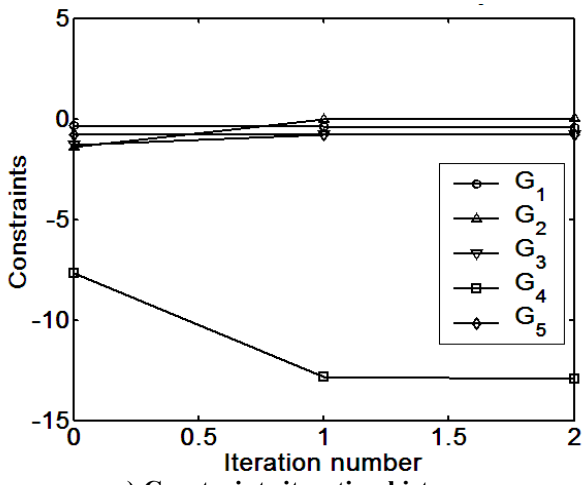

c) Constraints iteration history.

Figure A.0.3. Iteration history for maximum $\eta_V L_V/D$ spherically-blunted cone/parallelogram (m = 4) in Table 8.3.

A.2 Maximizing $(L_V/D)/q_{s,tot}$

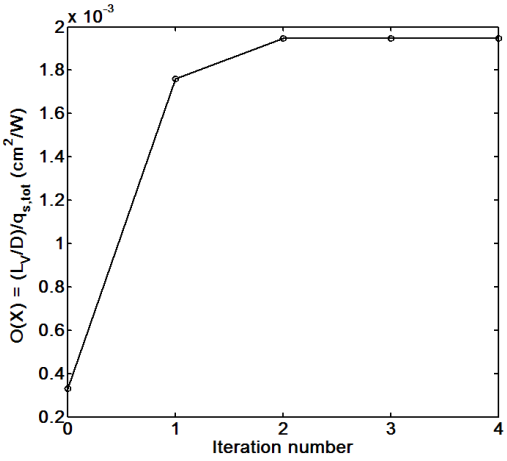

a) Objective function iteration history.

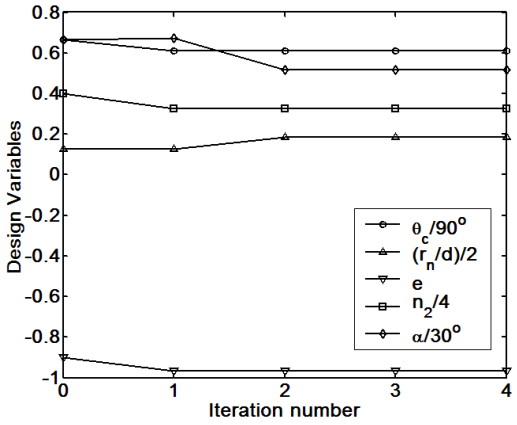

b) Design variable iteration history.

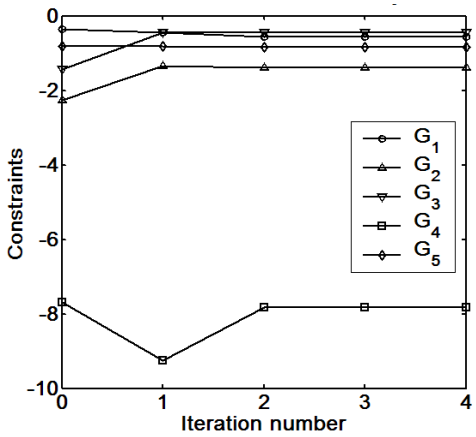

c) Constraints iteration history.

Figure A.0.4. Iteration history for maximum $(L_V/D)/q_{s,tot}$ spherically-blunted cone axial shape (m = 4) in Table 8.4.

Table A.0.1. Optimized $(L_V/D)/q_{s,tot}$ for M_∞ from 30 to 41, m = 4.

Spherically-blunted Cone Axial Shape Initial Design: $\theta_c = 60^o$, r_n/d=0.25, n_2 =1.6, e =-0.9, $\alpha = 20^o$					
Optimal Design (all cases have $\theta_c = 55^o$, e = -0.968, n_2 = 1.3)			Split Objective Function		Objective Function
M_∞	r_n/d	α	L_V/D	$q_{s,tot}$ (W/cm^2) ($q_{s,rad}$, $q_{s,conv}$)	$(L_V/D)/q_{s,tot}$ (cm^2/W)
30	0.379	20.5^o	0.872	280 (17.0, 263)	0.00311
31	0.327	14.8^o	0.986	359 (44.9, 314)	0.00275
32	0.292	15.2^o	1.02	452 (85.4, 367)	0.00226
33	0.316	16.8^o	0.984	543 (154, 389)	0.00181
34	0.184	16.1^o	1.10	738 (179, 559)	0.00149
35	0.150	13.6^o	1.14	911 (232, 679)	0.00125
36	0.206	20.2^o	0.998	1015 (381, 633)	0.000983
37	0.188	20.1^o	1.01	1200 (480, 720)	0.000842
38	0.169	13.5^o	1.13	1430 (600, 830)	0.000790
39	0.150	13.8^o	1.14	1670 (710, 960)	0.000683
40	0.150	13.6^o	1.14	1910 (880, 1030)	0.000597
41	0.150	13.5^o	1.14	2170 (1050, 1120)	0.000525

A.3 Minimizing $q_{s,tot}$

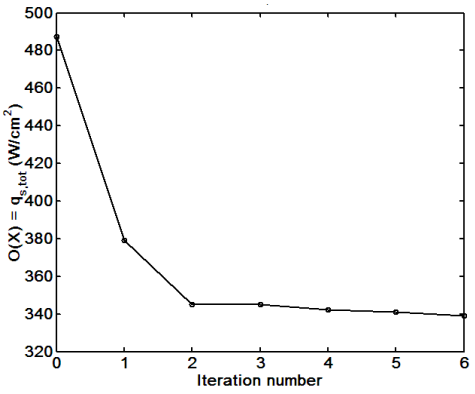

a) Objective function iteration history.

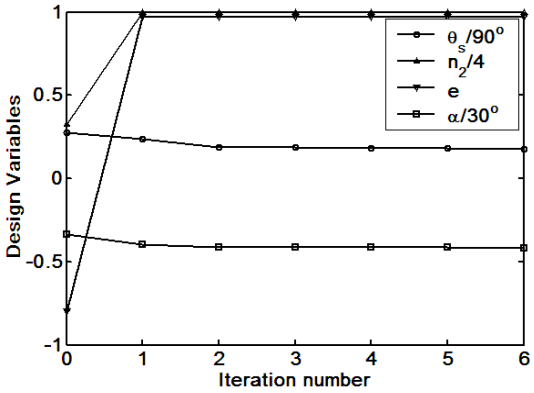

b) Design variable iteration history

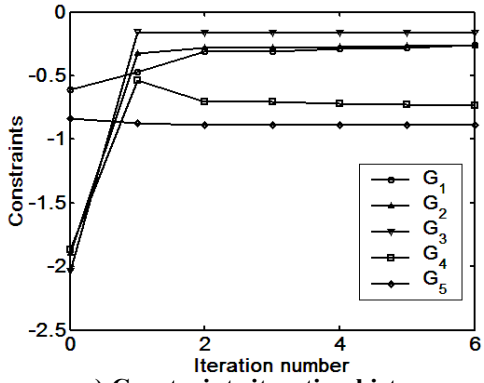

c) Constraints iteration history.

Figure A.0.5. Iteration history for minimum $q_{s,tot}$ spherical-segment axial shape (m = 4) in Table 8.5.

Table A.0.2. Optimized $q_{s,tot}$ for M_∞ from 30 to 41, m = 4.

Spherically-blunted Cone Axial Shape Initial Design: θ_c = 65°, r_n/d=1.1831, n_2 =1.8, e =-0.8, α = -10°							
Optimal Design							Objective Function
M_∞	θ_c	r_n/d	n_2	e	α	L_V/D	$q_{s,tot}$ (W/cm^2) ($q_{s,rad}$, $q_{s,conv}$)
30	55°	2.00	4.00	0.968	-11.7°	0.201	149 (35.1, 114)
31	55°	2.00	4.00	0.968	-12.4°	0.213	207 (80.2, 127)
32	55°	2.00	4.00	0.968	-12.4°	0.213	298 (158, 140)
33	75.6°	1.80	4.00	0.968	-11.9°	0.204	326 (163, 163)
34	55°	0.593	2.06	-0.171	-10.5°	0.122	596 (285, 312)
35	55°	0.615	2.81	0.356	-10.3°	0.129	735 (400, 335)
36	55°	0.384	1.98	-0.223	-10.2°	0.0992	896 (432, 464)
37	55°	0.368	1.83	-0.013	-10.3°	0.0978	1073 (556, 517)
38	55°	0.332	1.84	-0.009	-10.3°	0.0956	1279 (688, 592)
39	55°	0.313	2.65	0.041	-10.6°	0.115	1456 (795, 661)
40	55°	0.344	2.61	0.156	-10.3°	0.112	1680 (997, 683)
41	55°	0.292	2.74	0.073	-12.0°	0.130	1909 (1108, 801)

A.4 Minimizing $C_{m,cg,\alpha}$

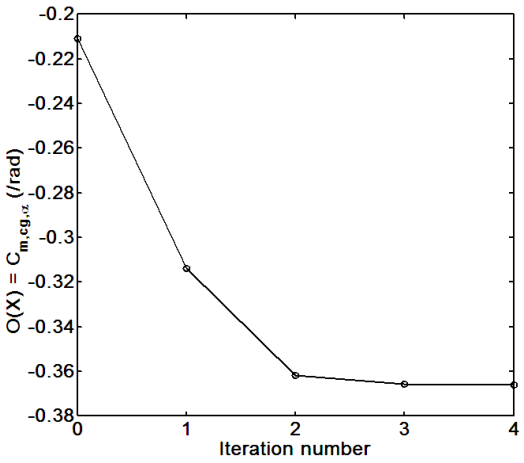

a) Objective function iteration history.

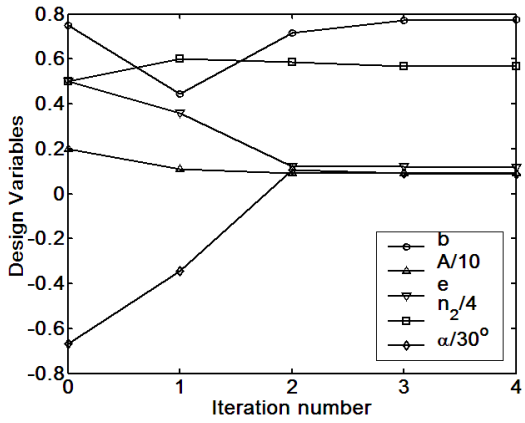

b) Design variable iteration history

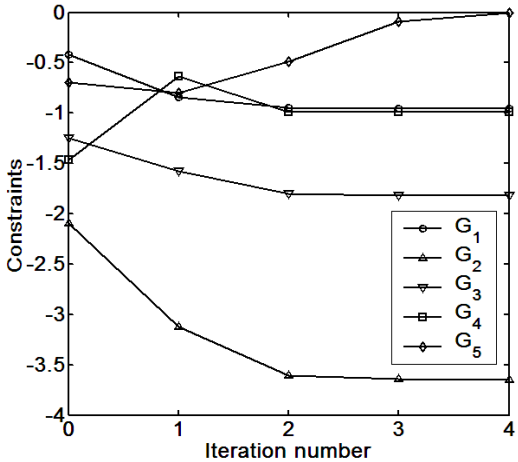

c) Constraints iteration history.

Figure A.0.6. Iteration history for minimum $C_{m,cg,\alpha}$ power law axial shape (m = 4) in Table 8.6.

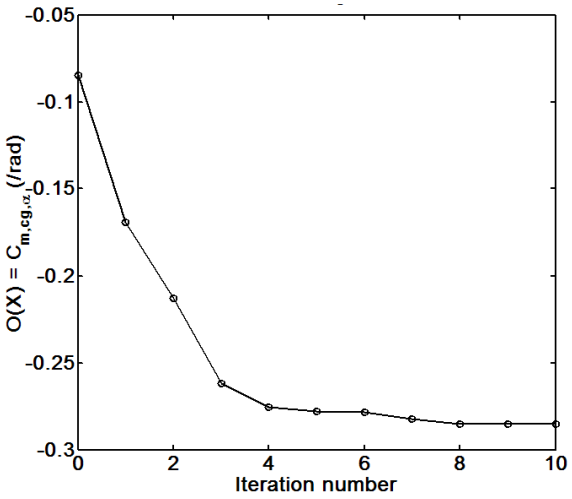

a) Objective function iteration history.

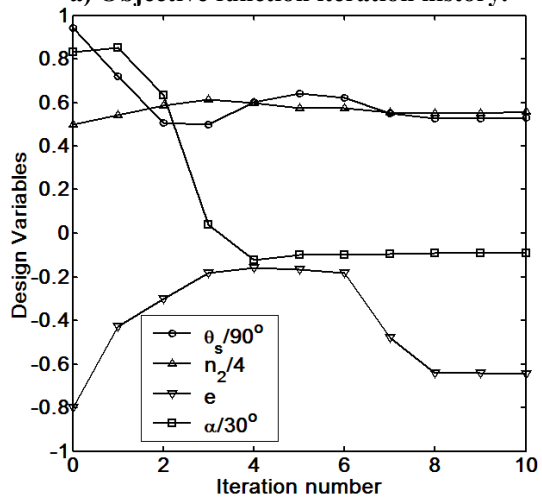

b) Design variable iteration history

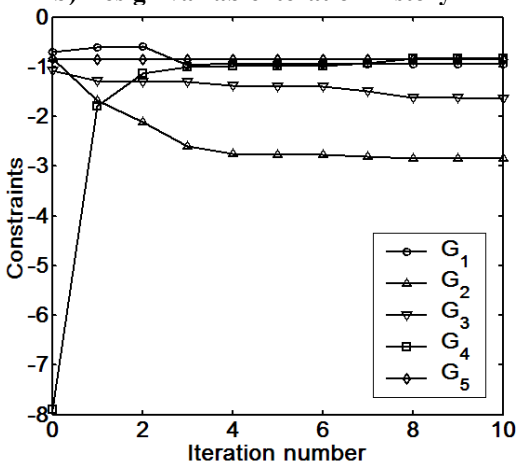

c) Constraints iteration history.

Figure A.0.7. Iteration history for minimum $C_{m,cg,\alpha}$ spherical-segment axial shape (m = 4) in Table 8.6.

Bibliography

[1] Crowder, R. S. and Moote, J. D., "Apollo Entry Aerodynamics," *Journal of Spacecraft and Rockets,* Vol. 6, No. 3, 1969, pp. 302-307.

[2] Kirk, D. B., Intrieri, P. F., and Seiff, A., "Aerodynamic Behavior of the Viking Entry Vehicle: Ground Test and Flight Results," Journal of Spacecraft and Rockets, Vol. 15, No. 4, 1978, pp. 208-212.

[3] Chrusciel, G. T. and Hull, L. D., "Theoretical Method for Calculating Aerodynamic Characteristics of Spherically Blunted Cones," AIAA Paper 1968-674, Jun. 1968.

[4] Faget, M. A., Garland, B. J., and Buglia, J. J., "Preliminary Studies of Manned Satellites, Wingless Configuration: Nonlifting," NACA RM L58E07a, 1958.

[5] Kruse, R. L., Malcolm, G. N., and Short, B. J., "Comparison of Free-Flight Measurement of Stability of the Gemini and Mercury Entry Capsules at Mach Numbers 3 and 9.5," NASA TM-X-957, 1964.

[6] Hillje, Ernest R., "Entry Flight Aerodynamics from Apollo Mission AS-202," NASA TN D-4185, 1967.

[7] Hillje, Ernest R., "Entry Aerodynamics at Lunar Return Conditions Obtained from the Flight of Apollo 4 (AS-501)," NASA TN D-5399, 1969.

[8] Moseley, W. C., Jr., Moore, R. H., Jr., and Hughes, J. E., "Stability Characteristics of the Apollo Command Module," NASA TN D-3890, 1967.

[9] Moseley, W. C., Jr., Graham, R. E., and Hughes, J. E., "Aerodynamic Stability Characteristics of the Apollo Command Module," NASA TN D-4688, 1968.

[10] DeRose, Charles E., "Trim Attitude, Lift and Drag of the Apollo Command Module with Offset Center-of-Gravity Positions at Mach Numbers to 29," NASA TN D-5276, 1969.

[11] Horstman, C. C., and Kussoy, M. I., "Free-flight Measurements of Aerodynamic Viscous Effects on Lifting Re-Entry Bodies," *Journal of Spacecraft and Rockets,* Vol. 4, No. 8, 1967, pp. 1064-1069.

[12] Jones, Robert A., Hunt, James L., "Measured Pressure Distributions on Large-Angle Cones in Hypersonic Flows of Tetrafluoromethane, Air and Helium," NASA TND-7429, Dec 1973.

[13] Tauber, M., Chargin, M., Henline, W., Chiu, A., Yang, L., Hamm, K. R., Jr., Miura, H., "Aerobrake Design Studies for Manned Mars Missions," *Journal of Spacecraft and Rockets,* Vol. 30, No. 6, 1993, pp. 656-664.

[14] Bernot, Peter T., Jordan, Bruce C., "Static Stability Charcteristis of Cone and Half-Cone Pyramid Configurations at Mach 6.83," NASA TND-3544, Aug 1966.

[15] Sammonds, R. I. and Kruse, R. L., "Viking Entry Vehicle Aerodynamic at M = 2 in Air and Some Preliminary Test Data for Flight in CO2 at M = 12," NASA TN D-7974, 1975.

[16] Willcockson, W. H., "Mars Pathfinder Heatshield Design and Flight Experience," *Journal of Spacecraft and Rockets,* Vol. 36, No. 3, 1999, pp. 374-379.

[17] Moss, J. N., Blanchard, R. C., Wilmoth, R. G., Braun, R. D., "Mars Pathfinder Rarefied Aerodynamics: Computations and Measurements," AIAA Paper 1998-298, Jan. 1998.

[18] Milos, F. S., Chen, Y. K., "Mars Pathfinder Entry Temperature Data, Aerothermal Heating, and Heatshield Material Response," AIAA Paper 1998-2681, Jun. 1998.

[19] Ezell, Edward Clinton, and Linda Neuman Ezell. *On Mars: Exploration of the Red Planet, 1958-1978.* NASA SP-4212, 1984.

[20] Shapland, D. J., Price, D. A., Hearne, L. F., "A Configuration for Re-Entry from Mars Missions Using Aerobraking," *Journal of Spacecraft and Rockets,* Vol. 2, No. 4, 1965, pp. 501-507.

[21] Micol, J. R. and Wells, W. L., "Hypersonic Lateral and Directional Stability Characteristics of Aeroassist Flight Experiment Configuration in Air and CF_4," NASA TM 4435, 1993.

[22] Wells, William L., "Measured and Predicted Aerodynamic Coefficients and Shock Shapes for Aeroassist Flight Experiment (AFE) Configuration," NASA TP-2956, 1990.

[23] Micol, John R., "Simulation of Real-Gas Effects on Pressure Distributions for Aeroassist Flight Experiment Vehicle and Comparison With Prediction," NASA TP-3157, Apr 1992.

[24] Davies, Carol B., Park, Chul, "Aerodynamic Characteristics of Generalized Bent Biconic Bodies for Aero-Assisted Orbital-Transfer Vehicles," NASA TM 84362, May 1983.

[25] Davies, Carol B., Park, Chul, "Optimum Configuration of High-Lift Aeromaneuvering Orbital Transfer Vehicles in Viscous Flow," *Journal of Spacecraft and Rockets,* Vol. 25, No. 3, Jun 1988.

[26] Magazu, Harry K., Lewis, Mark J., and Akin, David L., "Aerothermodynamics of a Parashield Re-Entry Vehicle," *Journal of Spacecraft and Rockets,* Vol. 35, No. 4, 1998, pp. 434-441.

[27] Murbach, Marcus S., "SCRAMP: The Development of an Advanced Planetary Probe from CFD to Re-entry Test Flight," 3rd International Planetary Probe Workshop, Athens, Greece, June 27-July 1, 2005.

[28] Whitmore, Stephen A., Banks, D., Andersen, B., and Jolley, P., "Direct-Entry, Aerobraking, and Lifting Aerocapture for hnuman-Rated Lunar Return Vehicles," AIAA Paper 2006-1033, AIAA Aerospace Sciences Meeting, Jan 2006.

[29] Bertin, J., *Hypersonic Aerothermodynamics*, AIAA Education Series, AIAA, New York, 1993.

[30] Rasmussen, M., *Hypersonic Flow*, John Wiley & Sons, Inc. New York, 1994.

[31] Park, C., Davies, C. B., "Aerothermodynamics of Manned Mars Missions," AIAA Paper 1989-0313, Jan. 1989.

[32] Rochelle, W. C., Bouslog, S. A., and Ting, P. C., "Aerothermodynamic Environments for Mars Entry, Mars Return, and Lunar Return Aerobraking Missions," AIAA Paper 1990-1791, Jun 1990.

[33] Rose, P. H., Stark, W. I., "Stagnation Point Heat-Transfer Measurements in Dissociated Air," *Journal of the Aeronautical Sciences,* Vol. 25, No. 1, Feb 1958.

[34] Kemp, Nelson H., Rose, P. H., Detra, R. W., "Laminar Heat Transfer Around Blunt Bodies in Dissociated Air," *Journal of the Aero/space Sciences,* Vol. 26, No. 7, Jul 1959, pp 421-430.

[35] Lee, D. B., Bertin, J. J., Ried, R. C., "Apollo Reentry Heating," NASA TM X-66780, Sept 1963.

[36] Lee, D. B., Goodrich, W. D., "The Aerothermodynamic Environment of the Apollo Command Module During Superorbital Entry," NASA TN D-6792, Apr 1972.

[37] Lee, D. B., "Apollo Experience Report – Aerothermodynamics Evaluation," NASA TN D-6843, Jun 1972.

[38] Pavlosky, J. E., Leger, L. G. St., "Apollo Experience Report – Thermal Protection Subsytem," NASA TN D-7564.

[39] Park, C., Tauber, M. E., "Heatshielding Problems of Planetary Entry, A Review," AIAA Paper 1999-3415, Jun 1999.

[40] Scotti, S. J., "Current Technology for Thermal Protection Systems," NASA CP-3157, Feb 1992.

[41] Lovelace, Uriel M., "Charts Depicting Kinematic and Heating Parameters for a Ballistic Reentry at Speeds of 26,000 to 45,000 Feet Per Second," NASA TN D-968, Oct 1961.

[42] Tauber, M. E., and G. P. Menees, "Aerothermodynamics of Transatmospheric Vehicles," *AIAA Journal of Aircraft,* Vol. 24, No. 9, 1987, pp. 594-602.

[43] Fay, J. A., Riddell, F. R., "Theory of Stagnation Point Heat Transfer in Dissociated Air," *Journal of Aeronautical Sciences,* Vol. 25, No. 2, Feb 1958.

[44] Zoby, E. V., Sullivan, E. M., "Effects of Corner Radiuus on Stagnation-Point Velocity Gradients on Blunt Axisymmetric Bodies," NASA TM X-1067, Mar 1965.

[45] Tauber, M. E., Sutton, K., "Stagnation-Point Radiative Heating Relations for Earth and Mars Entries," *AIAA Journal of Spacecraft & Rockets,* Vol. 28, No. 1, 1991, pp. 40-42.

[46] Park, C., "Stagnation-Point Radiation for Apollo 4 – A Review and Current Status," AIAA Paper 2001-3070, Jun 2001.

[47] Cauchon, D. L., "Radiative Heating Results form the FIRE II Flight Experiment at a Reentry Velocity of 11.4 Kilometers per Second," NASA TM X-1402, Jul 1967.

[48] Ried, Jr., R. C., Rochelle, W. C., Milhoan, J. D., "Radiative Heating to the Apollo Command Module: Engineering Prediction and Flight Measurement," NASA TM X-58091, Apr 1972.

[49] Suttles, J. T., Sullivan, E. M., Margolis, S. B., "Curve Fits of Predicted Inviscid Stagnation-Point Radiative Heating Rates, Cooling Factors, and Shock Standoff Distances for Hyperbolic Earth Entry," NASA TN D-7622, Jul 1974.

[50] Walters, Edward E., "Free-Flight Measurements of Radiative Heating to the Front Face of the Apollo Reentry Capsule as a Function of Angle of Attack," NASA TM X-851, Feb 1964.

[51] Kaattari, George E., "Shock Envelopes of Blunt Bodies at Large Angles of Attack," NASA TN D-1980, Dec 1963.

[52] Kaattari, George E., "A Method for Predicting Shock Shapes and Presssure Distributions for a Wide Variety of Blunt Bodies at Zero Angle of Attack," NASA TN D-4539, Apr 1968.

[53] Srinivasan, S., Tannehill, J. C., Weilmuenster, K. J., "Simplified Curve Fits for the Thermodynamic Properties of Equilibrium Air," NASA-CR-181245, Jun 1986.

[54] Tannehill, J. C., and P. H. Mugge, "Improved Curve Fits for the Thermodynamic Properties of Equilibrium Air Suitable for Numerical Computation Using Time-Dependent or Shock-Capturing Methods," NASA CR-2470, Oct 1974.

[55] Regan, F., *Re-Entry Vehicle Dynamics*, 1st ed., AIAA Education Series. AIAA, New York, 1994, Chap. 9.

[56] Levine, P., Ellis, T.R., Georgiev, S., "Factors Influencing the Design and Performance of Mars Entry Vehicles," *Journal of Spacecraft and Rockets,* Vol. 2, No. 2, 1965, pp. 130-146.

[57] Arora, R. K., Kumar, P., "Aerodynamic Shape Optimization of a Re-entry Capsule," AIAA Paper 2003-5394, AIAA Atmospheric Flight Mechanics Conference, Aug 2003.

[58] Papadopoulos, Periklis and Prabhakar Subrahmanyam, "Computational Investigation and Simulation of the Aerothermodynamics of Reentry Vehicles," AIAA 2005-3206, AIAA/CIRA 13th International Space Planes and Hypersonics Systems and Technologies, May 2005.

[59] Papadopoulos, Periklis and Prabhakar Subrahmanyam, "Trajectory Coupled Aerothermodynamics Modeling for Atmospheric Entry Probes at Hypersonic Velocities," AIAA 2006-1034, 44th AIAA Aerospace Sciences Meeting and Exhibit, Jan 2006.

[60] Barter, Neville J., *Space Data,* Northrop Grumman Space Technology, 5th ed, Mar 2003, Section 7.

[61] Gupta, R. N., Jones, J. J., Rochelle, W. C., "Stagnation-Point Heat-Transfer Rate Predictions at Aeroassist Flight Conditions," NASA TP-3208, Sept 1992.

[62] Sabean, John W., "Optimization of a Hypersonic Inlet with a Rectangular to Circular Transition Duct," Ph.D. Dissertation UM-AERO 99-09, Department of Aerospace Engineering, University of Maryland, College Park, MD, 1999.

[63] Gielis, J., "A Generic Geometric Transformation that Unifies a Wide Range of Natural and Abstract Shapes," *American Journal of Botany,* Vol. 90, No. 3, 2003, pp. 333-338.

[64] Eric W. Weisstein. "Simpson's Rule." From *MathWorld*--A Wolfram Web Resource. http://mathworld.wolfram.com/SimpsonsRule.html.

[65] Anderson, J. D., *Hypersonic and High Temperature Gas Dynamics,* AIAA, Virginia, 2000, Chap. 3.

[66] Anderson, J. D., *Fundamentals of Aerodynamics,* 3rd ed., McGraw-Hill Book Co., New York, 2001, Chap. 8.

[67] Nelson, Robert. C., *Flight Stability and Automatic Control,* 2nd Ed., McGraw-Hill Book Co., New York, 1997, Chap. 1, 2.

[68] Phillips, W. F., *Mechanics of Flight,* John Wiley & Sons, Inc., Hoboken, NJ, 2004.

[69] Anderson, J. D., *Introduction to Flight,* 4rd ed., McGraw-Hill Book Co., New York, 2000, Chap. 3.

[70] NOAA, NASA, USAF, "U.S. Standard Atmosphere, 1976," NASA-TM-X-74335, NOAA-S/T-76-1562, Oct 1976.

[71] DOT, Design Optimization Tools, Software Package, Ver. 4.20, Vanderplaats Research & Development, Inc., Colorado Springs, CO, 1995.

[72] Johnson, J. E., Starkey, R. P., and Lewis, M. J., "Aerodynamic Stability of Re-Entry Heat Shield Shapes for a Crew Exploration Vehicle," AIAA Paper 2005-4112, July 2005.

[73] Johnson, J. E., Starkey, R. P., and Lewis, M. J., "Aerothermodynamic Optimization of Re-Entry Heat Shield Shapes for a Crew Exploration Vehicle," AIAA Paper 2006-6273, Aug 2006.

[74] Loh, W. H. T., *Re-entry and Planetary Entry Physics and Technology,* Springer-Verlag New York Inc., New York, 1968, Chap. 2.

[75] Suttles, J. T., Sullivan, E. M., Margolis, S. B., "Curve Fits of Predicted Inviscid Stagnation-Point Radiative Heating Rates, Cooling Factors, and Shock Standoff Distances for Hyperbolic Earth Entry," NASA TN D-7622, Jul 1974.